12-2017

Energy Shaping Control for Stabilization of Interconnected Voltage Source Converters in Weakly-Connected AC Microgrid Systems

Nadia Lenora Carmita Smith
University of Arkansas, Fayetteville

Energy Shaping Control for Stabilization of Interconnected Voltage Source Converters in Weakly-Connected AC Microgrid Systems

A dissertation submitted in partial fulfillment
of the requirements for the degree of
Doctor of Philosophy in Engineering with a concentration in Electrical Engineering

by

Nadia Lenora Carmita Smith
University of Arkansas
Bachelor of Science in Electrical Engineering, 2010
University of Arkansas
Master of Science in Electrical Engineering, 2017

December 2017
University of Arkansas

This dissertation is approved for recommendation to the Graduate Council.

_____
Dr. Roy McCann, Ph.D.
Dissertation Director

_____
Dr. H. Alan Mantooth, Ph.D.
Committee Member

_____
Dr. Simon Ang, Ph.D.
Committee Member

_____
Dr. Uche Weijinya, Ph.D.
Committee Member

ABSTRACT

With the ubiquitous installations of renewable energy resources such as solar and wind, for decentralized power applications across the United States, microgrids are being viewed as an avenue for achieving this goal. Various independent system operators and regional transmission operators such as Southwest Power Pool (SPP), Midcontinent System Operator (MISO), PJM Interconnection and Electric Reliability Council of Texas (ERCOT) manage the transmission and generation systems that host the distributed energy resources (DERs). Voltage source converters typically interconnect the DERs to the utility system and used in High voltage dc (HVDC) systems for transmitting power throughout the United States.

A microgrid configuration is built at the 13.8kV 4.75MVA National Center for Reliable Energy Transmission (NCREPT) testing facility for performing grid-connected and islanded operation of interconnected voltage source converters. The interconnected voltage source converters consist of a variable voltage variable frequency (VVVF) drive, which powers a regenerative (REGEN) load bench acting as a distributed energy resource emulator. Due to the weak-grid interface in islanded mode testing, a voltage instability occurs on the VVVF dc link voltage causing the system to collapse.

This dissertation presents a new stability theorem for stabilizing interconnected voltage source converters in microgrid systems with weak-grid interfaces. The new stability theorem is derived using the concepts of Dirac composition in Port-Hamiltonian systems, passivity in physical systems, eigenvalue analysis and robust analysis based on the edge theorem for parametric uncertainty. The novel stability theorem aims to prove that all members of the classes of voltage source converter-based microgrid systems can be stabilized using an energy-shaping control methodology. The proposed theorems and stability analysis justifies the development of the

Modified Interconnection and Damping Assignment Passivity-Based Control (Modified IDA-PBC) method to be utilized in stabilizing the microgrid configuration at NCREPT for mitigating system instabilities. The system is simulated in MATLAB/Simulink™ using the Simpower toolbox to observe the system's performance of the designed controller in comparison to the decoupled proportional intergral controller. The simulation results verify that the Modified-IDA-PBC is a viable option for dc bus voltage control of interconnected voltage source converters in microgrid systems.

TABLE OF CONTENTS

LIST OF FIGURES

LIST OF TABLES

LIST OF SYMBOLS

e	error function
u	control input
x	state vector
x^*	equilibrium point
w	supply rate
y	system output
K	vector function
$g(x)$	Input matrix
$H(x)$	Hamiltonian energy function
$H_a(x)$	Added Hamiltonian energy function
$H_d(x)$	desired Hamiltonian energy function
$H_d(e)$	desired error Hamiltonian energy function
$J(x)$	Skew-Symmetric Interconnection matrix
$J_a(x)$	Added interconnection matrix
$J_d(x)$	Desired interconnection matrix
$J_d(e)$	Desired error interconnection matrix
$R(x)$	Semi-Positive Definite matrix
$R_a(x)$	added dissipation matrix
$R_d(x)$	desired dissipation matrix
$R_d(e)$	desired error dissipation matrix

MATHEMATICAL SYMBOLS

$g^{\perp}$ left-annihilator matrix

$\mathbb{R}$ set of real numbers

ω grid frequency

$\forall$ for any

$\subset$ subset

LIST OF ABBREVIATIONS

AFE	Active Front End Rectifier
B2B	Back to Back Converter
CBI	Control by Interconnection
EB	Energy Balancing
ES	Energy Shaping
ES-DI	Energy Shaping and Damping Injection
IDA	Interconnection and Damping Assignment
PBC	Passivity-Based Control
PCH	Port-Controlled Hamiltonian
PWM	Pulse Width Modulation
SPWM	Sinusoidal Pulse Width Modulation
SVM	Space Vector Modulation
VSC	Voltage Source Converter
VSI	Voltage Source Inverter

CHAPTER ONE

INTRODUCTION

1.1 Microgrid State of the Art

According to the IEEE 1547.4 Std. a microgrid commonly referred to as a distributed island system is an electric power system (EPS) that consists of distributed energy resources (DERs) and loads; it includes the local EPS and has the ability to disconnect from and parallel with the area EPS [1-3]. This suggests the microgrid being a small-scale power system can operate in grid-connected or islanded mode generating, distributing and regulating the flow of electricity to local customers. This provides for improved reliability, resiliency, and power quality [2-7]. The main components of a microgrid include distributed resources, protective devices, master controller, loads, smart switches, communication, control and automated systems [2-3]. There are many types of microgrid architectures such as industrial, isolated, military and developmental currently being researched in the area of smart energy [8-9].

1.1.1 Distributed Energy Resources and Power Converters in Microgrids

Microgrids incorporate many distributed resources, which include energy storage systems, photovoltaics (PV), fuel cells, batteries, wind power and combined heat and power (CHP) illustrated in Figure 1.1. Renewable energy sources such as solar and wind are usually classified as non-dispatchable distributed units due to their high volatility and intermittent characteristics. Consequently, they cannot be controlled with a microgrid master controller and must be paired with an energy storage unit to provide adequate power to the critical loads. However many DERs cannot be directly connected to the microgrid and must be integrated through power electronic

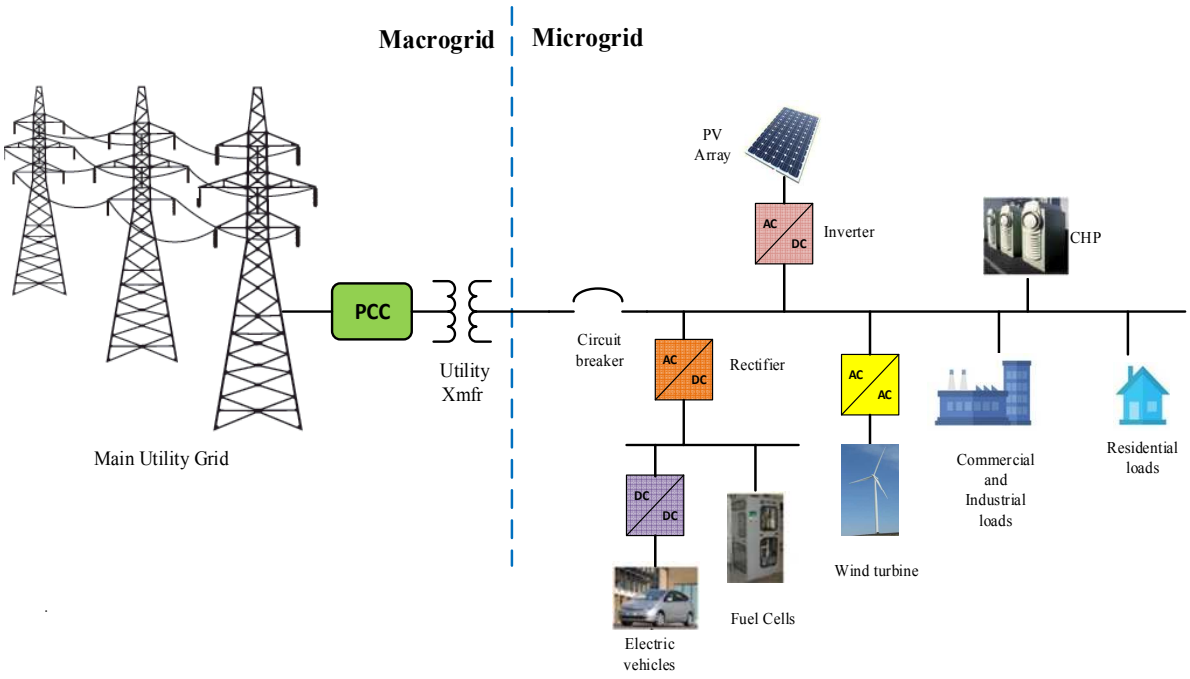

Figure 1.1 Microgrid System Configuration.

interfaces such as rectifier, inverters and two-level voltage source converters (VSC) [2],[10]. A two-level back-to-back (B2B) voltage source converter (VSC) is commonly used in providing bidirectional power flow in addition to frequency and voltage isolation between the utility and the grid [11]. In grid-connected mode, voltage source converters act as current sources feeding the utility grid, while in the islanded mode the VSCs act as a voltage source forming the output grid voltage to power the critical loads. The benefits of integrating power electronics in a microgrid range includes harmonic reduction leading to improved power quality to customers, reactive power control at the utility grid and voltage regulation at the point of common coupling. However, sometimes the utilization of power electronics brings about challenges in the controllability and stability of the microgrid [10],[12-13]. The types of stability that occur are transient, small signal, and voltage stability, which are usually associated with the control methods implemented in [10],[14-15].

Common stability control algorithms that have been proposed are linear active damping [13], direct voltage control and optimized power-sharing [13], and K factor control [16] which addresses the aforementioned challenges associated with microgrids.

1.1.2 Microgrid Operation and Control

As mentioned in the previous section, the microgrid operates in grid-connected and autonomous mode. To accomplish these tasks the microgrid utilizes a three-layer hierarchical control structure comprised of a primary, secondary, and tertiary control to minimize operational costs while ensuring reliability and maximum efficiency. The primary control or local control provides voltage and frequency stabilization using droop controllers and is also responsible for current injection. The main control techniques that exist in this layer are the master-slave and peer-to-peer control. The master-slave technique is associated with voltage-frequency control (V-f) and active and reactive power control (P-Q) while the peer-to-peer control is associated with the droop control techniques such as frequency-active power (f-P) control and voltage-reactive power (V-Q) control [2]. Droop control is important in the case of power-sharing among parallel inverters in the ac microgrids [17]. The secondary control provides compensation for any voltage and frequency steady-state errors associated with the primary control; the tertiary control determines the power flow between the microgrid and the utility-grid based on economic factors such as microgrid scheduling. This dissertation will focus on implementing robust control techniques for the primary control layer.

1.1.3 Microgrid Stability Issues

As mentioned in section 1.1.1 power electronics can sometimes contribute to instabilities in microgrid systems. With the integration of voltage source converter topologies to distributed energy resources, the challenge is to control these power converters while mitigating any

instabilities that would occur from the control implementation. Generally, the type of microgrid architecture greatly influences a specific stability issue. There are three types of stability concerns of research interest, which are the following:

- Small Signal Stability: This is usually associated with feedback control, changes in the load, system damping and power limits of the distributed generations. The mitigation of this instability can be contributed to the implementation of stabilizers for DGs, Energy Management systems, and supplementary control loops.
- Transient Stability: Transient stabilities are constituted by islanding, faults, and loss of DGs. Stability can be improved by implementing load-shedding methods, controlling power electronics, and energy storage.
- Voltage Stability: Voltage instabilities are due to load dynamics, under voltage load shedding, current limiters, and voltage regulation. Voltage stability can be improved by implementing load-shedding methods, controlling power electronics and energy storage.

1.1.4 Weak Microgrids

Due to the significant increase in the penetration of distributed energy resources, weak grids and microgrids have gained a lot of attention since the DERs are typically interconnected through power electronics interfaces which affect grid dynamics, control, and reliability. The grid strength is characterized as stiff or rigid if it is resilient to small perturbations such as load variations or switching of equipment [18]. On the contrary, the grid is characterized as weak if the system becomes unstable under perturbations. Some issues associated with weak grids include control instability, control interactions, and voltage instability. Typically, the analysis of weak grids is viewed from two perspectives. Firstly, analyzing power electronic converters, control algorithms,

and grid synchronization methods. Secondly, performing stability analysis on the network using the impedance-based stability analysis or the eigenvalue analysis to observe how the system performs to variations in the grid's impedance. The impedance-based analysis evaluates systems stability based on the ratio of the source output impedance to the load input impedance and applies the generalized Nyquist Criterion [19]. Using the eigenvalue analysis, a state-space model of the system is derived and the system's eigenvalues are determined and analyzed based on a zero/pole plane to view the stability of the system [19-20].

1.2 Motivation for Research

The primary motivation for this research stems from a 13.8kV 4.75 MVA research facility for a microgrid laboratory testbed that is built and tested at the National Center for Reliable Electric Power Transmission (NCREPT) at the University of Arkansas shown in Figure 1.2. This facility provides for prototyping and testing power interface applications such as solar inverters, grid reliability technologies such as fault current limiters and transportation applications such as automotive and traction systems.

The authors in [7] describes the microgrid test bed, which consists of one 750kVA variable voltage variable frequency (VVVF) drive being configured as a two-level back-to-back (B2B) voltage source converter; two B2B voltage source converters acting as regenerated drives rated at 2MVA; six 0.48Δ/4.16x13.8Y kV 2.5-MVA power transformers and several circuit breakers rated at low and medium voltages. A one-line diagram of the proposed microgrid is displayed in Figure 1.3 where a three phase 1.5 MVA utility transformer connects to the 12.47kV distribution line. The microgrid back-to-back voltage source converter (*MGVS*) acting as the VVVF drive is connected to the 480Vac bus *MSB1* through the circuit breaker *LVCB4*. The microgrid operates in

grid-connected mode when the low voltage circuit breaker *LVCB5* is closed and when it is opened the system operates in islanded mode. In the islanded mode, the *MGVS* provides power to the distributed resource emulators *DRE1* and *DRE2* through transformer $T6$ and the medium voltage bus *MVB2*. The *DREs* are also two-level back-to-back voltage source converters acting as regenerative load (REGEN) benches, which have the regenerative capability that can operate up to 2MVA and only consumes the losses from the utility grid.

Figure 1.2 NCREPT Test Facility [7].

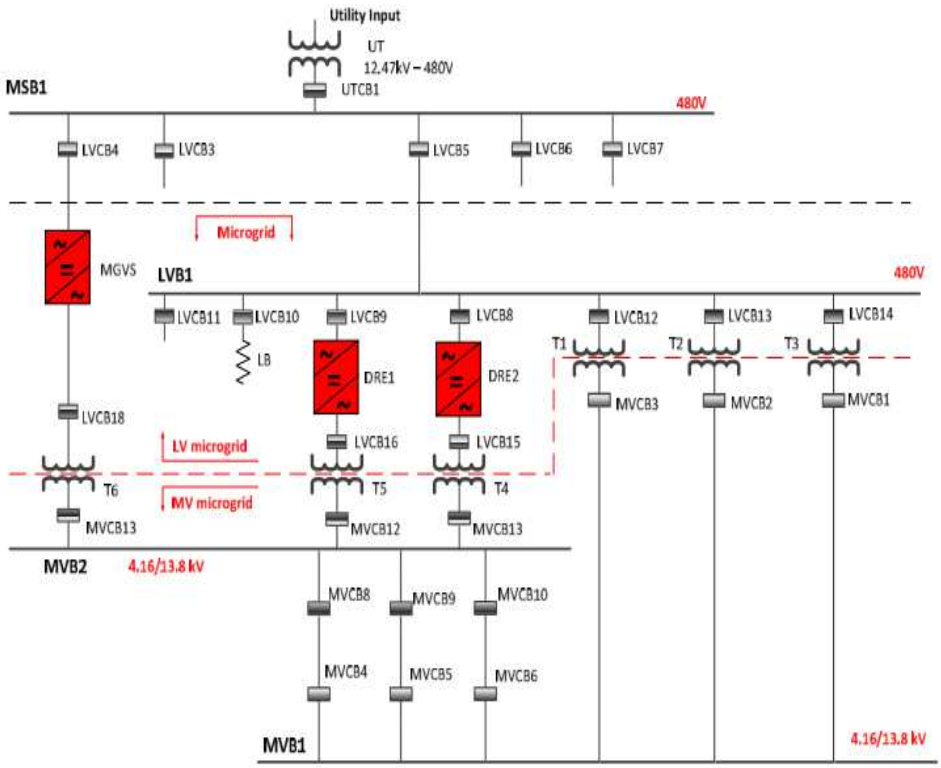

Figure 1.3 One-line diagram of proposed Microgrid Testbed [6-7].

1.2.1 Instability Issue of the Microgrid Testbed

The proposed microgrid testbed was tested to observe the performance of the VVVF drive and REGEN load bench. An experiment was conducted to operate the VVVF drive and REGEN bench in standalone mode and islanded mode to collect instability data from a CATS 2000 LabVIEW data acquisition unit. Figure 1.4 shows the experimental data obtained of the REGEN bench operating in standalone mode when the load is at 10% of the full load. In the islanded mode, the VVVF drive and REGEN bench are interconnected. The active front-end (AFE) rectifier of the VVVF drive stabilizes the dc link voltage to 750Vdc. Once commanded dc link voltage is obtained, the inverter of the VVVF drive turns on providing 480Vrms to the REGEN bench. The AFE of the REGEN bench charges its dc link capacitor voltage to 750Vdc. Afterwards, the REGEN's inverter acting as a load simulator injects current into the grid with a current value set by a user input. At

this instance, the VVVF drive capacitor dc link voltage experienced an overvoltage, increased above the maximum allowable limit, and collapsed. The VVVF drive providing the voltage to the microgrid was not able to handle the power consumed by the REGEN bench. Therefore this microgrid system is characterized as weak due to the high sensitivity of the VVVF drive. Figures 1.5 and 1.6 illustrates the dc link capacitor voltage performance when the VVVF drive and REGEN bench are connected. Figures 1.7-1.9 displays the VVVF output voltage for V_{ab}, V_{bc} and the VVVF output current I_a respectively. The results of this experiment prompted for the research and design of robust control methods, to improve the stability and the resiliency of the proposed microgrid configuration at NCREPT.

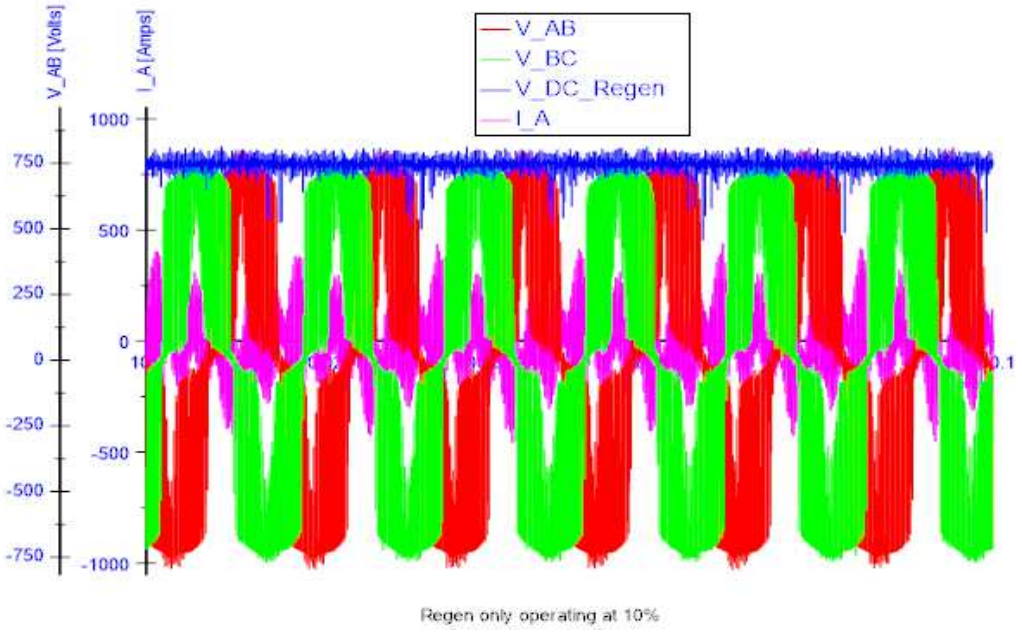

Figure 1.4 CATS 2000 Data Acquisition of REGEN Drive operation

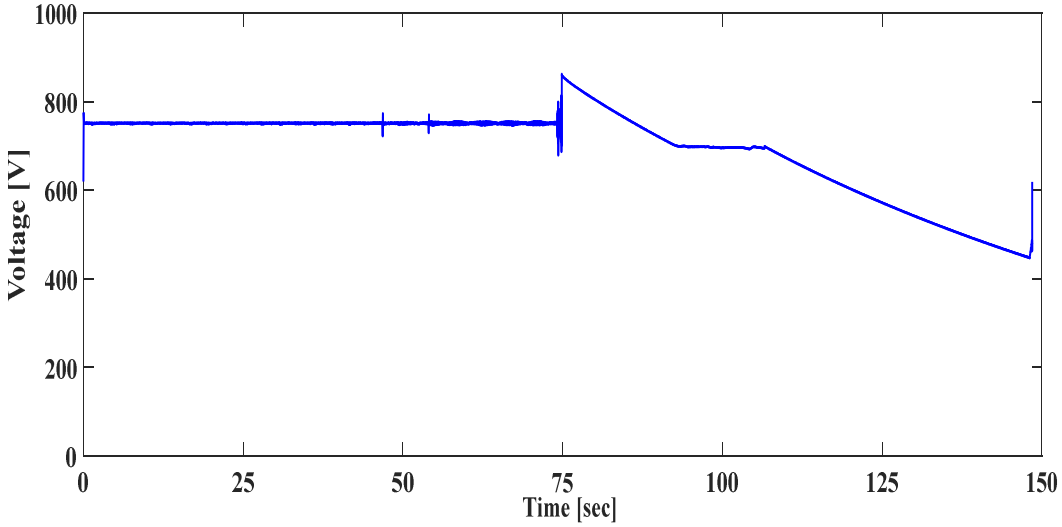

Figure 1.5 Variable Voltage Variable Frequency drive dc link capacitor voltage

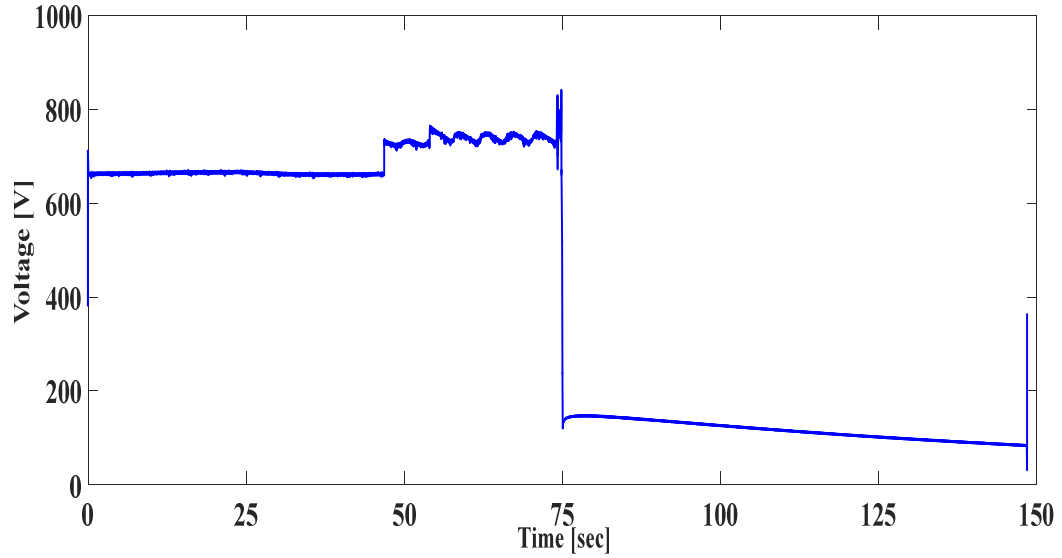

Figure 1.6 Regenerative bench dc link capacitor voltage

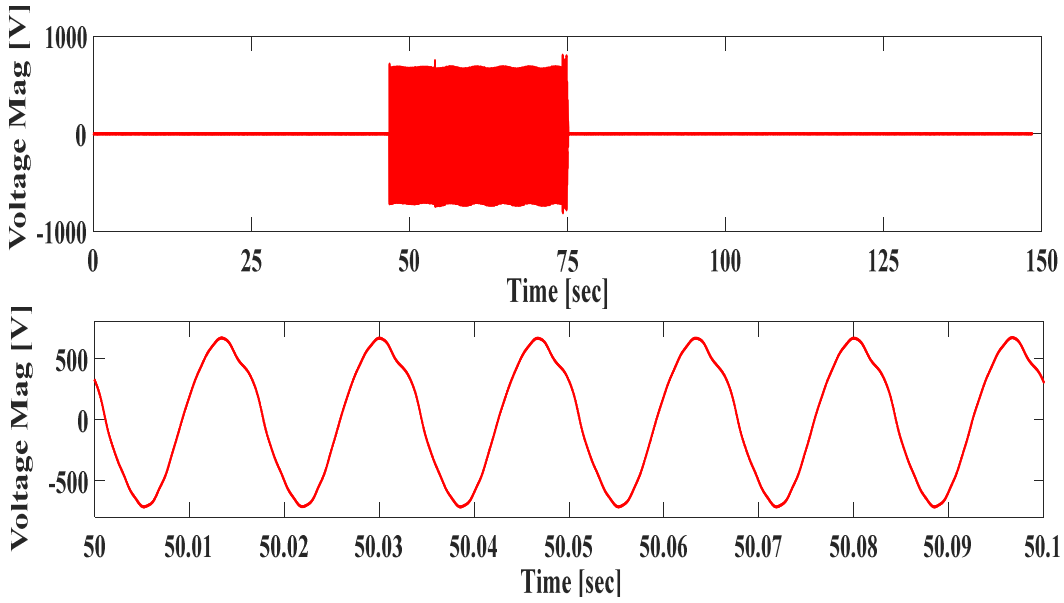

Figure 1.7 Variable Voltage Variable Frequency Drive Output Voltage for phase AB

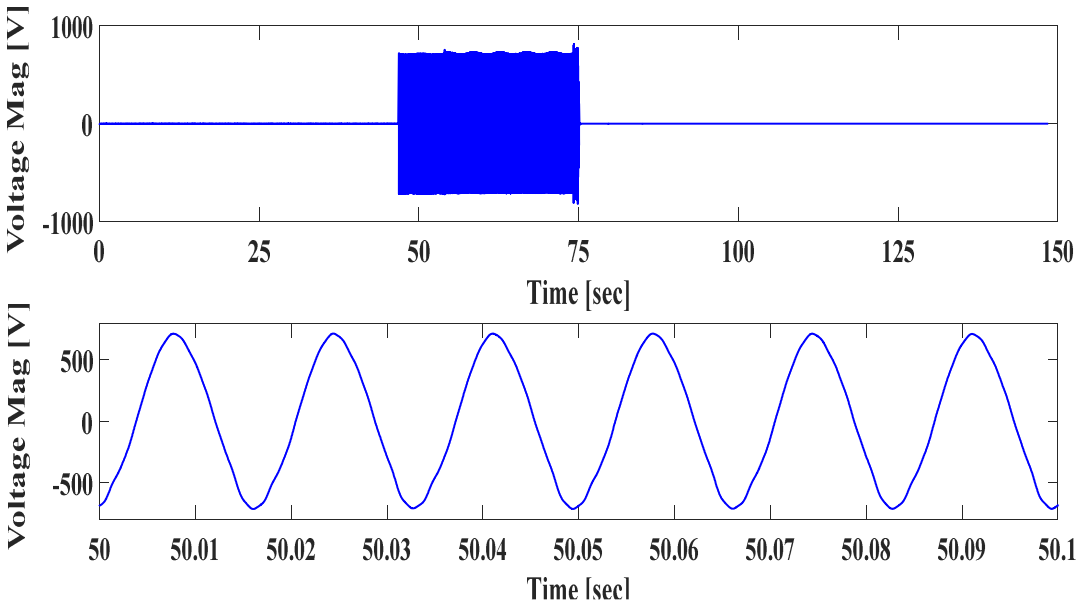

Figure 1.8 Variable Voltage Variable Frequency Drive Output Voltage for phase BC

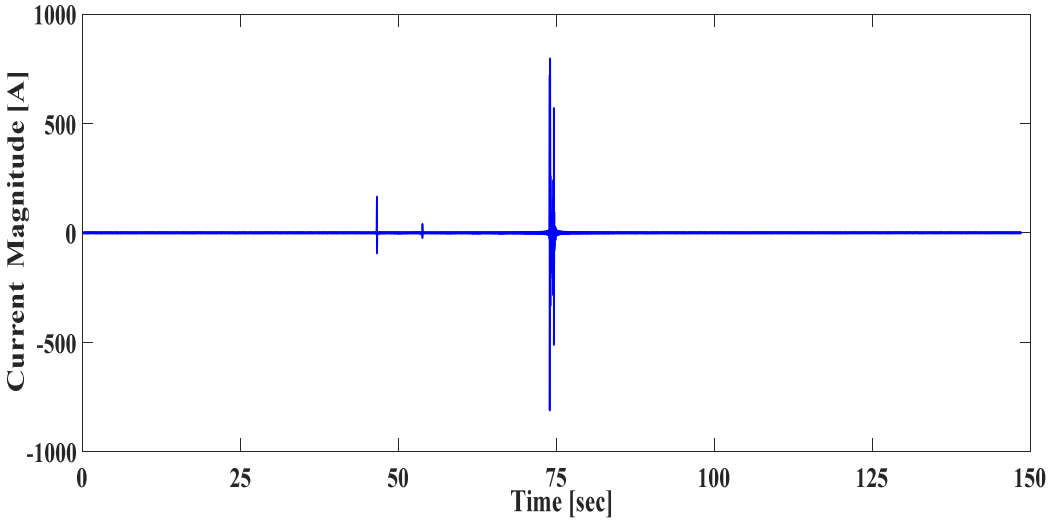

Figure 1.9 Variable Voltage Variable Frequency Drive phase 'a' Output Current

1.2.2 Load Frequency Control Applications for Transmission Systems

The secondary motivation for this research stems from the Midwest Interconnection Seams Study for the Grid Modernization Initiative which is a collaborative effort by Midcontinent Independent Service Operator (MISO), Southwest Power Pool, the National Renewable Energy Laboratory (NREL) and other university and industry partners. The aim of the interconnections seams study is to facilitate efficient transfer of electricity throughout the United States through a more integrated power system that will improve economic growth and the development and utilization of distributed energy resources such as solar and wind [21]. The interconnected areas in the power system either exports or imports a scheduled amount of power through transmission-line interconnection to its neighboring areas. Using load frequency control application each area absorbs its respective load changes during normal operation such that the steady-state frequency error is zero. A zero steady-state frequency error is maintained by ensuring that the total power flow out of each area through its tie-line is congruent with its pre-scheduled value.

The NCREPT system being a small-scale test-bed can be configured as a system of interconnected "SEAMS" with a weak grid interface in the islanded microgrid configuration as shown in Figure 1.10. The VVVF drive and REGEN bench can be viewed as interconnected seams with ac/dc ties resembling high-voltage, direct current HVDC two-level voltage source back-to-back converters, which are typically used for power transmission. The weak grid interface that exists in power systems is usually associated with wind energy conversion systems. In the southern region of the United States, Southwest Power Pool is responsible for wind generation providing power to loads on the south-eastern and south-western part of the United States. The passivity-based control stability method discussed in chapter three is advantageous for power systems because the voltage source converters in the seven back-to-back HVDC systems across the United States must be controlled to provide power over long distances [21]. In [22], an energy-based modeling and control method is used for electric power systems and HVDC transmission systems.

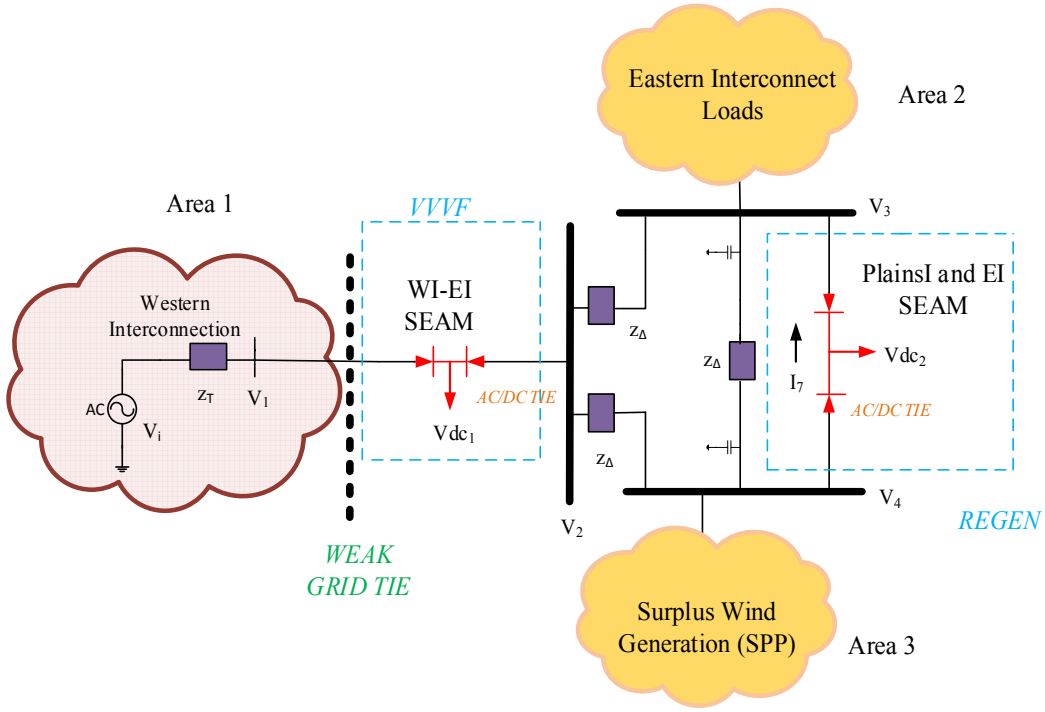

Figure 1.10 NCREPT system as SPP "SEAMS" Interconnection

1.3 Dissertation Objectives and Contributions

This new research contribution seeks to address the limitations associated with interconnecting multiple power electronic stages/converters that tend to become unstable under various loading conditions.

The new contributions this dissertation seeks to promote are as follows:

- Derive a stability theorem for all members of the class of interconnected VSCs-based microgrids utilizing the concepts of a Dirac Port-Hamiltonian system and the passivity property to prove that the NCREPT facility microgrid configuration is stabilizable using a passivity-based control method.
- Derive a Port-Controlled Hamiltonian Model and a Modified Interconnection and Damping Assignment Passivity-Based Controller (Modified IDA-PBC) for the microgrid

configuration at the NCREPT testing facility to address the voltage instability that currently exists.

The objectives of this dissertation are as follows:

- Model the active front-end rectifier of the VVVF drive and REGEN bench for the microgrid configuration using the Port-Controlled Hamiltonian modeling formulation.
- Design and simulate the Modified IDA-PBC method for the AFE rectifier of the VVVF driven and REGEN bench and compare with the traditional decoupled proportional integral current control method for dc voltage control in the two-level voltage source back-to-back converters.
- Model the Voltage Source Inverter of the VVVF drive using the Port-Controlled Hamiltonian modeling formulation.
- Design and simulate the Modified IDA-PBC method for the voltage source inverter of the VVVF compare with the traditional decoupled proportional integral current control for grid-forming mode operations.

1.4 Dissertation Organization

The dissertation is organized as follows:

- Chapter Two presents several preliminary nonlinear control theories that serve as a basis for understanding properties of nonlinear systems from a stability perspective. These concepts such as Lyapunov stability theory, passivity, dissipativity theory and equilibrium theory are used to determine robust control methods for controlling complex systems.
- Chapter Three examines the Lagrangian and Hamiltonian energy functions and the passivity properties that make them candidates for Lyapunov functions discussed in chapter two. This discussion leads to the modeling and control of Hamiltonian systems. The

passivity-based control theory presents the development of passivity-based controllers used to construct closed-loop stable controllers based on the energy shaping and damping assignment principle. The design method for the Interconnection and Damping Assignment Passivity-Based Control (IDA-PBC) and the Modified Interconnection and Damping Assignment Passivity-Based Control (Modified IDA-PBC) are discussed.

- Chapter Four discusses the two-level voltage source converter, which serves as the basis for understanding the two-level back-to-back (B2B) voltage source converter. The back-to-back VSC source converter is examined to illustrate how the rectifier and inverter are controlled in grid-feeding and grid-forming for microgrid applications. Additionally, reference frame transformations, pulse-width modulation, and grid synchronization techniques are presented.
- Chapter Five presents a novel stability theorem for a weak grid condition associated with microgrids using the principle of composition Dirac Port-Hamiltonian systems. A stability analysis of the NCREPT system is performed using an eigenvalue analysis and a robust analysis using parametric uncertainty via the edge theorem to illustrate that the stability of the microgrid is greatly influenced by varying the input impedance leading to the justification of utilizing the Modified IDA-PBC.
- Chapter Six presents the Port-Controlled Hamiltonian modeling method and the Modified IDA-PBC control method for the dc-ac inverter in the VVVF drive. The inverter control for the VVVF drive is designed to provide a reference output voltage of 480Vrms at a frequency of 60Hz.
- Chapter Seven presents the Port-Controlled Hamiltonian modeling method and the Modified IDA-PBC control method for the active front-end rectifier of the VVVF drive

and REGEN bench. The controller is designed to stabilize the dc link capacitor voltage of both back-to back converters.

- In Chapter Eight the microgrid configuration of the NCREPT system is simulated using the proposed controller. The system is simulated to view the performance of the VVVF drive in standalone mode and islanded mode in which the VVVF drive and REGEN bench are interconnected. The islanded mode simulation results with the proposed controller are compared to the decoupled proportional integral current controller.
- Chapter Nine provides concluding remarks about the Modified IDA-PBC for the NCREPT system and future work along the same line of research is presented.

1.5 Summary

This chapter provides an overview of the state of the art of microgrid systems. The motivation for this research is also discussed along with the dissertation outline and new research contribution.

CHAPTER TWO

PRELIMINARIES IN NONLINEAR CONTROL

2.1 Introduction

Physical systems such as mechanical, robotics, and electrical systems possess inherent nonlinearities that can produce undesirable effects when in operation. This has prompted the design of robust control methods and nonlinear analysis techniques to compensate for them. Unlike linear systems where the system can be analyzed in time or frequency domain, the complexities of a nonlinear system make it impossible to implement such analysis [23-24]. Hence, other analytical methods are embraced such as describing function analysis, phase plane analysis, and Lyapunov stability methods.

Firstly, the phase-plane analysis graphically analyzes and solves nonlinear systems. It is a two-dimensional plane used to observe the motion trajectories of a system and provides insight into the nonlinear effects. Secondly, describing function analysis approximates those nonlinear parts in the nonlinear system through linear approximations and analyzes the system utilizing frequency domain techniques. Lastly, Lyapunov stability methods are used in the design and analysis of a system by direct and indirect methods. The direct method consists of generalized energy concepts related to mechanical or electrical systems such that the motion of these systems are stable if the system's energy decreases all the time. The energy of the system is represented as a scalar-like function commonly referred to as a Lyapunov function, which is used in analyzing the stability of nonlinear systems. This energy function has inherent Lyapunov properties and is used in the direct method to observe whether it is decreasing or increasing. If the energy function is decreasing then the system is stable. The indirect or linearization method determines if a system's stability is close

to the linear approximation such that linear control techniques can be used to analyze the system [23].

In this chapter, the Lyapunov stability method will be the analytical and design tool of choice. In addition to understanding the analytical tools associated with the design methods for nonlinear systems it's essential to understand the properties and characteristics for stabilizing systems. This chapter presents the concepts of stability, Lyapunov stability theory, passivity and dissipativity which will form the basis of Port-Controlled Hamiltonian (PCH) modeling and Passivity-Based control (PBC) techniques discussed in Chapter three.

2.2 Stability Concepts

Stability theory plays a vital role in understanding nonlinear and robust control design of nonlinear systems. Stability of a system is examined in the sense of Lyapunov and addresses the behavior of a system around a desired equilibrium point. An equilibrium point refers to the value of the state vector that the system trajectory or curve in the state space corresponds to and can be defined by the standard definition 2.1.

Definition 2.1 [23][24] *A state $\boldsymbol{x}^*$ is an equilibrium state or equilibrium point of the system if once $\boldsymbol{x}(\boldsymbol{t})$ is equal to $\boldsymbol{x}^*$, it remains equal to $\boldsymbol{x}^*$ for all future time.*

Hence for a set of nonlinear dynamical equation in the form

$$\dot{x} = f(x, t) \,, \tag{2.1}$$

where x is a $nx1$ state vector and f is a vector function such that $f: D \to R^n$ is a locally Lipschitz map from a domain $D \subset R^n$ into R^n This means that the state vector x^* satisfies

$$f(x^*) = 0 \,, \tag{2.2}$$

of which the equilibrium points for the nonlinear equation in (2.2) can be solved.

The stability concept can also be referred to the system trajectory being kept arbitrarily close to the origin by starting sufficiently close to it [22],[24]. To study the stability of x^*, the definitions and theorems are stated for the case when the equilibrium point is at the origin where $x^* = 0$. Because nonlinear systems are more complex than linear systems addressing refined stability concepts are imperative as stated in the standard definition 2.2. The equilibrium point is stable if all solutions in the state space starting near the origin stays near the origin otherwise it is unstable. An equilibrium point is asymptotically stable if all solutions starting nearby the origin not only stay nearby, but tend to converge to the equilibrium point as time approaches infinity. It is globally asymptotically stable if the equilibrium point is asymptotically stable as the state approaches infinity.

Definition 2.2 [23][24] *The equilibrium point* $x = 0$ *of (2.1) is*

- ***stable*** *if, for each scalar* $\epsilon > 0$*, there is* $\delta = \delta(\epsilon) > 0$ *such that*

$$\|x(0)\| < \delta \;\Rightarrow \|x(t)\| < \epsilon, \quad \forall t \geq 0 \,. \tag{2.3}$$

- ***unstable*** *if it is not stable;*
- ***asymptotically stable*** *if it is stable and* δ *can be chosen such that*

$$x(t) \to 0 \text{ as } t \to \infty, \text{ for all } \|x(0)\| < \delta \,. \tag{2.4}$$

- ***globally asymptotically stable****, if it is stable and* $x(t_0) \to x^*$ *as* t *goes to infinity;*

2.3 Lyapunov Stability Theory

The Russian mathematician and engineer Aleksandr Lyapunov who sought to address the stability of equilibrium points in autonomous and non-autonomous systems first introduced the Lyapunov stability concept. The general concept of stability in terms of Lyapunov theory suggests how well a system behaves around a desired operating point and using the linearization of the direct method to verify the system stability properties in definition 2.2. The stability of nonlinear

systems is addressed using Lyapunov's linearization and direct method. The linearization method uses the principle of local stability i.e. how a system's state develops after starting near an equilibrium point and it encourages the use of linear control techniques such that a stable design using these techniques ensures the stability of the original physical systems [23][24]. The drawback of the linearization method is that the controller design must remain in a linear range, but sometimes it is difficult to predict how large that range is so the direct method is preferred.

The Lyapunov direct method hinges on the concept that if the energy function of a system is decreasing then the system converges to an equilibrium point. Hence a scalar "energy-like" function for the dynamical system can be generated and its time variation can be examined which allows the stability of the system to be determined [24]. The direct method has been used in the stable operation of multilevel converter-based distributed generation in power grids [25], reducing large-signal disturbances in three-phase PWM ac-dc voltage source converters [26], a neural network based controller design for ac-dc voltage source converters [27], large signal Lyapunov-based stability studies in microgrids [28], switched-mode power converters [29] and single-phase grid-connected PV central inverters [30]. Lyapunov's direct method classifies functions to determine the stability of an equilibrium point as shown in the standard theorem 2.1-2.3.

Theorem 2.1 [23][24][22] *Let* $x = 0$ *be an equilibrium point for (2.1) and* $D \subset R^n$ *to be the domain containing* $x = 0$. *Let* $V: D \to R$ *be a continuously differentiable function such that*

$V(x)$ *is a positive definite function when*

$$V(0) = 0 \quad \text{and} \quad V(x) > 0 \text{ in } D - \{0\}, \tag{2.5}$$

V(x) is *a positive semidefinite function* when

$$V(x) \geq 0, \tag{2.6}$$

V(x) is a *negative definite* or *negative semi-definite* function when $-\mathrm{V}(\mathrm{x})$ is positive definite or positive semidefinite.

V(x) is *indefinite* if it does not have a definite sign per the aforementioned cases.

Theorem 2.2 [22-24] *Let* $x = 0$ *be an equilibrium point for (2.1) and* $D \subset R^n$ *to be the domain containing* $x = 0$. *Let* $V: D \to R$ *be a positive definite scalar function. Then if its derivatives along the trajectories* $\dot{V}(x)$ *of the system in (2.1) is*

Negative semidefinite and the equilibrium point (x*) is stable i.e

$$\dot{V}(x) \leq 0 \quad . \tag{2.7}$$

Negative definite and the equilibrium point (x*) is asymptotically stable i.e

$$\dot{V}(x) < 0 \quad . \tag{2.8}$$

The positive definite scalar function V is called a *Lyapunov function*.

Theorem 2.3 [22-24] *Let* $x = 0$ *be an equilibrium point for (2.1) and* $D \subset R^n$ *to be the domain containing* $x = 0$. *Let* $V: D \to R$ *be a positive definite scalar function. Then if its derivatives along the trajectories* $\dot{V}(x)$ *of the system in (2.1) is negative definite and* $V(x)$ *goes to infinity then the equilibrium point is globally asymptotically stable.*

2.4 Passivity and Dissipativity

Passivity is a property of Lyapunov stability that takes into account energy conservation and transformation. As discussed in section 2.3, Lyapunov functions generalize the energy in a system so it can be assumed that the Lyapunov functions can be added or combined for subsystems in physical systems. The passivity theory utilizes the notion of Lyapunov functions by determining rules to describe the combination of subsystems expressed in a Lyapunov-like formulism such as the Port Controlled Hamiltonian and Euler Lagrange formalisms [31]. The passivity theory also represents an approach in constructing Lyapunov functions for feedback control [23].

Generally, passive systems cannot store more energy than is being supplied to it from the external environment with the difference being the dissipated energy [31]. Since passivity is related to the energy transformation of dynamical systems, feedback and parallel interconnection of passive systems can be viewed as a process of energy exchange, which follows that the feedback or sum of two passive systems yields a passive system[22],[31-32]. Figure 2.1- 2.2 illustrates the concept of the passivity of parallel and feedback connected subsystems, respectively where u represents the input supply from the external environment to independent systems where their energies are combined to form an output y that is passive in nature. This property can be generalized for an arbitrary number of cascaded subsystems by applying the passivity principle [33].

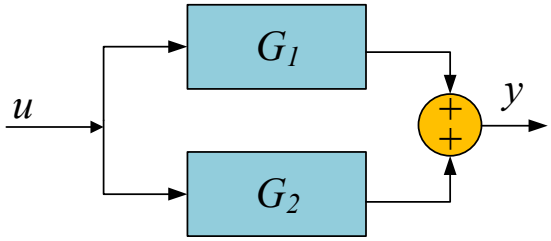

Figure 2.1 Passivity of Parallel connected systems.

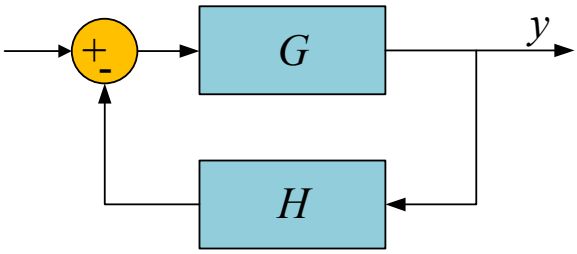

Figure 2.2 Passivity of Feedback connected systems.

Another concept associated with stability is dissipativity, which is a property of physical systems related to the dissipation of energy. Since passive systems take into account energy dissipation and transformation, it can be deduced that a passive system is inherently dissipative. The total Hamiltonian H energy of a passive system is defined in terms of the energy stored in the inductors and capacitors of the system. The conventional passivity and dissipativity definitions are given in the following equations [31].

Consider a general state space system $\sum$ which can be described as

$$\sum: \begin{cases} \dot{x} = f(x,u),\ x(0) - x_0 \in \mathbb{R}^n, \\ y = h(x,u), \end{cases} \tag{2.9}$$

where $x \in \mathbb{R}^n$ is the state vector, input $u \in \mathbb{R}^m$ and output $y \in \mathbb{R}^m$.

Definition 2.3 [22][31]*The system* $\sum$ *is passive if it is dissipative with supply rate* $w(u,y) = u^T y$. *It is input strictly passive (ISP) if it is dissipative with supply rate* $w(u,y) = u^T y - \delta_i \|u\|^2$ *where* $\delta_i > 0$. *And* $\sum$ *is output strictly passive it is dissipative with supply rate* $w(u,y) = u^T y - \delta_o \|y\|^2$ *where* $\delta_i > 0$.

Definition 2.4[22][31] *The* $\sum$ *is dissipative with respect to the supply* $w(u,y): \mathbb{R}^m x\, \mathbb{R}^m \rightarrow \mathbb{R}^n$ *if and only if there exists a storage function* $\mathcal{H}: \mathbb{R}^n \rightarrow \mathbb{R}_{\geq 0}$ *such that*

$$\mathcal{H}\big(x(T)\big) \leq \mathcal{H}\big(x(0)\big) + \int_0^T w(u(t), y(t))dt \tag{2.10}$$

for all , all $T \geq 0$ and all $x_0 \in \mathbb{R}^n$.

2.5 Zero Dynamics

Definition 2.5 [24]*The zero dynamics of systems are the internal dynamics of the system that are induced by zeroing the output.*

Remark 2.1 [24] If the zero dynamics has an asymptotically stable equilibrium point in the domain of interest the system is said to be *minimum phase*. If the zero dynamics of the system is stable it is *weakly minimum phase* and if its zero dynamics are unstable it is *non-minimum* phase.

2.6 Summary

This chapter discusses fundamental principles of nonlinear control as it relates to physical systems. Stability theories, concepts, and properties of nonlinear systems are presented. This chapter serves as a basis for understanding the Modified Interconnection and Damping Assignment Passivity control method and Port-Control Hamiltonian modeling methods discussed in chapter three.

CHAPTER THREE
ENERGY-SHAPING PASSIVITY-BASED CONTROL

3.1 Introduction

Switch-mode power converters possess nonlinear characteristics that contribute to its instabilities. These nonlinearities are constituted by switching elements, parasitics in the passive elements and electromagnetic couplings between components. Some approaches to controlling power converters are feedback linearization, sliding mode control, sinusoidal pulse-width modulation and current mode controllers. Although the control schemes are used often for stability they do not take into consideration the physical nature of the model and the energy relation of the system. In designing switched-mode power converters one must consider its dynamic behavior. Due to the increasing demands of energy management and conversion, reduced harmonic generation, and reliability the classical control design techniques have reached their limits leading to the development of controllers that takes into account the nonlinearities of the system. One such nonlinear stability controller is the passivity-based control method which has been investigated for the past decade [34].

Passivity-based control shapes the energy of the system by using principles of Lyapunov's theory to design stabilizing controllers for nonlinear closed-loop systems. This controller can be designed through energy-shaping using the Euler-Lagrange (EL) and Port-Controlled Hamiltonian (PCH) methods or a Power-Shaping method, which utilizes the Brayton-Moser framework. Euler-Lagrange and Port-Controlled Hamiltonian control methods are used in mechanical and electromechanical systems while Port-Controlled Hamiltonian are utilized in electrical systems.

3.2. Lagrangian and Hamiltonian Systems

Physical systems of multi-domains can be modeled using the Lagrangian and Hamiltonian frameworks. The main idea of these frameworks is the energy storage concept of passive systems. Knowing that physical systems can be viewed as smaller subsystems that exchange energy among themselves they are also referred to as energy-transformative devices and this concept provides a basis for modeling from an energy perspective [35]. There are two types of modeling frameworks that incorporates the passivity-based control method which are the Euler-Lagrange and Hamiltonian modeling systems.

Lagrangian modeling is used for deriving equations of motion for mechanical and electrical systems based on the EL functions resulting in EL equations. In electrical systems, for example, the Lagrangian energy function is represented as the difference between the total magnetic co-energy and the total electric energy[35][36]. Since EL systems are passive, a feedback controller can be designed by the averaging method with the assumption that EL systems are closely related to PWM models that operate at high switching frequencies [37].

Hamiltonian modeling is an extension of the Lagrangian modeling system. Hamiltonian equations are obtained for the Hamiltonian energy function, which is the total stored magnetic energy and electric energy of the system. A Hamiltonian system is a lossless system with an underlying LC structure that acts as ports. From a Lyapunov stability perspective, the Hamiltonian and EL energy functions serve as a basis for constructing candidate Lyapunov functions leading to the development of system properties such as stability and passivity.

3.3 Port-Hamiltonian Modeling Systems

In the electrical domain, a port is characterized as a set of terminals that obeys the port-Kirchhoff law. Typically, terminals are used for interconnection with the environment where the variables of these terminals are the currents and voltages. Ports are used for interchanging energy between the physical system and its environment and other interconnected sub-circuits [38]. From the electric circuit perspective, we can view a device as a black box with wires called terminals which the circuit uses to electrically interact with its environment. Hence, circuit modeling seeks to aim at describing this interaction. One such type of modeling is port-based modeling where the objective is to provide a framework for modeling complex systems of various domains. Since energy can be transformed from one form to another it is easily deduced that modeling physical systems of different domains can be achieved through three important characteristics that exist in physical systems which are energy storage, energy-dissipation, and energy routing [2],[39]. Since energy is a physics concept that is encompassed in different domains such as mechanical, electrical and hydraulics, it serves as a "vehicular language" for communicating among experts from different fields [35],[39].

Port-Hamiltonian modeling systems are comprised of three structures, which are energy-storage elements (S) (inductors and capacitors), energy-dissipating elements R (resistors) and the central interconnected energy-routing elements D shown in Figure 3.1. The structures are linked via variables called effort (e) and flow (f) which are paired to form ports. Hence the pair of vectors (f, e) is a set of port variables. In the electric domain the effort and flow port variables represent the current and voltage in a circuit respectively. Figure 3.1 displays three ports, which are (f_R, e_R) corresponding to energy-dissipation, (f_S, e_S) the energy-storage and (f_P, e_P) referring to the external port.

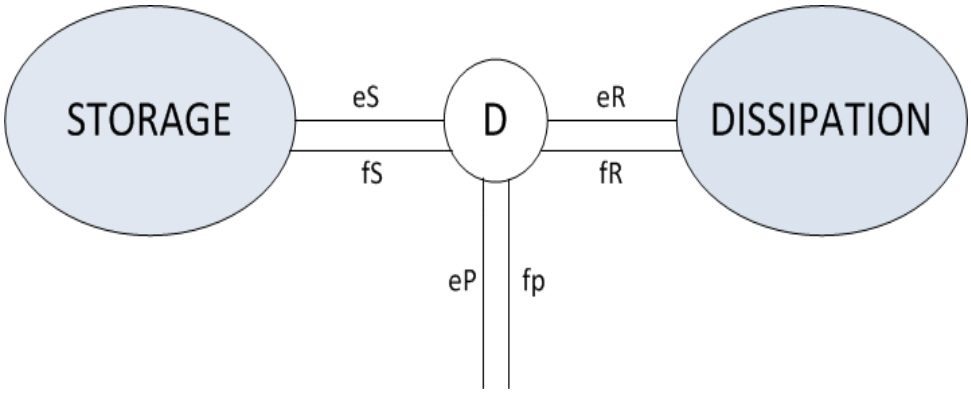

Figure 3.1 Port-Hamiltonian System.

Port-Hamiltonian systems are described by the following general nonlinear equations.

$$\begin{cases} \dot{x} = f(x) + g(x)u\,, \\ y = h(x)\,. \end{cases} \qquad (3.1)$$

The input state output port-Hamiltonian systems can be described by

$$\begin{cases} \dot{x} = [J(x) - R(x)]\,\dfrac{\partial H}{\partial x}(x) + g(x)u, \;\; x \in \mathbb{R}^n, \\ y = g^T(x)\dfrac{\partial H}{\partial x}(x) \end{cases} \qquad (3.2)$$

where $x \in \mathbb{R}^n$ is the state vector; and the port power variables $u \in \mathbb{R}^m$, $y \in \mathbb{R}^m$ are conjugated variables whose products has units of power. The symmetric dissipation matrix is represented by $R(x) = R^T(x) \in \mathbb{R}^{nxn}$.The interconnection structure is captured in the skew-symmetric matrix $J(x) = -J^T(x) \in \mathbb{R}^{nxn}$ and the input matrix $g(x) \in \mathbb{R}^m$.The Hamiltonian function $H(x) \in \mathbb{R}$ represents the system's total energy stored. The Hamiltonian of the system is given by

$$H(q, \phi) = \sum_{j=a,b,c} \left(\frac{1}{2}\frac{\phi_j^2}{L} + \frac{1}{2}\frac{q_j^2}{C} \right), \qquad (3.3)$$

where $\phi_j = (\phi_a\ \phi_b\ \phi_c)^T$ and $q_j = (q_a\ q_b\ q_c)^T$ represents the flux linkages and charges in the inductors and capacitors respectively.

The Hamiltonian relations for inductors and capacitors is defined as

$$\phi = L\frac{dq_L}{dt}\ . \tag{3.4}$$

$$q_C = C\frac{d\phi_C}{dt}\ . \tag{3.5}$$

3.4 Control of Port-Hamiltonian Systems

When a system has been modeled in its Port-Hamiltonian (PH) form (3.2), the next objective is to decide what type of control technique will be used to control the PH system. Energy-Based control techniques such as control by interconnection (CBI), stabilization by Casimir generation and energy transfer control are designed based on the perspective of interconnecting a plant's PH model with the controller PH system [39]. This chapter will focus on the design of a passivity-based control (PBC) method utilizing stability concepts from Lyapunov's theory in chapter two. In the case of stabilization, a controller design needs to generate a suitable candidate Lyapunov function to ensure the stability of the closed-loop system.

3.4.1 Passivity-Based Control

Passivity-Based Control (PBC) ensures the stability of a closed-loop system by making a system passive [31]. Essentially, the passivity-based control is a nonlinear model-based controller that successfully exploits the physical structure of a system and its passivity property since physical systems satisfy an energy-balancing equation such that a system's stored energy is equal to the difference between the supplied energy and the dissipated energy shown in equation 3.6

$$\underbrace{H[x(t)] - H[x(0)]}_{\text{Stored energy}} = \underbrace{\int_0^t u^T(s)y(s)ds}_{\text{Supplied energy}} - \underbrace{d(t)}_{\text{Dissipated energy}}, \tag{3.6}$$

where $d(t)$ is a nonnegative function that captures the dissipation effects. A new controller is then formed by modifying the energy balance equation such that the desired stored energy is equal to the difference between the new supplied energy and the desired dissipated energy shown in equation 3.7 as

$$\underbrace{H_d[x(t)] - H_d[x(0)]}_{\text{Desired Stored Energy}} = \underbrace{\int_0^t v^T(s)y'(s)ds}_{\text{New Supplied energy}} - \underbrace{d_d(t)}_{\text{Dissipated Energy}}, \tag{3.7}$$

where $H_d(x)$ is the desired total energy function; y' is the new passive output and d_d is the dissipation term to increase the rate of convergence [40]. Therefore, the passivity-based control utilizes the principle of energy shaping and damping injection to render a closed-loop system passive with respect to a Lyapunov-like desired storage function to determine a state feedback controller. The controller design to achieve passivity is a two-stage process. The first stage is energy-shaping where the potential energy of the system is modified such that the "new" potential energy has a global and unique minimum in the desired equilibrium. The second stage is damping injection where the system's dissipation function is modified to ensure asymptotic stability based on Lyapunov's theory as discussed in chapter two [1-2].

Many passivity-based control methods have been researched such as the Energy-Shaping and Damping Injection (ES-DI), Interconnection and Damping Assignment Passivity-Based control (IDA-PBC) and a Modified Interconnection and Damping Assignment [39], [41-42]. The Energy-Shaping and Damping Injection passivity-based control suffer from a dissipation obstacle, which does not allow the added energy to depend on the states of the system with natural damping. This

obstacle limits the controller's applicability to certain systems. The dissipation obstacle does not exist in the IDA-PBC method, which is a generalization of the energy shaping and damping injection method and focuses on set-point regulation. The Modified IDA-PBC is a variation of the IDA-PBC and is useful in reference tracking, which is not provided by the existing IDA-PBC. Passivity-based control with energy shaping has been used in stabilizing DC motor drives system, current source inverters, boost inverters, induction motors and the basic power electronic converter [43-44]. The following sections will provide the controller design methods for the IDA-PBC and the Modified IDA-PBC. The Modified IDA-PBC will be used in the control of the back-to-back converter, rectifier, and AC microgrid in chapters six and seven.

3.4.2 Interconnection and Damping Assignment Passivity-Based Control

Using the plant input-state-output port Hamiltonian equation in (3.2), the objective of the IDA-PBC is to obtain a static feedback control $\mu = \beta(x)$ to stabilize the given system (3.2) at a desired equilibrium point such that the closed-loop dynamical system is a Port-Controlled Hamiltonian with dissipation of the form denoted as [42]. Ortega et al. in [45] discusses the procedure for solving the closed-loop system in equation 3.8 discussed in the equations 3.9-3.20

$$\dot{x} = [J_d(x) - R_d(x)] \frac{\partial H_d}{\partial x}(x), \tag{3.8}$$

where the closed-loop desired internal interconnection matrix is given by

$$J_d(x) = J(x) + J_a(x), \tag{3.9}$$

And the closed-loop dissipation matrix is defined as

$$R_d(x) = R(x) + R_a(x) = R_d^T(x)\ , \tag{3.10}$$

with J_a and R_a being the additional internal interconnection and damping matrices. $J_d(x)$ satisfy skew-symmetry such that $J_d(x) = -J_d^T(x)$ and $R_d(x)$ satisfy the positive semi-definiteness such that $R_d(x) = R_d^T(x)$ with $R_d(x) \geq 0$.

The desired closed loop Hamiltonian function is defined by

$$H_d(x) = H(x) + H_a(x)\ , \tag{3.11}$$

where $H_a(x)$ represents the energy modification that is injected into the system and $H(x)$ is the open-loop Hamiltonian function. $H_d(x)$ has a minimum at the desired equilibrium point x^*. The controller $u(x)$ that achieves the closed objective in (3.8) is given by

$$u(x) = \left(g^T(x)g(x)\right)^{-1} g^T(x)([J_d(x) - R_d(x)]\frac{\partial H_d}{\partial x}(x) - [J(x) - R(x)]\ \frac{\partial H}{\partial x}). \tag{3.12}$$

The control objectives are satisfied when the desired closed-loop Hamiltonian function H_d, the desired interconnection matrix J_d , and the desired damping matrix are obtained by solving the matching condition given by

$$g^{\perp}(x)\ [J(x) - R(x)]\frac{\partial H}{\partial x}(x) = g^{\perp}(x)\ \ [J_d(x) - R_d(x)]\frac{\partial H_d}{\partial x}(x). \tag{3.13}$$

According to [39] solving the matching condition for the aforementioned matrices is usually a tedious process. Hence there are several observations that can be made in the process of selecting the desired interconnection and damping matrices which are the following:

- The selection of the desired interconnection and damping matrices $J_d(x),\ R_d(x)$ can be freely chosen only if the interconnection matrix satisfy skew symmetry and the damping matrix satisfy positive definiteness.
- Partially or completely fixing the desired Hamiltonian function $H_d(x)$ such that it satisfies the equilibrium condition.

- Using the left annihilator $g^{\perp}(x)$ in (3.13) as an additional degree of freedom which can be used to reduce the complexity of the matching condition.

The factors mentioned above leads to the development of three possible methods that would enable the selection of the desired matrices allowing for a solution to the partial differential matching equation. The three methods are discussed as follows [46]:

- Non-Parameterized IDA-PBC: The matrices $J_d(x)$ and $R_d(x)$ are fixed and the matching equation is solved for the desired energy Hamiltonian function $H_d(x)$ such that $H_d(x)$ has a minimum at the desired equilibrium point.
- Algebraic IDA-PBC: This approach allows the matching condition to be written as a set of algebraic equations in terms of the desired unknown interconnection and damping matrices $J_d(x)$ and $R_d(x)$ while fixing the desired energy Hamiltonian function $H_d(x)$.
- Parameterized IDA-PBC: This technique fixes the structure of $H_d(x)$ while imposing design constraints on the unknown matrices $J_d(x)$ and $R_d(x)$ for solving the matching equation.

Proposition 3.1 *Consider the system in (3.8) and the desired equilibrium x^* to be stabilized. Assume that we can find functions $\mu(x), R_a(x), J_a(x), H_a(x)$ and a vector function $K(x)$ which satisfies the partial differential equation such that the following conditions occur*

(i) (Integrability) $K(x)$ is the gradient of a scalar function that is,

$$\frac{\partial K}{\partial x}(x) = \left[\frac{\partial K}{\partial x}(x)\right]^T \tag{3.14}$$

(ii) (Equilibrium Assignment) $K(x)$ at x^* verifies

$$K(x^*) = -\frac{\partial H}{\partial x}(x^*) \quad \text{such that} \quad \frac{\partial H_d}{\partial x}(x^*) = 0$$

(3.15)

(iii) (Lyapunov Stability) The Jacobian of $K(x)$ satisfies the

$$\frac{\partial K}{\partial x}(x^*) > -\frac{\partial^2 H}{\partial x^2}(x^*) \quad \text{such that} \quad \frac{\partial^2 H_d}{\partial x^2}(x^*) > 0. \tag{3.16}$$

Under these conditions the closed loop system $\mu = \beta(x)$ will be a Port Controlled Hamiltonian system with dissipation given in (3.8) and

$$\frac{\partial H_a}{\partial x}(x) = K(x). \tag{3.17}$$

The equilibrium point x^* will be a locally stable equilibrium of the closed-loop given in (3.8) and will be under LaSalle's invariance principle asymptotically stable if the largest invariant set under the closed-loop dynamics contained in

$$\left\{x \in X \middle| \frac{\partial^T H_d}{\partial x}(x) R_d(x) \frac{\partial H_d}{\partial x}(x) = 0\right\}, \tag{3.18}$$

equals $\{x^*\}$ [31].

The stability of x^* is established by noting that along the trajectories of (3.8) a negative definite matrix is obtained as

$$\dot{H}_d = -[\nabla H_d]^T R_d(x) H_d \leq 0 \ . \tag{3.19}$$

From (3.19) it can be observed that $H_d(x)$ qualifies as a Lyapunov function since the derivative is negative and only equal to zero at the equilibrium point. To ensure bounded solutions an estimate of its domain of attraction is provided by the largest bounded level set

$$\{x \in R^n | H_d(x) \leq c\}. \tag{3.20}$$

From (3.20) when $\|x\| \to \infty$, $H_d \to \infty$ and a large range of asymptotic stability is achieved at the equilibrium point.

3.4.3 Modified Interconnection and Damping Assignment Passivity-Based Control

The Modified Interconnection and Damping Assignment Passivity-Based Control introduces a new matching equation, which extends the IDA-PBC control to reference tracking control and regulation control of port-controlled Hamiltonian systems and non-passive systems [46-47]. The Modified-IDA-PBC design method is similar to that of the IDA-PBC method; however, a new matching condition is designed in terms of error variables for reference trajectory tracking. Wang and Goldsmith [47] present the procedure for solving the closed-loop error equation in 3.21 using equations 3.22-3.31.

If we consider the general non-linear equation in (3.1), the closed-loop dynamic for the trajectory tracking error is a Port-Controlled Hamiltonian with dissipation of the form

$$\dot{x} = [J_d(e) - R_d(e)]\frac{\partial H_d}{\partial e}(x, x^*) + \dot{x^*}, \tag{3.21}$$

where $e = x - x^*$ the error is variable, x is the state vector, x^* is the desired reference trajectory, and $\dot{x^*}$ is the derivative of the reference trajectory.

$J_d(e)$ is the closed-loop internal error interconnection matrix given by

$$J_d(e) = J(e) + J_a(e), \tag{3.22}$$

$R_d(e)$ is the closed-loop error dissipation matrix is defined as

$$R_d(e) = R(e) + R_a(e) = R_d^T(e), \tag{3.23}$$

with $J_a(e)$ and $R_a(e)$ being the additional internal error interconnection and error damping matrices. $J_d(e)$ satisfy skew-symmetry such that $J_d(e) = -J_d^T(e)$ and $R_d(e)$ satisfy the positive semi-definiteness such that $R_d(e) = R_d^T(e)$ with $R_d(e) \geq 0$. The desired storage function $H_d(x, x^*)$: $R^n \Rightarrow$R such that it has minimum at $x = x^*$ is represented as

$$\min H_d(x, x^*) \text{ at } x = x^*, \tag{3.24}$$

The desired closed-loop error Hamiltonian function is defined by

$$H_d(e) = H(e) + H_a(e), \tag{3.25}$$

where $H(e)$ is the open-loop Hamiltonian function and $H_a(e)$ is the added energy function of the errors. The controller $u(x) = \beta(x, x^*)$ that achieve the closed objective in (3.20) is given by

$$\beta(x, x^*) = \left(g^T(x)g(x)\right)^{-1} g^T(x)\left\{[J(e) - R_d(e)]\frac{\partial H_d}{\partial x}(x, x^*) + \dot{x^*} - f(x)\right\}, \tag{3.26}$$

The control objectives are satisfied when the desired closed-loop error Hamiltonian function $H_d(e)$, the desired error interconnection matrix $J_d(e)$, and the desired error damping matrix $R_d(e)$ are obtained by solving the matching condition given by

$$g^{\perp}(x)f(x) = g^{\perp}(x)([J_d(e) - R_d(e)]\frac{\partial H}{\partial e}(x, x^*) + \dot{x^*}, \tag{3.27}$$

where $g^{\perp}(x)$ is a full-rank left annihilator of $g(x)$ such that $g^{\perp}(x)g(x) = 0$. Then (3.26) takes the following closed-loop port-controlled Hamiltonian form.

$$\dot{e} = [J_d(e) - R_d(e)]\ \frac{\partial H_d}{\partial e}(x, x^*), \tag{3.28}$$

with a locally stable equilibrium at $e = 0$. Then according to La Salle's principle, the closed-loop system in (3.26) will be asymptotically stable if the origin is an isolated minimum of $H_d(x, x_d)$ and the largest invariant set under the closed-loop dynamics (3.26) contained in

$$\left\{e \in R^n \middle| \frac{\partial^T H_d}{\partial x}(x, x_d)R_d(e)\frac{\partial H_d}{\partial x}(x, x^*) = 0\right\}, \tag{3.29}$$

equals $\{0\}$.

The stability of (x, x_d) is established by noting that along the trajectories of (3.27) a negative definite matrix is obtained as

$$\dot{H}_d(x, x^*) = -\frac{\partial^T H_d}{\partial x}(x, x_d)R_d(e)\frac{\partial H_d}{\partial x}(x, x^*) \leq 0\ , \tag{3.30}$$

From (3.29) it can be observed that $H_d(x, x^*)$ qualifies as a Lyapunov function since the derivative is negative and only equal to zero at the equilibrium point. To ensure bounded solutions an estimate of its domain of attraction is provided by the largest bounded level set

$$\{e \in R^n | H_d(x, x^*) \leq c\}. \tag{3.31}$$

From (3.31) when $\|e\| \to \infty$, $H_d \to \infty$ and a large range of asymptotic stability is achieved at the equilibrium point.

3.5 Extension to passivity property of Port-Controlled Hamiltonian Systems

In energy shaping control steady-state errors can arise due to modeling errors and noise. As mentioned in [42] and[48], an integrator can be added around the passive output preserving stability. The integral actions is combined to solve the steady state problem and increase the robustness of the system. Proposition 3.2 further explains the conventional integral action as it relates to the passivity property of port-controlled hamiltonian systems.

Proposition 3.2 [48] *(Integral action) Consider the system in (3.1) with the closed-loop* $u = \beta(x) + v$*, where* $\dot{v} = K_I g^T(x) \nabla H_d$*, such that* $K_I = K_I^T > 0$*. Then the stability properties in Proposition 3.1 are preserved.*

Proof. The closed-loop the closed loop takes the PCH form

$$\begin{bmatrix} \dot{x} \\ \dot{v} \end{bmatrix} = \begin{bmatrix} J_d(x) - R_d(x) & g(x)K_I \\ -K_I g^T(x) & 0 \end{bmatrix} \begin{bmatrix} \nabla_x W \\ \nabla_v W \end{bmatrix}, \tag{3.32}$$

where

$$W(x, v) \cong H_d + \frac{1}{2} v^T K_I^{-1} v, \begin{bmatrix} \nabla_x W \\ \nabla_v W \end{bmatrix}, \tag{3.33}$$

qualifies now as a Lyapunov function.

3.6 Summary

This chapter presented a general overview of two energy-based storage functions systems which are the Lagrange and Hamiltonian storage functions. These functions provide a basis for modeling Euler Lagrange and Hamiltonian systems. The Port-Control Hamiltonian modeling system is described and is used as a framework for designing a passivity-based control method. The passivity-based control method is a model-based nonlinear control method that takes into consideration the physical structure of a system. An overview of the design methodology for the Interconnection and Damping Assignment Passivity-Based Controller and the Modified Interconnection and Damping Assignment Passivity-Based Control are discussed.

CHAPTER FOUR

VOLTAGE SOURCE CONVERTERS IN AC MICROGRIDS

4.1 Two-level Voltage Source Converters

A voltage source converter (VSC) as its name states converts an ac voltage to dc voltage and vice versa. Voltage source converters can be two-level, three-level or multilevel. Some examples of these topologies include ac-dc rectifiers, three-level neutral point clamped inverters and modular multilevel converters. This chapter focuses on two-level voltage source converter topologies such as the ac-dc rectifier and the dc-ac inverter to be used in a back-to-back (B2B) converter configuration. A two-level voltage source converter generates two voltage levels at the output of the converter. Typically, voltage source converters are comprised of self-commutating switches which can be line-commutated i.e. gate turn-off thyristors or forced-commutated such those utilizing insulated gate bipolar transistors (IGBTs) and mosfets with antiparallel diodes for each leg which are turned on and off in a controlled manner. The commutating switches ensure bidirectional current flow thereby allowing the voltage source converter to operate as a rectifier or inverter[49-50].

Rectifier and inverter voltage source converters consists of phase reactors which are commonly located on the input and output of these converters are used for controlling the active and reactive power by regulating the current through them. The input and output phase reactors are also used in ac filtering to reduce high-frequency harmonics that occur in the input or output ac currents [49]. The dc link capacitor in VSCs is chosen to accommodate voltage stress across the commutated devices during operation. It also provides a low inductive path for the turned-off current and acts as an energy storage for controlling power flow in addition to reducing the voltage ripple on the dc side [49]. The two-level voltage source converters discussed in this chapter will

be the back-back two-level voltage source converter comprising of an active front-end rectifier and an inverter.

4.2 Two-Level Back-to-Back Voltage Source Converter

The two-level back-to-back (B2B) voltage source converter (VSC) is commonly used for bidirectional power flow in addition to frequency and voltage isolation between the utility and the grid. Other advantages include high power factor and high-efficiency capability[7],[51], which makes it favorable in motor drives and microgrid applications. Back-to-Back converters consist of an inverter and rectifier and in some applications an active front end (AFE) rectifier.

Figure 4.1 displays the two-level back-to-back voltage source converter topology that will be used in simulating and implementing the port-controlled Hamiltonian controller design in chapter 5. It can be observed from Figure 4.1 that the energy delivered from the AFE rectifier is stored in the dc link capacitor and that energy is sent to the inverter to be delivered to the load [52]. For bidirectional power flow capability, the output current must be 180 degrees out of phase with the output voltage. The rectifier and inverter operation in the two-level back-to-back converter for ac microgrid applications are discussed in the following sections.

4.2.1 Active Front End rectifier (AFE)

The objective of the active front end rectifier in Figure 4.1 serves to regulate the dc link capacitor voltage and to ensure unity power factor at the grid. The active front-end rectifier consists of an LC filter which is used to reduce current harmonics around the switching frequency of the converter [53]. If an isolation transformer is used then an LCL filter is assumed at the input of the rectifier. According to Liserre et al.[53], when designing a controller for the active rectifier, the system should be modeled in the rotating frame of an L-based active rectifier. This allows the LCL

filter to be reduced to an L-filter. Additionally, the filter capacitor can be neglected if its value is low.

The AFE rectifier is controlled using the traditional dual loop control comprising of a fast inner current control loop which regulates the current flow into the converter and a slow outer voltage loop for regulating the dc bus voltage. The controller is designed by sensing the three-phase grid voltages and currents and converting them to their dc equivalents on the dq reference frame through Parks transformation. To ensure proper operation, zero steady state error of the dc currents and voltages are enabled by utilizing proportional integral (PI) controllers. Figure 4.2 displays the control structure of the active front end rectifier.

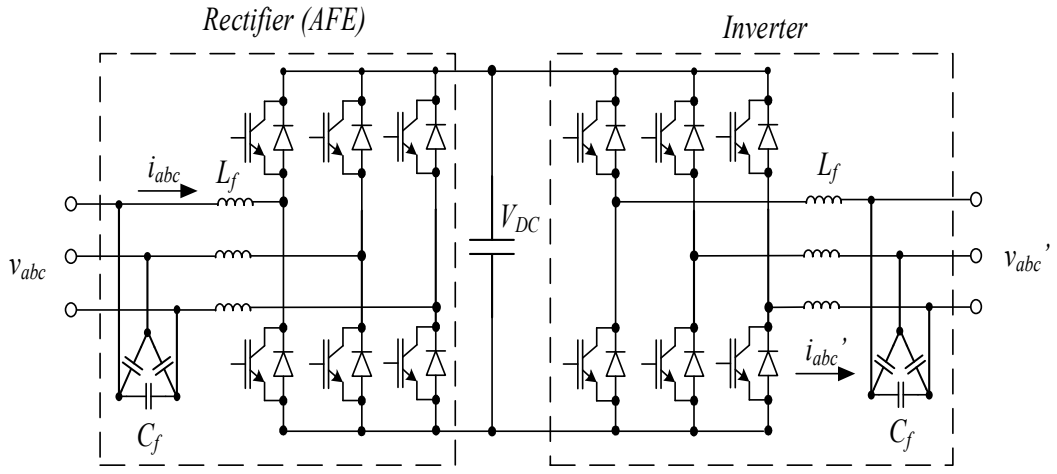

Figure 4.1 Two-level Back-to-Back Voltage Source Converter Topology.

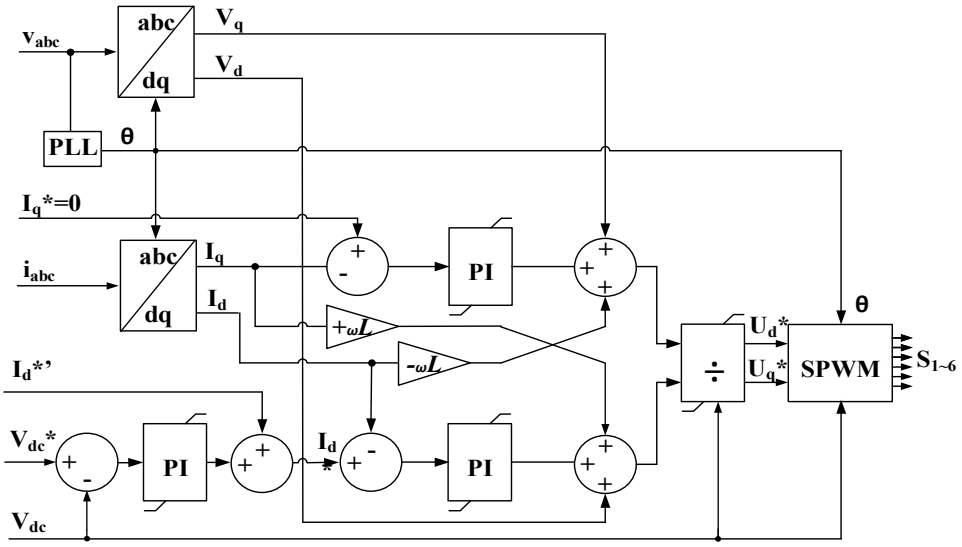

Figure 4.2 Control structure for Active Front-End Rectifier [6].

4.2.2 DC-AC Voltage Source Inverter

The dc-ac voltage source inverter in the back-to-back converter regulates the amplitude and frequency of the output voltages. For ac microgrid applications the inverter operates in three modes of operation shown in Figures 4.3-4.4 which are the following: grid-forming mode, grid-feeding mode and grid-supporting mode [54]. In grid-forming mode, the inverter is typically represented as an ideal ac voltage with a low-output impedance whereby the microgrid voltage and frequency at the point of coupling (PCC) are set by a reference voltage E_{ref} and reference frequency ω_{ref}. On the contrary, in grid-feeding mode, the inverter is viewed as an ideal current connected to the ac microgrid in parallel with a high impedance. The current injected flows to the utility grid and is determined by the reference active power P_{ref} and reactive power Q_{ref}.

In grid-supporting mode, the inverter can be represented as an ideal ac controlled current with a parallel impedance or controlled voltage source in series with an impedance.

This mode of operation combines the functionality of the grid-forming and grid feeding converter as it relates to voltage and frequency regulation in addition to current injection.

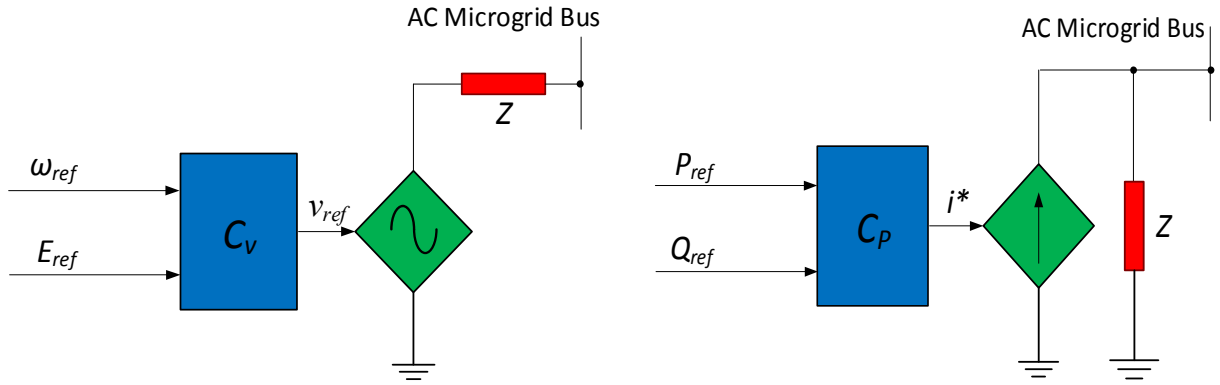

(a) Grid-Forming Converter (b) Grid-Feeding converter

Figure 4.3 Grid-Forming and Grid-Feeding Power Converter Representation.

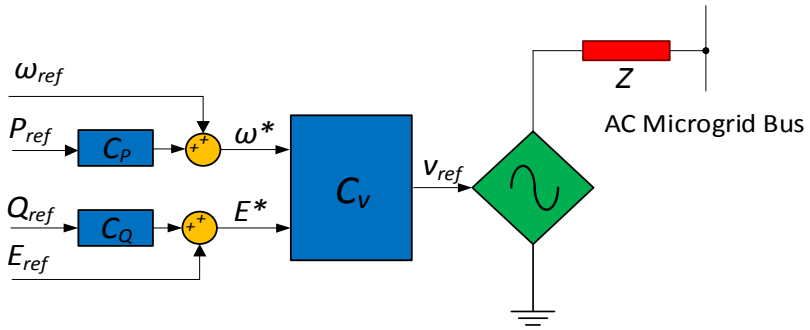

(a) Voltage-Controlled Grid-Supporting converter

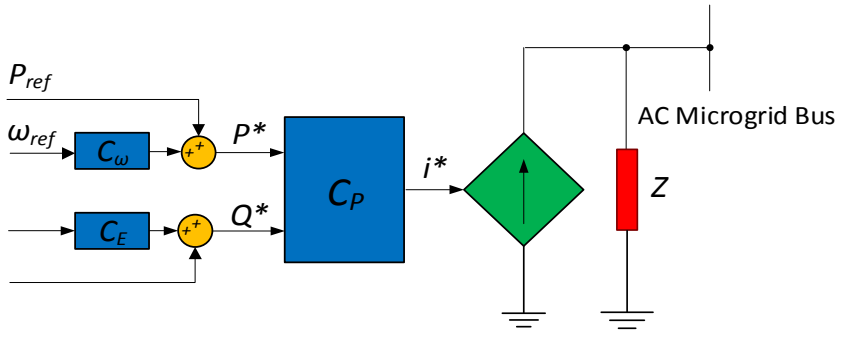

(b) Current-Controlled Grid-Supporting Converter

Figure 4.4 Grid-Supporting power Converter Representation.

In the grid-forming mode, the inverter utilizes a closed-loop cascade synchronous control structure shown in Figure 4.5. The measured grid voltages and currents are transformed to their equivalent dc inputs in the dq synchronous frame. The voltage amplitude and frequency at the point of common coupling (PCC) are set by the designer by using a reference voltage V^* and reference frequency ω^* which are used as inputs to the controller. The cascade control consists of a fast inner current control loop which regulates the amount of current supplied by the converter and an outer voltage control loop that ensures that the ac grid voltage matches the reference voltage [17]. Proportional Integral (PI) controllers are utilized to ensure zero steady-state error of the voltages and currents.

The grid-feeding mode allows the inverter to act as a power source and it is designed such that reactive and active power is delivered to the energized grid which is achieved by adjusting the reference active power P^* and the reference reactive power Q^* given by equations 4.1 and 4.2. This mode of operation also utilizes the synchronous cascade control methodology. The inner current control loop regulates the current injected into the grid and the external voltage control loop sets the reference current to deliver power to the grid. Similarly, PI controllers are incorporated to ensure a zero steady-state error. Figure 4.6 illustrates the control structure of the grid-feeding mode for the dc-ac voltage source inverter. One limitation of this traditional dual loop current control method is that for unbalanced grid conditions the PI controllers are not able to regulate oscillations that appear in the dq voltage and current signals.

$$P = v_d i_d + v_q i_q \tag{4.1}$$

$$Q = v_d i_q - v_q i_d i_q \tag{4.2}$$

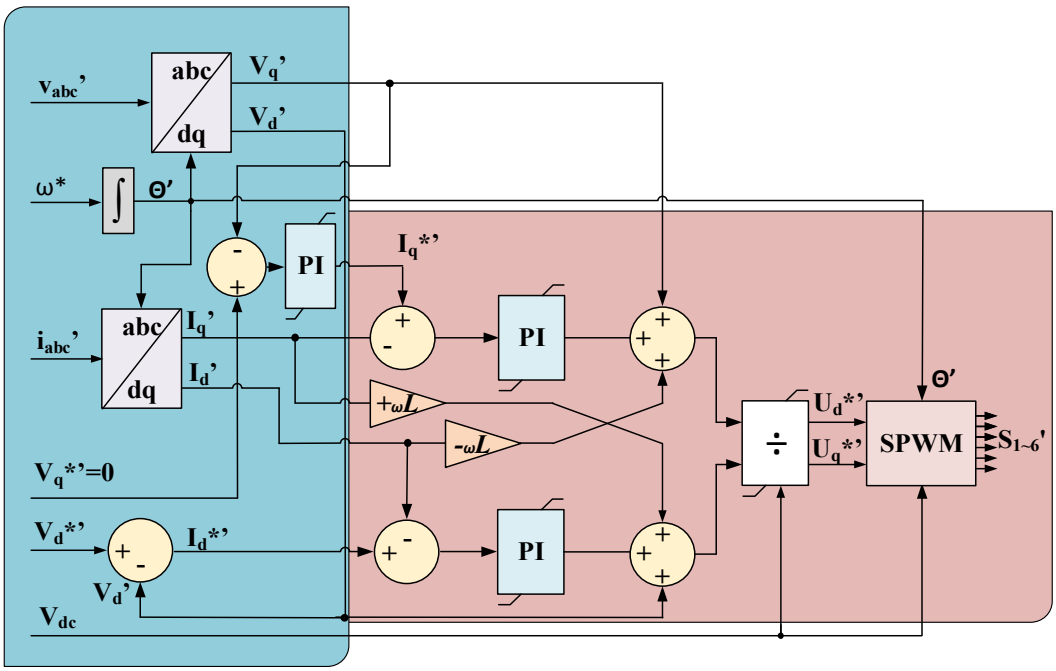

Figure 4.5 Control structure Voltage Source Inverter in Grid-Forming Mode [6].

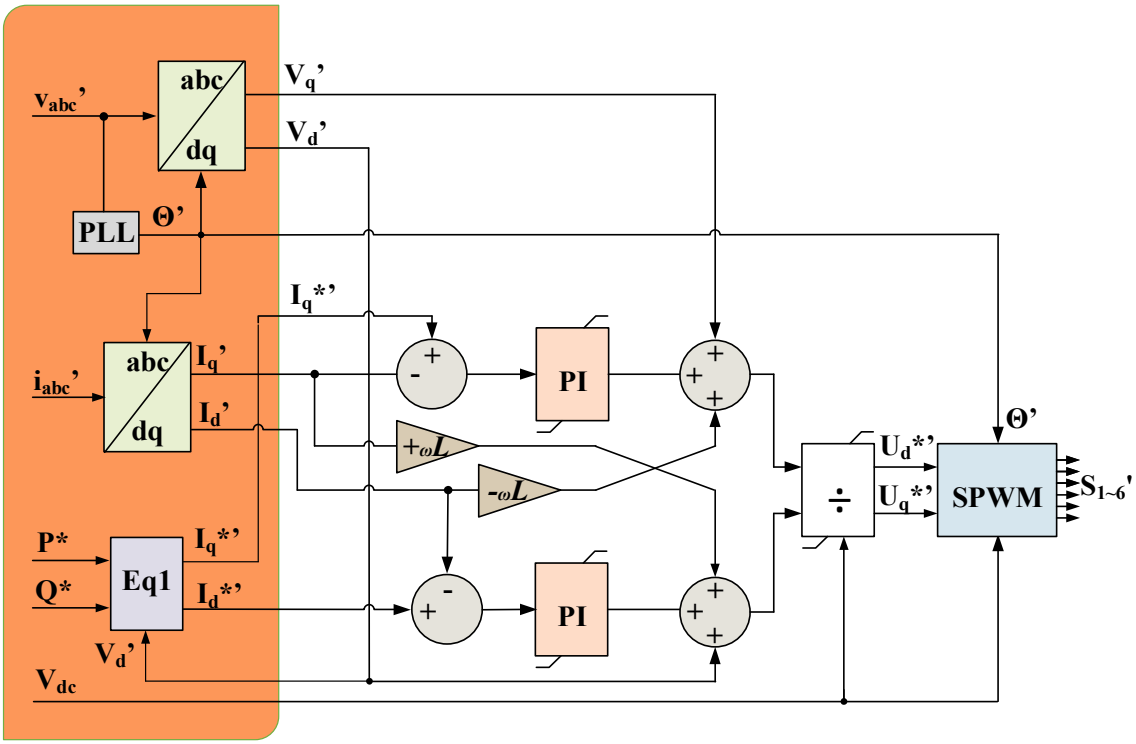

Figure 4.6 Control Structure of Voltage Source Inverter in Grid-Feeding Mode [6].

4.3 Pulse-Width Modulation Techniques of Voltage Source Converters

Pulse width modulation techniques are used in controlling many single-phase and three-phase systems. More specifically, it is used in modulating the fundamental component of the output voltage while reducing the harmonics in current and voltage waveforms. Examples of the most common PWM techniques are sinusoidal pulse-width modulation (SPWM), selective harmonics elimination (SHE), and space vector pulse-width modulation (SVPWM).

The sinusoidal pulse width modulation technique (SPWM) will be used in the circuit implementation and is used for producing an inverter output voltage that is sinusoidal with a controllable magnitude and frequency. The SPWM scheme is implemented by comparing a sinusoidal control signal $v_{control}$ at a desired frequency with a triangular waveform v_{tri} at a selected carrier frequency [55]. The purpose of the control signal $v_{control}$ is to regulate the duty ratio that contains the desired fundamental frequency of the inverter output voltage. On the other hand, the switching frequency of the inverter is establish by the triangular waveform v_{tri}. Figure 4.7 shows an example of the sinusoidal pulse-width modulation. Usually the output voltage of the inverter is not a perfect sine wave and harmonics frequencies are present hence an amplitude modulation ratio m_a is necessary to keep the harmonics in the output voltage at a minimum which is designed to within the linear modulation range.

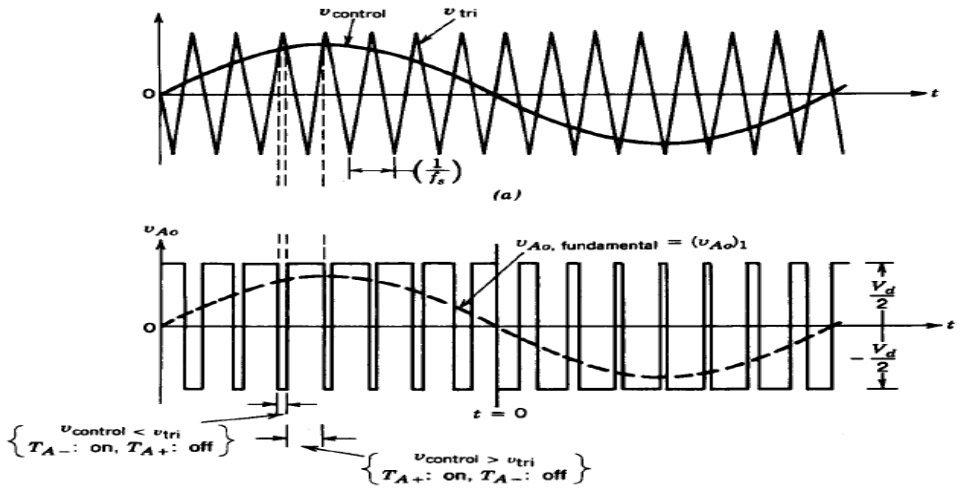

Figure 4.7 Sinusoidal Pulse Width Modulation [55].

The linear range of the modulation ratio occurs when $m_a \leq 1.0$. Outside of this range harmonics are pushed in to the high-frequency range around the switching frequency. If $m_a >$ 1.0 then overmodulation occurs resulting in more harmonics in the output voltage.

The modulation ratio is defined as

$$m_a = \frac{V_{control\ (peak)}}{V_{tri\ (peak)}} \ . \tag{4.3}$$

where $V_{control}$ and V_{tri} are the peak amplitudes of the control signal and triangular waveform respectively. Sinusoidal pulse width modulation can be implemented using unipolar and bipolar voltage switching. During unipolar switching the output voltage changes between zero and $+V_d$ or between zero and $-V_d$ voltages levels. The advantage of unipolar switching is the doubling of the switching frequency of the lower harmonics in the output voltage. Hence in the case of single phase inverter if the voltage waveforms are 180° out of phase with each other there would be a cancellation of the harmonic component at the switching frequency of the output voltage. On the other hand, during bipolar voltage switching the output volatge switches between $-V_d$ and $+V_d$ voltage levels [55].

4.4 Park's and Clarke's Transformations

A common mathematical tool for controlling three-phase voltage source converters is through the implementation of Park's transformation. The Park's Transformation is performed in two steps [56]. The first step uses Clarke's transformation to convert balanced three-phase quantities from the three-phase abc stationary reference frame into two-phase balanced quantities in the stationary reference frame. The balanced two-phase stationary variables of the Clarkes' transformation are denoted as α and β which are orthogonal hence the two-phase stationary frame is also referred to as the orthogonal reference frame. The α and β axis are also located in the same plane as the three phase reference frame. The transformation matrix from the abc stationary reference frame to the $\alpha\beta$ orthogonal reference frame is given by

$$\begin{bmatrix}\alpha\\ \beta\\ 0\end{bmatrix} = \sqrt{\frac{2}{3}}\begin{bmatrix}1 & -\frac{1}{2} & -\frac{1}{2}\\ 0 & \frac{\sqrt{3}}{2} & -\frac{\sqrt{3}}{2}\\ \frac{1}{\sqrt{2}} & \frac{1}{\sqrt{2}} & \frac{1}{\sqrt{2}}\end{bmatrix}\begin{bmatrix}a\\ b\\ c\end{bmatrix}, \tag{4.4}$$

The next step in the Park's transformation is the transformation from the two-axis orthogonal frame $\alpha\beta$ to a two-axis synchronously rotating reference frame dq. This is achieved by applying an axis rotation multiplied by the Clarke transform given in equation 4.4 where θ (rotation angle) is the integral of the fundamental angular speed ω. The transformational is matrix given in equation 4.5. The result of this rotation is that the time-varying signals are transformed into dc variables. The transformation matrix from the $\alpha\beta$ orthogonal reference frame to the dq rotating reference frame is given by

$$\begin{bmatrix}d\\ q\\ 0\end{bmatrix} = \begin{bmatrix}\cos(\theta) & \sin(\theta) & 0\\ -\sin(\theta) & \cos(\theta) & 0\\ 0 & 0 & 1\end{bmatrix}\begin{bmatrix}\alpha\\ \beta\\ 0\end{bmatrix}, \tag{4.5}$$

The full transformation from abc to dq is displayed in equation 4.6. Similarly, the inverse Park's transform can be obtained by performing the inverse of the transformations as displayed in equation 4.7. The stationary, orthogonal and rotating reference frames are displayed in Figure 4.8.

$$\begin{bmatrix} d \\ q \\ 0 \end{bmatrix} = \sqrt{\frac{2}{3}} \begin{bmatrix} \cos(\theta) & \cos(\theta - \frac{2\pi}{3}) & \cos(\theta + \frac{2\pi}{3}) \\ -\sin(\theta) & -\sin(\theta - \frac{2\pi}{3}) & -\sin(\theta + \frac{2\pi}{3}) \\ \frac{1}{\sqrt{2}} & \frac{1}{\sqrt{2}} & \frac{1}{\sqrt{2}} \end{bmatrix} \begin{bmatrix} a \\ b \\ c \end{bmatrix}, \tag{4.6}$$

$$\begin{bmatrix} a \\ b \\ c \end{bmatrix} = \sqrt{\frac{2}{3}} \begin{bmatrix} \cos(\theta) & -\sin(\theta) & \frac{1}{\sqrt{2}} \\ \cos(\theta - \frac{2\pi}{3}) & -\sin(\theta - \frac{2\pi}{3}) & \frac{1}{\sqrt{2}} \\ \frac{1}{\sqrt{2}} & -\sin(\theta + \frac{2\pi}{3}) & \frac{1}{\sqrt{2}} \end{bmatrix} \begin{bmatrix} d \\ q \\ 0 \end{bmatrix}, \tag{4.7}$$

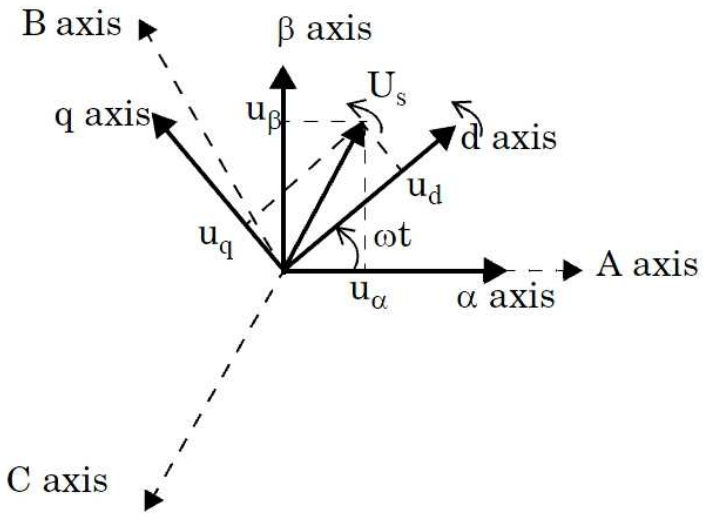

Figure 4.8 Stationary, Orthogonal and Rotating Reference Frame [14].

4.5 Phase-Locked Loop

Grid-connected converter systems such as inverters, rectifiers, and back-to-back converters require accurate and fast detection of the utility grid's voltage amplitude, frequency, and phase angle, which are paramount in the operation of these grid-connected systems [56],[57],[49]. In some instances, the grid frequency can fluctuate in a power system that contains a considerable amount of distributed energy resources in the case of a fault [58]. Hence, the grid must be synchronized to accommodate such events. The conventional synchronization method used is called the phase-locked loop control. The phase-locked loop control synchronizes the inverter output current and rectifier input current with the grid voltage ensuring unity power factor. For three-phase applications, the synchronous reference frame phase-locked loop (SRF-PLL) is widely used.

4.5.1 Synchronous Reference Frame Phase Locked Loop

The synchronously rotating reference frame phase-locked loop (SRF-PLL) is based on a closed-loop configuration where the measured three-phase grid voltages are taken as inputs to the phase locked loop of which the angle of the phase 'a' voltage is used to determine the rotational angle θ. The rotational angle is the tracked phase angle, which is used in the Park's and Clarkes transformation in the implementation of the PLL by integrating the grid frequency ω' [59]. Typically the quadrature-axis component V_q of the synchronously rotating dq frame is fed to a PI controller to achieve reference value of 0 in the steady state. The quadrature-axis component V_q locks the rotation of the synchronous frame to a specific position with the three-phase stationary frame and produces the desired dc reference value of the direct axis component [56],[60]. The output of the loop filter is the estimated frequency ω' and is integrated to obtain the estimated

phase angle θ'. Figure 4.9 shows a block diagram of the synchronously rotating reference frame phase-locked loop [61].

4.5.2 Dual Second Order Generalized Integrator Frequency Locked Loop

When utility grids are unbalanced the synchronous reference frame technique becomes deteriorated and is not able to accurately track the positive and negative sequences of the grid voltage which is essential in controlling grid-connected power converters in microgrid systems. In grid-forming mode the synchronization should be able to perform well on grid-connected and islanded modes allowing the converter to maintain a stable voltage in the microgrid. In grid-feeding mode, the voltage source converter connected to the microgrid will experience frequency dips and phase angle transients thus a robust synchronization method must be selected to ensure stability during this mode of operation.

The dual second order generalized integrator frequency-locked-loop (DSOGI-FLL) is chosen as the desired synchronization method [62]. The DSOGI-FLL is formed by combining two synchronization methods i.e. a second order generalized integrator for quadrature-signals generators (SOGI-QSG) and a frequency locked loop (FLL). The DSOGI-FLL converts three-phase voltages from stationary to the orthogonal $\alpha\beta$ reference frame. The SOGI-QGS acts as a bandpass filter obtaining filtered versions of the $\alpha\beta$ grid voltages, $v'_{\alpha\beta}$ and $qv'_{\alpha\beta}$. The frequency locked loop detects the grid frequency ω' which is used in the SOGI-QSG transformation and the filtered phase voltages are sent to positive/negative sequence calculators. Figure 4.10 displays the block diagram of the DSOGI-FLL.

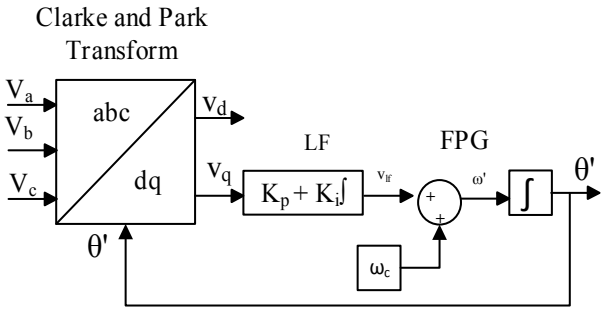

Figure 4.9 Synchronous Reference Frame Phase-Locked Loop.

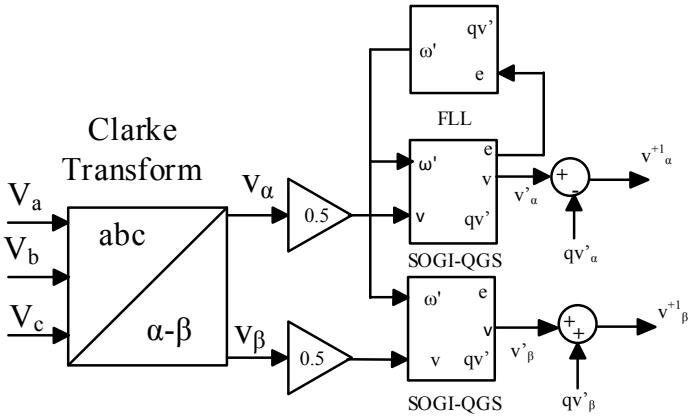

Figure 4.10 Double Second Order Generalized Integrator Frequency-Locked Loop.

4.6 Summary

This chapter presents an overview of the two-level back-to-back voltage source converter and the proportional integral control method for voltage source converters in AC microgrid systems. A theoretical background of reference frame transformations, pulse width modulation methods, and grid synchronization techniques are also presented. The concepts used in the chapter will be used in designing the passivity-based controller in Chapter six and Chapter seven.

CHAPTER FIVE

NOVEL STABILITY THEOREMS FOR CASCADED POWER CONVERTERS IN WEAK AC MICROGRID SYSTEMS

5.1 Introduction

Novel stability theorems are derived for cascaded converters in voltage source converter-based microgrid systems to address dc link voltage regulation in weak grid systems. A brief review of microgrid circuit topologies is presented in addition to a linearized model of the virtual microgrid configuration of the NCREPT system. The NCREPT microgrid configuration can be viewed as baseline model comprising of various microgrid topologies. A robust analysis using the edge theorem is presented to demonstrate the system's stability with a weak grid connection using parametric uncertainty. Additionally, an eigenvalue analysis of the derived 24^{th} order mathematical model of the NCREPT system is also investigated to illustrate the systems' stability under grid impedance variation. Using the principle of passivity in physical systems and Port-Hamiltonian systems discussed in chapters two and three respectively, it is proven that the stability analysis theorem for the NCREPT microgrid configuration is valid for all members of the class of voltage source converter-based microgrid systems.

5.2 Microgrid Circuit Topologies

Microgrids are categorized as ac, dc, and hybrid ac/dc configurations. Figure 5.1 illustrates the AC microgrid configuration where distributed energy resources are interfaced to voltage source converters, which are connected in parallel to provide power to the load for islanded mode operations. In grid-connected mode, the load is powered by the utility grid interface. The multi-terminal hybrid ac/dc shown in Figure 5.2 can be viewed as a combination of a hybrid ac/dc feeder and dc microgrid. The voltage source converters convert the incoming three-phase ac power to dc

power, which feeds the multiple dc loads at the dc bus terminals. The hybrid ac/dc feeder in Figure 5.3 combines the back-to-back voltage source converters such that loads are connected to various ac or dc parts of the feeder. The networked ac microgrid shown in Figure 5.4 is also a hybrid ac/dc configuration which provides power to various loads under fault conditions.

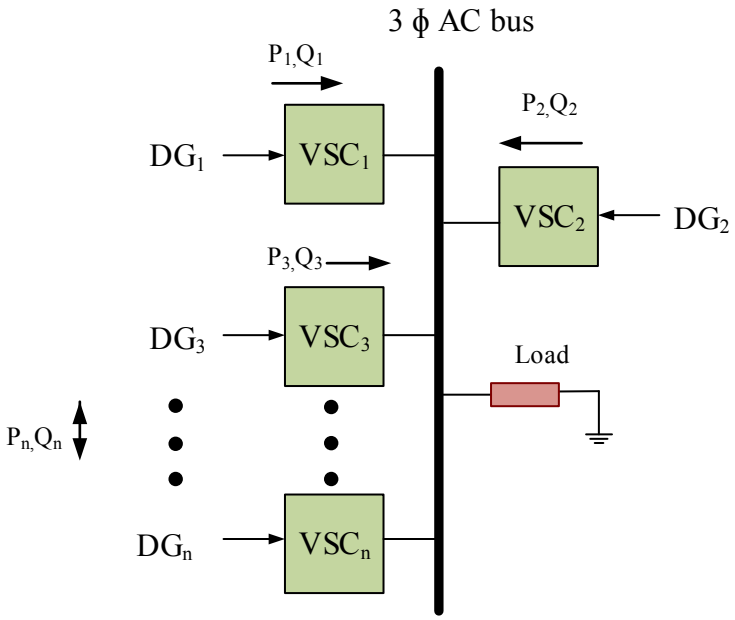

Figure 5.1 AC Microgrid Parallel Configuration.

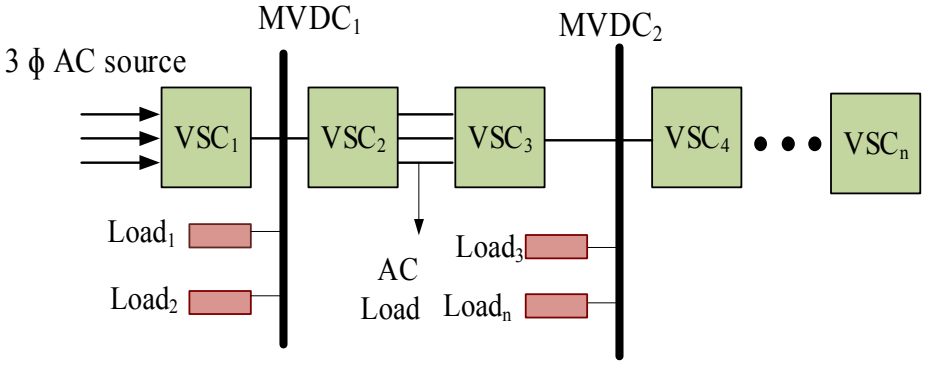

Figure 5.2 Multi-Terminal Hybrid AC/DC Microgrid.

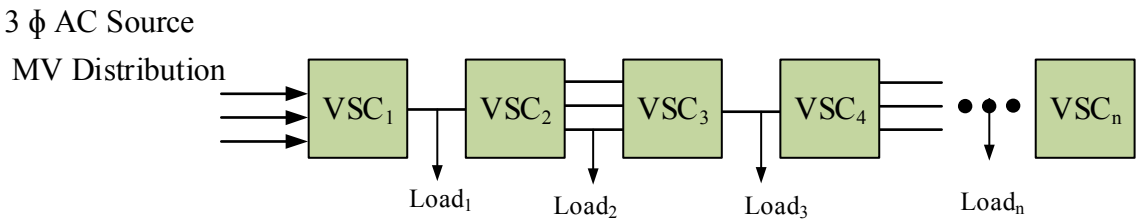

Figure 5.3 Hybrid AC/DC Microgrid.

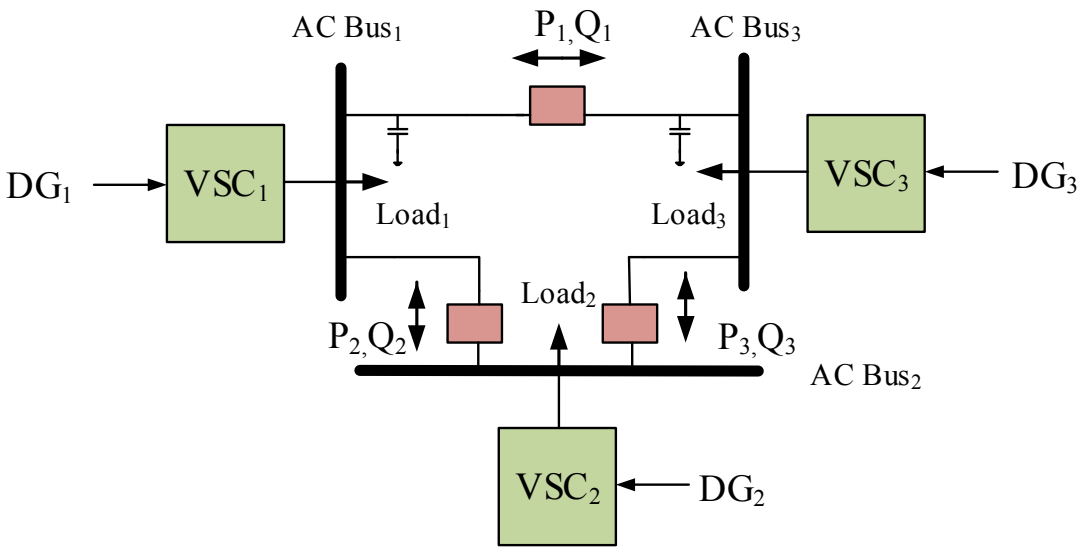

Figure 5.4 Networked Hybrid AC/DC Microgrid.

5.3 Stability Theorems for Interconnected VSCs in Microgrid Systems

Stability theorems are proposed for interconnected voltage source converters in microgrid systems using the principle of Dirac structures. The NCREPT system having characteristics of the ac, dc and hybrid ac/dc microgrid configuration is used as a benchmark for showing that all classes of VSC-based microgrids can be stabilized using the passivity-based control method which leads to Corollary 5.1

Corollary 5.1: All physical systems are a combination of subsystems constituted by the composition of Dirac structures in which all Dirac structures are inherently passive hence, the sum of series or parallel subsystems are passive leading to stability based on the energy-balancing concept in [45].

The Dirac composition structure is presented in Figure 5.5 with detailed proof of the theorem presented by Cervera et al. in [63]. A Dirac structure is a power conserving interconnection of storage and dissipative elements in a physical system. The vector spaces e and f represent the effort and flows in the system, which are typically represented as voltages and currents in electrical systems as mentioned in chapter three.

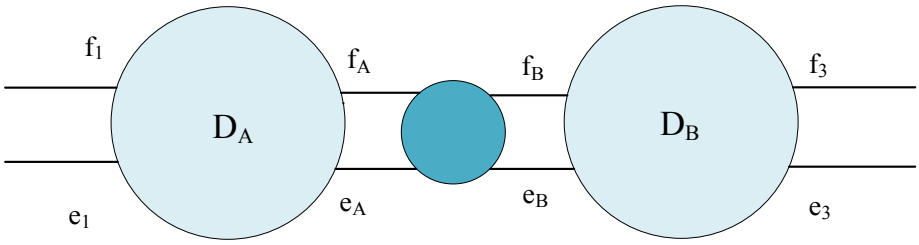

Figure 5.5. Composition of Dirac structure

Assuming that the energy variables are in a linear space X the vector of flows of the energy storing elements is defined as $\dot{x}$ while the vector of efforts of the energy storing is given as $\frac{\partial H}{\partial x}(x)$ .The total energy balance of the energy storing elements is given by

$$\frac{dH}{dt}\big(x(t)\big) = \frac{\partial^T H}{\partial x}\big(x(t)\big)\dot{x}(t) \tag{5.1}$$

which leads to the Port-Hamiltonian dynamical system

$$\left(-\dot{x}(t), \frac{\partial H}{\partial x}(t), f(t), e(t)\right) \epsilon\, D \tag{5.2}$$

From Theorem 3 in [63], the composition of two Dirac structures is again a Dirac structure defined by

$$D \coloneqq D_A || D_B = (D_A || D_B)^{\perp} \tag{5.3}$$

Hence from Figure 5.5 the incoming power in the Dirac structure D_A is equal to the outgoing power D_B were the relationship between the efforts e_A, e_B and flows f_A and f_B on vector spaces of shared effort variables F_2^* and shared flow variables F_2 are described as

$$f_A = -f_B \, \epsilon \, F_2 \tag{5.4}$$

$$e_A = -e_B \, \epsilon \, F_2^* \tag{5.5}$$

The individual stored energies of D_A and D_B leads to a total energy or the Hamiltonian energy of the system.

***Theorem 5.1**: Voltage source converter-based hybrid ac/dc microgrid systems are Dirac Port-Hamiltonian Systems.*

Proof: This result directly follows from Theorem 3 in [63].

Consider the one-line diagrams of the VVVVF drive and REGEN bench configuration of the NCREPT microgrid system displayed in Figures 5.6-5.7. The one-line diagrams are viewed as having characteristics of a networked AC microgrid system and a hybrid ac/dc microgrid system shown in Figure 5.8.

Assumption 5.1: The lumped parameter systems shown in Figure 5.6 and Figure 5.7 are balanced and the voltage source converters of the VVVF drive and REGEN bench represents lossless Dirac structures D_1 and $D_2$with ideal switches $S_{1i}, S_{2i} S_{3i}, S_{4i}$. The energy dissipative structure R_i is represented by the resistances in the system and the energy storage structure S_i are represented by the inductors and capacitors in the systems. The port pairs (e, f) represent the power flow in the system where the effort e of the system are the voltages of the dissipative and storage

elements given by V_i,V_{1i}, V_{2i},V_{3i}, V_{4i} and the flow f is the current flow in the dissipation and storage elements of the system given by $i_{1i}i_{2i}i_{3i}i_{4i}i_{5i,}i_{6i}$, i_{7i}, i_{8i} . The external inputs $u_{1i}, u_{2i}, u_{3i}, u_{4i}$ are the modulation indices used to control the voltage source converters in the microgrid.

The total energy or Hamiltonian H(x) is therefore given by

$$H(x) = \frac{1}{2}\, L_i^2 \, + \frac{1}{2} C_i^2 \tag{5.6}$$

where L_i and C_i are the sum of the inductances and capacitances in the system.

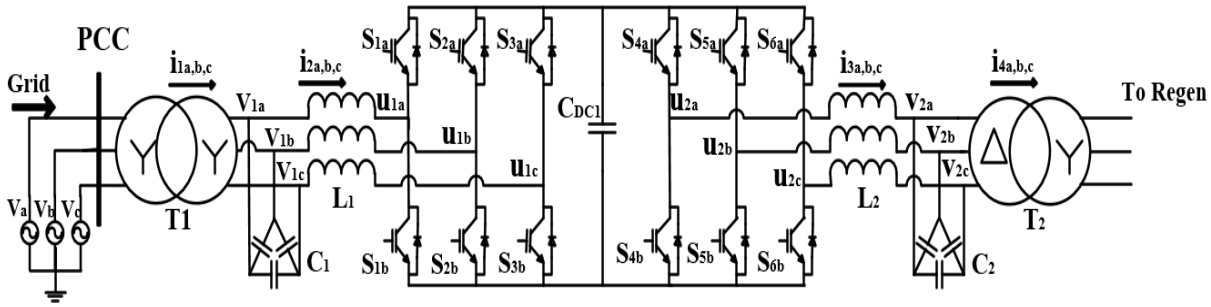

Figure 5.6 Three-phase equivalent circuit for VVVF drive.

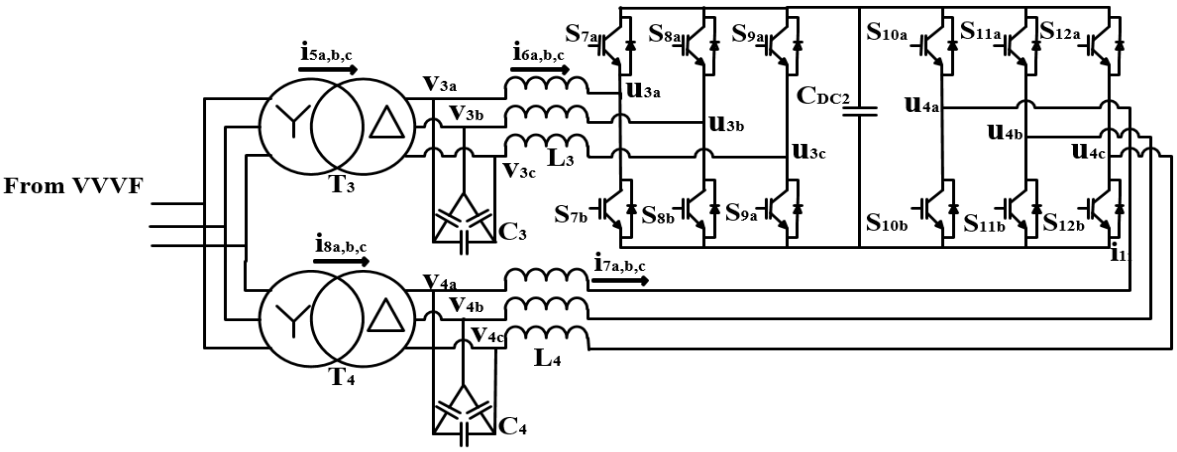

Figure 5.7 Three-phase circuit for REGEN bench.

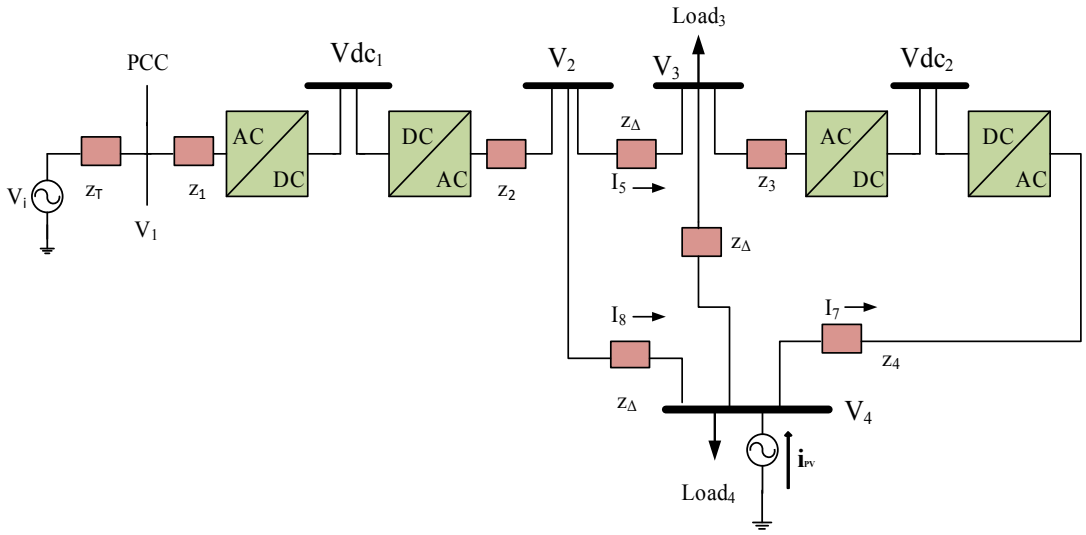

Figure 5.8. Block diagram representation of NCREPT system.

According to Theorem 3 [63], the composition of two Dirac structures is again a Dirac structure then the composition of n Dirac structures is again a Dirac structure. Additionally, the interconnection of n port-hamiltonian systems through the interconnection Dirac D_i defines another Port-Hamiltonian system with Dirac structure D [39]. Hence without loss of generality the one-line diagrams Figure 5.6 and Figure 5.7 can be viewed as an interconnection of Dirac structures of the VVVF drive and REGEN bench such that

$$D_{VVVF} \coloneqq D_{RECT_1} || D_{INV_1} = (D_{RECT_1} || D_{INV_1})^{\perp} \tag{5.7a}$$

$$D_{REGEN} \coloneqq D_{RECT_2} || D_{INV_2} = (D_{RECT_2} || D_{INV_2})^{\perp} \tag{5.7b}$$

$$D_{microgrid} \coloneqq D_{VVVF} || D_{REGEN} = (D_{VVVF} || D_{REGEN})^{\perp} \tag{5.7c}$$

$$H_{microgrid} \coloneqq H_{VVVF} + H_{REGEN} \tag{5.7d}$$

which concludes that the voltage source converter-based hybrid AC/DC NCREPT microgrid system is a Dirac Port-Hamiltonian System. Passivity is also a property of the Dirac structure hence the VSC-based hybrid ac/dc microgrid system is also passive Thus it can also be concluded that all VSC-based microgrid systems are passive Dirac-Port Hamiltonian systems.

Theorem 5.2: **VSC-based hybrid ac/dc microgrid are input-affine nonlinear systems**

Proof: This result directly follows from Definition 10.1 in [39] where the input-output Hamiltonian system with dissipation is an affine system. Using Theorem 5.1 where the sum of Port-Hamiltonian systems of the hybrid ac/dc NCREPT microgrid system is another Port-Hamiltonian system then VSC-based hybrid ac/dc microgrid systems are also input-affine nonlinear systems.

5.4 Robust Analysis of the NCREPT Microgrid Configuration

In weak grid systems, the short circuit ratio of the grid impedance typically indicates if the grid is stiff or weak when handling voltage variations. To determine if a system is robustly stable many analytical methods such as root locus, eigenvalue analysis, impedance-based analysis and parametric uncertainty can be employed. In the case of the NCREPT system microgrid configuration, the grid impedance consists of the 5% transformer impedance, which can vary due to aging over time. Hence, a stability analysis of the NCREPT system can be demonstrated to observe how the system reacts to a varying transformer impedance, which ultimately affects the VVVF drives' ability to maintain a constant dc voltage during operation. An eigenvalues analysis of the system is implemented to determine how the system responds to varying transformer impedances. The transformer impedance variation also leads to the implementation of the concept of parametric uncertainty using the edge theorem which is discussed later in the chapter.

The nonlinear mathematical model of the microgrid configuration shown in Figure 5.6 was derived in [64]. The mathematical model in the stationary reference frame was converted via parks transformation to the d-q synchronous rotating frame producing a 24^{th} order system. The system is then linearized using a Taylor series expansion around the system's equilibrium point to reduce the model complexity for control implementation. The linearized system is given as

$$\Delta\dot{x} = \bar{A}\Delta x + \bar{B}\Delta u + \bar{F}\Delta u_d, \tag{5.9a}$$

$$\Delta y = \bar{C}\Delta x \tag{5.9b}$$

The state error is given by $\Delta x = x - \bar{x} \in \mathbb{R}^n$, the input error is $\Delta u = u - \bar{u} \in \mathbb{R}^n$, the disturbance input error is $\Delta u = u_d - \bar{u}_d \in \mathbb{R}^n$ and $\bar{A} \in \mathbb{R}^n$, $\bar{B} \in \mathbb{R}^n, \bar{C} \in \mathbb{R}^n, \bar{F} \in \mathbb{R}^n$, are concatenated matrices which represent the state matrix elements, input matrix elements, disturbance matrix elements and output matrix elements respectively which are shown in equations 5.10-5.20 the matrices values are given in Appendix A.

$$\left.\frac{\partial \mathrm{f}}{\partial \mathrm{x}}\right|_{(\bar{\mathrm{x}},\bar{\mathrm{u}})} = \begin{bmatrix} \bar{\mathrm{A}}_{11} & \bar{\mathrm{A}}_{12} \\ \bar{\mathrm{A}}_{21} & \bar{\mathrm{A}}_{22} \end{bmatrix}$$

where:

$$\bar{\mathbf{A}}_{\mathbf{11}} = \begin{bmatrix} -\frac{\mathrm{R_T}}{\mathrm{L_T}} & \omega & 0 & 0 & 0 & 0 & 0 & 0 & 0 & 0 & 0 & 0 \\ -\omega & -\frac{\mathrm{R_T}}{\mathrm{L_T}} & 0 & 0 & 0 & 0 & 0 & 0 & 0 & 0 & 0 & 0 \\ 0 & 0 & -\frac{\mathrm{R_1}}{\mathrm{L_1}} & \omega & 0 & 0 & 0 & 0 & 0 & 0 & 0 & 0 \\ 0 & 0 & -\omega & -\frac{\mathrm{R_1}}{\mathrm{L_1}} & 0 & 0 & 0 & 0 & 0 & 0 & 0 & 0 \\ 0 & 0 & 0 & 0 & -\frac{\mathrm{R_2}}{\mathrm{L_2}} & \omega & 0 & 0 & 0 & 0 & 0 & 0 \\ 0 & 0 & 0 & 0 & -\omega & -\frac{\mathrm{R_2}}{\mathrm{L_2}} & 0 & 0 & 0 & 0 & 0 & 0 \\ 0 & 0 & 0 & 0 & 0 & 0 & -\frac{\mathrm{R}}{\mathrm{L}} & \omega & 0 & 0 & 0 & 0 \\ 0 & 0 & 0 & 0 & 0 & 0 & -\omega & -\frac{\mathrm{R}}{\mathrm{L}} & 0 & 0 & 0 & 0 \\ 0 & 0 & 0 & 0 & 0 & 0 & 0 & 0 & -\frac{\mathrm{R}}{\mathrm{L}} & \omega & 0 & 0 \\ 0 & 0 & 0 & 0 & 0 & 0 & 0 & 0 & -\omega & -\frac{\mathrm{R}}{\mathrm{L}} & 0 & 0 \\ 0 & 0 & 0 & 0 & 0 & 0 & 0 & 0 & 0 & 0 & -\frac{\mathrm{R_3}}{\mathrm{L_3}} & \omega \\ 0 & 0 & 0 & 0 & 0 & 0 & 0 & 0 & 0 & 0 & -\omega & -\frac{\mathrm{R_3}}{\mathrm{L_3}} \end{bmatrix} \tag{5.10}$$

$$\bar{A}_{12} = \begin{bmatrix} 0 & 0 & 0 & 0 & -\frac{1}{L_T} & 0 & 0 & 0 & 0 & 0 & 0 & 0 \\ 0 & 0 & 0 & 0 & 0 & -\frac{1}{L_T} & 0 & 0 & 0 & 0 & 0 & 0 \\ 0 & 0 & -\frac{\bar{\mu}_{1d}}{L_1} & 0 & \frac{1}{L_1} & 0 & 0 & 0 & 0 & 0 & 0 & 0 \\ 0 & 0 & -\frac{\bar{\mu}_{1q}}{L_1} & 0 & 0 & \frac{1}{L_1} & 0 & 0 & 0 & 0 & 0 & 0 \\ 0 & 0 & \frac{\bar{\mu}_{2d}}{L_1} & 0 & 0 & 0 & -\frac{1}{L_2} & 0 & 0 & 0 & 0 & 0 \\ 0 & 0 & \frac{\bar{\mu}_{2q}}{L_1} & 0 & 0 & 0 & 0 & -\frac{1}{L_2} & 0 & 0 & 0 & 0 \\ 0 & 0 & 0 & 0 & 0 & 0 & \frac{2}{3L} & 0 & -\frac{1}{3L} & 0 & -\frac{1}{3L} & 0 \\ 0 & 0 & 0 & 0 & 0 & 0 & 0 & \frac{2}{3L} & 0 & -\frac{1}{3L} & 0 & -\frac{1}{3L} \\ 0 & 0 & 0 & 0 & 0 & 0 & \frac{1}{3L} & 0 & -\frac{2}{3L} & 0 & \frac{1}{3L} & 0 \\ 0 & 0 & 0 & 0 & 0 & 0 & 0 & \frac{1}{3L} & 0 & -\frac{2}{3L} & 0 & \frac{1}{3L} \\ 0 & 0 & 0 & -\frac{\bar{\mu}_{3d}}{L_3} & 0 & 0 & 0 & 0 & \frac{1}{L_3} & 0 & 0 & 0 \\ 0 & 0 & 0 & -\frac{\bar{\mu}_{3q}}{L_3} & 0 & 0 & 0 & 0 & 0 & \frac{1}{L_3} & 0 & 0 \end{bmatrix} \quad (5.11)$$

$$\bar{\mathbf{A}}_{21} = \begin{bmatrix} 0 & 0 & 0 & 0 & 0 & 0 & 0 & 0 & 0 & 0 & 0 & 0 \\ 0 & 0 & 0 & 0 & 0 & 0 & 0 & 0 & 0 & 0 & 0 & 0 \\ 0 & 0 & 0 & 0 & 0 & 0 & 0 & 0 & 0 & 0 & 0 & 0 \\ 0 & 0 & \frac{\bar{\mu}_{1d}}{C_{DC1}} & \frac{\bar{\mu}_{1q}}{C_{DC1}} & \frac{-\bar{\mu}_{2d}}{C_{DC1}} & \frac{-\bar{\mu}_{2q}}{C_{DC1}} & 0 & 0 & 0 & 0 & 0 & 0 \\ 0 & 0 & 0 & 0 & 0 & 0 & 0 & 0 & 0 & 0 & \frac{\bar{\mu}_{3d}}{C_{DC2}} & \frac{\bar{\mu}_{3q}}{C_{DC2}} \\ \frac{1}{C_1} & 0 & -\frac{1}{C_1} & 0 & 0 & 0 & 0 & 0 & 0 & 0 & 0 & 0 \\ 0 & \frac{1}{C_1} & 0 & -\frac{1}{C_1} & 0 & 0 & 0 & 0 & 0 & 0 & 0 & 0 \\ 0 & 0 & 0 & 0 & \frac{1}{C_2} & 0 & -\frac{1}{C_2} & 0 & 0 & 0 & 0 & 0 \\ 0 & 0 & 0 & 0 & 0 & \frac{1}{C_2} & 0 & -\frac{1}{C_2} & 0 & 0 & 0 & 0 \\ 0 & 0 & 0 & 0 & 0 & 0 & 0 & 0 & \frac{1}{C_3} & 0 & -\frac{1}{C_3} & 0 \\ 0 & 0 & 0 & 0 & 0 & 0 & \frac{1}{C_4} & 0 & -\frac{1}{C_4} & 0 & 0 & 0 \\ 0 & 0 & 0 & 0 & 0 & 0 & 0 & \frac{1}{C_4} & 0 & -\frac{1}{C_4} & 0 & 0 \end{bmatrix} \quad (5.12)$$

$$\bar{\mathbf{A}}_{\mathbf{22}} = \begin{bmatrix} -\frac{R_4}{L_4} & \omega & 0 & -\frac{\bar{\mu}_{4d}}{L_4} & 0 & 0 & 0 & 0 & 0 & 0 & \frac{1}{L_4} & 0 \\ -\omega & -\frac{R_4}{L_4} & 0 & -\frac{\bar{\mu}_{4q}}{L_4} & 0 & 0 & 0 & 0 & 0 & 0 & 0 & \frac{1}{L_4} \\ 0 & 0 & 0 & 0 & 0 & 0 & 0 & 0 & 0 & 0 & 0 & 0 \\ \frac{\bar{\mu}_{4d}}{C_{DC2}} & \frac{\bar{\mu}_{4q}}{C_{DC2}} & 0 & 0 & 0 & 0 & 0 & 0 & 0 & 0 & 0 & 0 \\ 0 & 0 & 0 & 0 & 0 & \omega & 0 & 0 & 0 & 0 & 0 & 0 \\ 0 & 0 & 0 & 0 & -\omega & 0 & 0 & 0 & 0 & 0 & 0 & 0 \\ 0 & 0 & 0 & 0 & 0 & 0 & 0 & \omega & 0 & 0 & 0 & 0 \\ 0 & 0 & 0 & 0 & 0 & 0 & -\omega & 0 & 0 & 0 & 0 & 0 \\ 0 & 0 & 0 & 0 & 0 & 0 & 0 & 0 & -\frac{1}{R_{L1}C_3} & \omega & 0 & 0 \\ 0 & 0 & 0 & 0 & 0 & 0 & 0 & 0 & -\omega & -\frac{1}{R_{L1}C_3} & 0 & 0 \\ -\frac{1}{C_4} & 0 & 0 & 0 & 0 & 0 & 0 & 0 & 0 & 0 & -\frac{1}{R_{L2}C_4} & \omega \\ 0 & -\frac{1}{C_4} & 0 & 0 & 0 & 0 & 0 & 0 & 0 & 0 & -\omega & -\frac{1}{R_{L2}C_4} \end{bmatrix} \quad (5.13)$$

$\bar{\mathrm{B}} = \left.\frac{\partial \mathrm{f}}{\partial \mathrm{u}}\right|_{(\bar{\mathrm{x}},\bar{\mathrm{u}},\bar{\mathrm{u}}_\mathrm{d})} = \begin{bmatrix} \bar{\mathrm{B}}_{11} \\ \bar{\mathrm{B}}_{21} \end{bmatrix}$ where:

$$\bar{\mathbf{B}}_{\mathbf{11}} = \begin{bmatrix} 0 & 0 & 0 & 0 & 0 & 0 & 0 & 0 \\ 0 & 0 & 0 & 0 & 0 & 0 & 0 & 0 \\ -\frac{\bar{v}_{DC1}}{L_1} & 0 & 0 & 0 & 0 & 0 & 0 & 0 \\ 0 & -\frac{\bar{v}_{DC1}}{L_1} & 0 & 0 & 0 & 0 & 0 & 0 \\ 0 & 0 & \frac{\bar{v}_{DC1}}{L_2} & 0 & 0 & 0 & 0 & 0 \\ 0 & 0 & 0 & \frac{\bar{v}_{DC1}}{L_2} & 0 & 0 & 0 & 0 \\ 0 & 0 & 0 & 0 & 0 & 0 & 0 & 0 \\ 0 & 0 & 0 & 0 & 0 & 0 & 0 & 0 \\ 0 & 0 & 0 & 0 & 0 & 0 & 0 & 0 \\ 0 & 0 & 0 & 0 & 0 & 0 & 0 & 0 \\ 0 & 0 & 0 & 0 & -\frac{\bar{v}_{DC2}}{L_3} & 0 & 0 & 0 \\ 0 & 0 & 0 & 0 & 0 & -\frac{\bar{v}_{DC2}}{L_3} & 0 & 0 \end{bmatrix} \quad (5.14)$$

$$\bar{\boldsymbol{B}}_{\boldsymbol{21}} = \begin{bmatrix} 0 & 0 & 0 & 0 & 0 & 0 & -\frac{\bar{v}_{DC2}}{L_4} & 0 \\ 0 & 0 & 0 & 0 & 0 & 0 & 0 & -\frac{\bar{v}_{DC2}}{L_4} \\ \frac{\bar{\imath}_{2d}}{C_{DC1}} & \frac{\bar{\imath}_{2q}}{C_{DC1}} & -\frac{\bar{\imath}_{3d}}{C_{DC1}} & -\frac{\bar{\imath}_{3q}}{C_{DC1}} & 0 & 0 & 0 & 0 \\ 0 & 0 & 0 & 0 & \frac{\bar{\imath}_{6d}}{C_{DC2}} & \frac{\bar{\imath}_{6q}}{C_{DC2}} & \frac{\bar{\imath}_{7d}}{C_{DC2}} & \frac{\bar{\imath}_{7q}}{C_{DC2}} \\ 0 & 0 & 0 & 0 & 0 & 0 & 0 & 0 \\ 0 & 0 & 0 & 0 & 0 & 0 & 0 & 0 \\ 0 & 0 & 0 & 0 & 0 & 0 & 0 & 0 \\ 0 & 0 & 0 & 0 & 0 & 0 & 0 & 0 \\ 0 & 0 & 0 & 0 & 0 & 0 & 0 & 0 \\ 0 & 0 & 0 & 0 & 0 & 0 & 0 & 0 \\ 0 & 0 & 0 & 0 & 0 & 0 & 0 & 0 \end{bmatrix} \quad (5.15)$$

$\bar{\mathbf{F}} = \frac{\partial \mathrm{f}}{\partial \mathrm{u_d}}\Big|_{(\bar{\mathrm{x}},\bar{\mathrm{u}},\bar{\mathrm{u}}_\mathrm{d})}$ where

$$\begin{bmatrix} \frac{1}{\mathrm{L_T}} & 0 & 0 & 0 & 0 & 0 & 0 & 0 & 0 & 0 & 0 & 0 & 0 & 0 & 0 & 0 & 0 & 0 & 0 & 0 & 0 & 0 & 0 & 0 \\ 0 & \frac{1}{\mathrm{L_T}} & 0 & 0 & 0 & 0 & 0 & 0 & 0 & 0 & 0 & 0 & 0 & 0 & 0 & 0 & 0 & 0 & 0 & 0 & 0 & 0 & 0 & 0 \\ 0 & 0 & 0 & 0 & 0 & 0 & 0 & 0 & 0 & 0 & 0 & 0 & 0 & 0 & 0 & 0 & 0 & 0 & 0 & 0 & 0 & 0 & \frac{1}{\mathrm{C_4}} & 0 \\ 0 & 0 & 0 & 0 & 0 & 0 & 0 & 0 & 0 & 0 & 0 & 0 & 0 & 0 & 0 & 0 & 0 & 0 & 0 & 0 & 0 & 0 & 0 & \frac{1}{\mathrm{C_4}} \end{bmatrix}^T \quad (5.16)$$

$\overline{\mathbf{C_{dc}}} =$

$$\begin{bmatrix} 0 & 0 & 0 & 0 & 0 & 0 & 0 & 0 & 0 & 0 & 0 & 0 & 0 & 0 & 1 & 0 & 0 & 0 & 0 & 0 & 0 & 0 & 0 & 0 \\ 0 & 0 & 0 & 0 & 0 & 0 & 0 & 0 & 0 & 0 & 0 & 0 & 0 & 0 & 0 & 1 & 0 & 0 & 0 & 0 & 0 & 0 & 0 & 0 \end{bmatrix}^T \quad (5.17)$$

The state variables, controller inputs and disturbance variables are given below.

$$\mathbf{x} = [\mathrm{i_{1d}} \quad \mathrm{i_{1q}} \quad . \quad . \quad . \quad \mathrm{i_{7d}} \quad \mathrm{i_{7d}} \quad \mathrm{v_{cdc1}} \quad \mathrm{v_{Cdc2}} \quad \mathrm{v_{1d}} \quad \mathrm{v_{1q}} \quad . \quad . \quad . \quad \mathrm{v_{4d}} \quad \mathrm{v_{4q}}]^{\mathrm{T}} . \quad (5.18)$$

$$\mathbf{u} = [\mu_{1\mathrm{d}} \quad \mu_{1\mathrm{q}} \quad \mu_{2\mathrm{d}} \quad \mu_{2\mathrm{q}} \quad \mu_{3\mathrm{d}} \quad \mu_{3\mathrm{q}} \quad \mu_{4\mathrm{d}} \quad \mu_{4\mathrm{q}}]^{\mathrm{T}}. \quad (5.19)$$

$$\mathbf{u_d} = [\mathrm{v_d} \quad \mathrm{v_d} \quad \mathrm{i_{PVd}} \quad \mathrm{i_{PVq}}]^{\mathbf{T}} . \quad (5.20)$$

To determine if the microgrid configuration is controllable and observable such that a robust controller can be implemented, the NCREPT system is viewed as a square system given by the definition 5.1.

Definition 5.1 *A square system* $\sum \in \mathbb{R}^{nxn}$ *can be defined as one in which the number of control inputs* u_i *equal the number of control outputs* y_i.

The control input for the microgrid system is given by

$$u_{control} = \left[u_{1d}\, u_{1q}\, u_{2d}\, u_{2q}\, u_{3d}\ \ u_{3q}\, u_{4d}\, u_{4q} \right]^T , \tag{5.21}$$

which represents the modulation indices of the rectifier and inverter in the VVVF drive and REGEN bench.

The control output for the microgrid system is given by

$$y_{control} = \left[i_{7d}\, i_{7q}\, V_{DC_1}\, V_{DC_2}\, V_{3d}\, V_{3q}\, V_{4d}\, V_{4q} \right]^T , \tag{5.22}$$

which represents the system states of interest that are to be controlled and observed.

The system is determined to be controllable and observable and a stability analysis of the microgrid system is performed using an eigenvalue analysis and the edge theorem.

5.4.1 Application of Eigenvalue Analysis for Weak Grid Analysis of NCREPT System

The stability of the closed-loop system is determined by finding the eigenvalues of the closed-loop system matrix **A** which is equivalent to finding the roots of the characteristic equation of **A** which is described by

$$s^{24} + a_{23}s^{23} + a_{22}s^{22} \ldots + a_1 s + a_0 \quad , \tag{5.23}$$

where the coefficients is a multilinear function of the system **A** matrix parameters. The coefficients of the polynomial in (5.23) were solved as a function of the system matrix parameters. The dc link voltage instability that occurred during testing of the microgrid system is particularly due to the impedance of the transformer coupled with the other line impedances. The microgrid system's

eigenvalues were obtained to show how the system responded to variations in the input impedance. Figure 5.9- 5.11 displays the variation in grid resistance, grid inductance and overall impedance respectively as the input impedance of the system increases. The system's eigenvalues were obtained to show the system stability to variations in the input impedance illustrated in Figure 5.12. It can be deduced that as the impedance increases, the eigenvalues of the system approach zero. This analysis verify that a weak-grid connection exists in the microgrid configuration.

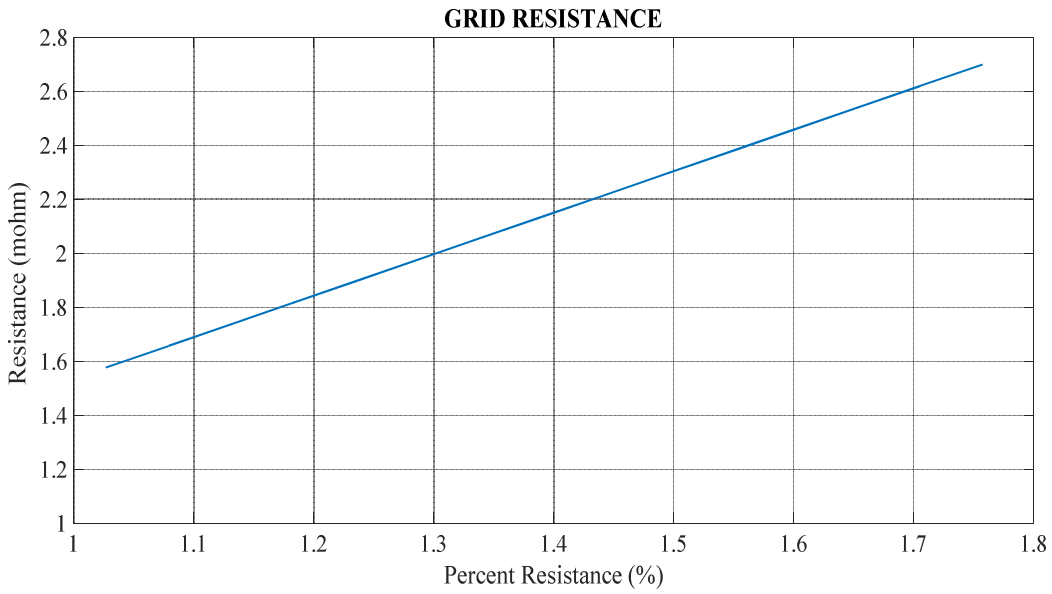

Figure 5.9 Grid Resistance vs Percent Resistance.

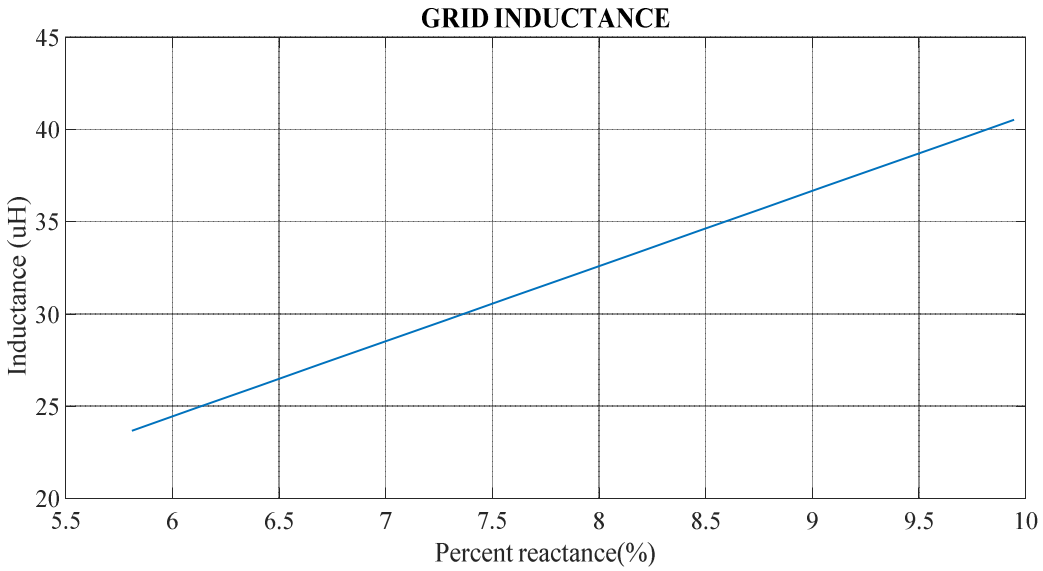

Figure 5.10 Grid Inductance vs Percent Inductance.

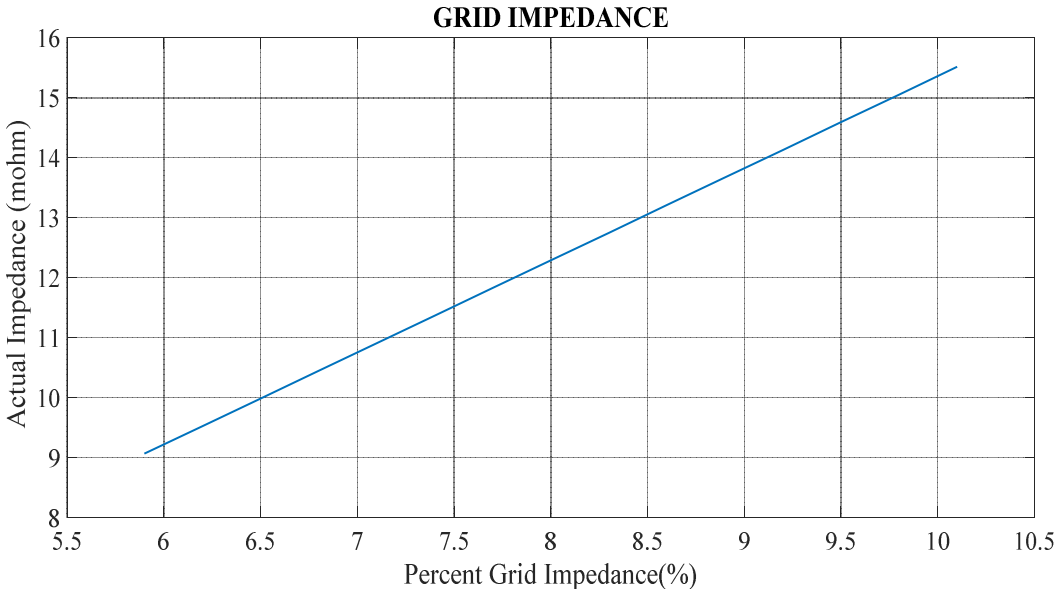

Figure 5.11 Grid Impedance vs Percent Impedance.

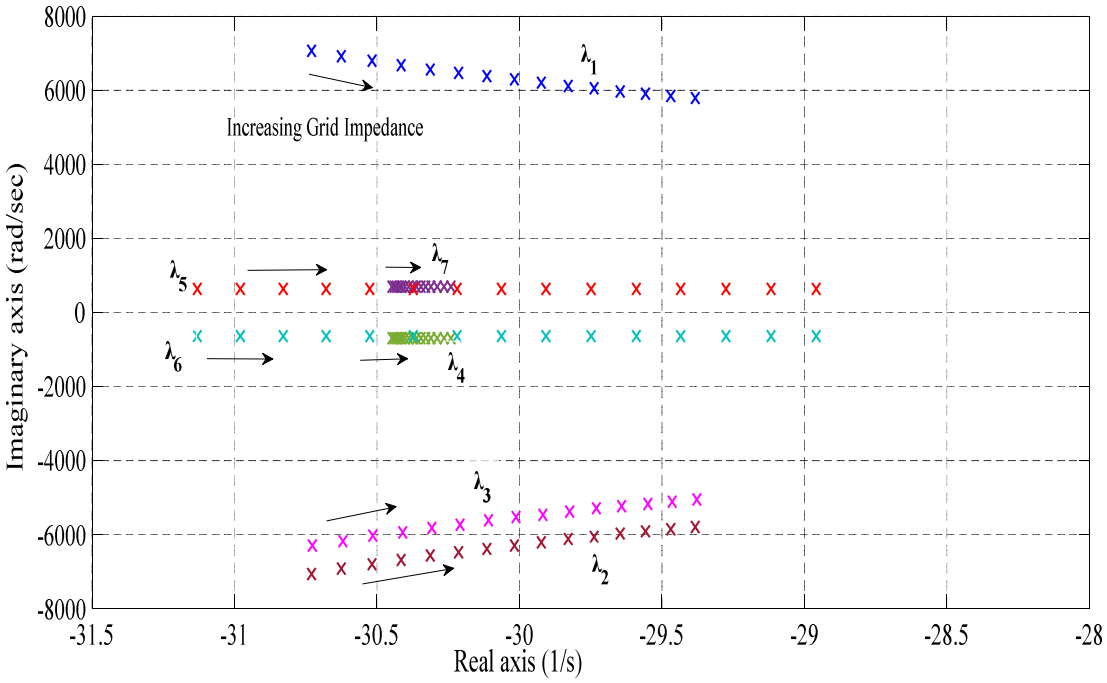

Figure 5.12 Eigenvalues of microgrid system with increasing grid impedance.

5.4.2 Application of Edge Theorem for weak grid analysis of NCREPT System

The weak grid analysis of the NCREPT microgrid configuration is analyzed using the edge theorem, which will be used to observe how varying the impedance values at the grid affects the overall grid stability. The edge theorem determines a system's stability based on the concept of parametric uncertainty [65-66]. It deals with the robust stability of polytopic family polynomials with respect to an arbitrary region. The Edge theorem typically shows the root space of the entire family of polynomials can be obtained from the root set of the exposed edges.

A polytopic family of polynomials can be observed as a convex hull of a finite number of polynomials which are mathematically expressed as the family

$$P(s) = \lambda_1 P_1(s) + \cdots + \lambda_n P_n(s) \qquad (5.24)$$

where $P_i(s)$ are fixed real polynomials and λ_i are real barycentric coordinates with $\lambda_i \geq 0$ and $\sum \lambda_i = 1$.

The edge theorem states that the stability of a polynomial with linear parameter dependency is determined by checking the edges of a l dimensional hyper-rectangle box called the "Q-box" which represents the vector space of defined parameters. Hence a polytope is robustly stable if and only if all of its edges are stable.

Theorem 5.3 (Edge Theorem): The polynomial family $P(s,Q) = \{\, p(s,q) = \sum_{i=0}^{n} a_i(q)s^i = |q \,\epsilon\, Q\}$ with affine coefficient functions $a_i(q)$ and $Q = \{q|q_i \epsilon |[q_i^-; q_i^+], i = 1,2, \ldots., l\}$ is stable iff the edges of the l dimensional Q-box are stable.

If the parameter values q_i take a minimum or maximum value then the corresponding polynomial is called the vertex polynomial. If exactly one of the polynomial parameters varies between maximum and minimum values while the remaining parameters stick to their maximum or minimal value then the polynomial is called an edge polynomial [67]. The number of edges of Q is given by

$$N_{edges} = l2^{l-1} \tag{5.25}$$

Hence by checking the stability of the edge of the Q box, the microgrid system's stability can be determined. And this done by checking the root location of the line segments of polynomials of the form

$$P_\lambda = (1-\lambda)P_1(s) + \lambda P_2(s), \qquad \lambda \,\epsilon [0\,,1] \tag{5.26}$$

In the case of the microgrid configuration, the transformer impedances are varied for the interval feedback systems of the VVVF drive and REGEN bench. The controller for the NCREPT microgrid configuration consists of a decoupled proportional integral controller for the grid-forming and grid-feeding converters. Hence it is suitable to implement proportional integral

feedback controllers for each rectifier and inverter for the VVVF drive and REGEN bench system matrices to form a single input single output (SISO) closed-loop system which will be used for implementing the edge theorem.

The isolated transfer functions represent the SISO for the output variables of interest in (5.22) which will be used in determining the new characteristic polynomial given as

$$\delta(s,P) = \delta_0(P) + \delta_1(P)S + \delta_2(P)S^2 + \cdots + \delta_{24}(P)s^{25} \tag{5.27}$$

An interval feedback closed-loop system for the VVVF drive is used to determine its robust stability since the impedance variations are associated with the input of this converter. The resistance and inductance parameter intervals are chosen as

$$R_T = [1.58m\Omega \;\; 2.7m\Omega] \quad \text{and} \quad L_T = [23.67\,\mu H \;\; 41\mu H] \tag{5.28}$$

which represents the coefficients of the interval polynomials of the VVVF drive. The two variable coefficients are used to construct the edges of the Q-box polytope producing four edge polynomials corresponding to four edges in the coefficient space shown in Figure 5.13.

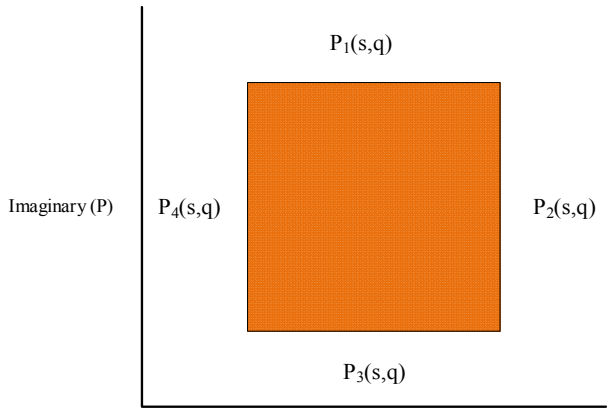

Figure 5.13 Coefficient Space

Using the Edge Theorem, the boundary of the root space of the interval polynomial family is obtained by plotting the root loci along the exposed edges of the box. The characteristic polynomials for the VVVF drive and REGEN bench plants with a closed-loop proportional integral controller were obtained and a root loci for each closed -loop system was constructed to observe its stability using the edge theorem.

Firstly, four edge polynomials for the transfer function of the VVVF dc link to input grid impedance of the interval feedback system were derived and the boundary of the root space of the interval polynomial family was obtained by plotting the root loci along the exposed edges of the Q-box. The root loci of the edges are illustrated in Figure 5.14. It can be observed that the entire root space of the set of characteristic polynomials is not found in the left-hand plane, therefore, the family of polynomials for the VVVF drive is not robustly stable.

Next, four vertex characteristic polynomials for the VVVF drive and REGEN bench were derived, and the edge theorem was applied to illustrate the overall system stability. The root space of NCREPT microgrid system is shown in Figure 5.15 and it can also be observed that the entire root space of the set of characteristic polynomials of the NCREPT system is not found in the left-hand plane, therefore, the family of polynomials for this system is not robustly stable.

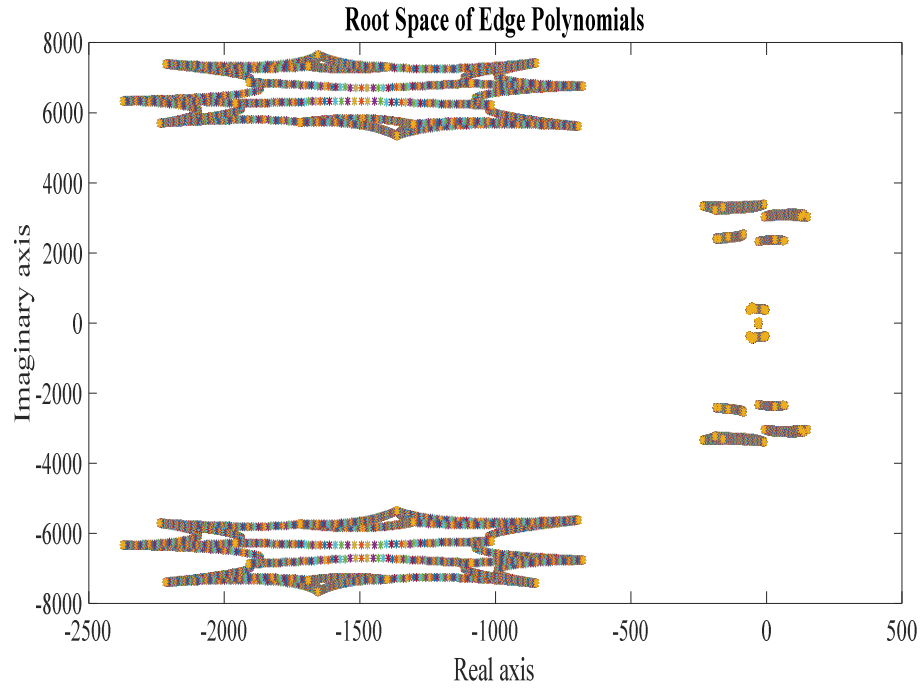

Figure 5.14 Root Space of the entire polytope of the VVVF drive.

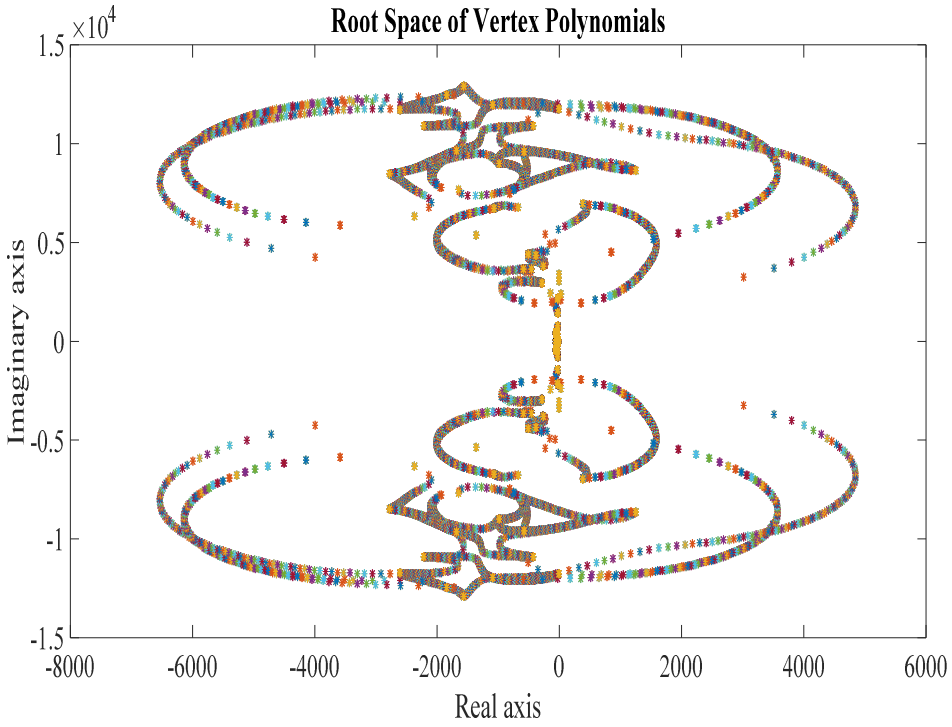

Figure 5.15 Root Space of NCREPT system

The robust stability analysis of the microgrid system using parametric uncertainty via the edge theorem indicates that the system is not robustly stable with a proportional integral controller. Additionally, as the input impedance increases the 13.8kV microgrid system becomes unstable. Thus, a robust control method such as a passivity-based control can be utilized to provide stability to the overall system. This notion leads to the development of theorem 5.4 for stabilizing hybrid ac/ac microgrid systems.

Theorem 5.4**: **VSC-based hybrid ac/dc microgrid systems can be stabilized by the passivity-based control method.

Proof: The weak grid stability analysis using the edge theorem and eigenvalue analysis for the linearized NCREPT microgrid system is valid for all members of the class of microgrids. From the stability analysis, the system is not robustly stable with a traditional proportional integral feedback. Therefore, from theorem 5.1 and theorem 5.2 VSC-based microgrids can be stabilized according to the passivity-based control method described in chapter three.

5.5 Summary

This chapter briefly discussed the various types of microgrids and derived stability theorems for the linearized microgrid configuration of the NCREPT system based on the concepts of Dirac structures, passivity, and the edge theorem for robust analysis. A stability analysis of the NCREPT system implemented the eigenvalue analysis to observe the poles of the system as the input impedance varies resulting. The system poles increased towards the right-hand plane indicating that the system was becoming increasingly unstable as the input impedance increased. The edge theorem was also implemented to verify the system's robustness by varying the input impedance of the NCREPT system and plotting the root space of the system. It was determined that the system was not robustly stable.

CHAPTER SIX

ENERGY-BASED MODELING AND CONTROL OF DC-AC VOLTAGE SOURCE INVERTER

6.1 Literature Review

In AC microgrids, dispatchable and non-dispatchable distributed generation units are integrated with voltage source inverters (VSI) to provide power to various loads and to the AC grid at the point of coupling (PCC). As discussed in chapters one and three, the voltage source inverter operates in two modes of operation at the primary level of the three-level hierarchy control. The grid-forming mode ensures voltage and frequency stability at the PCC during autonomous (island) mode. The grid-feeding mode regulates the active and reactive power injected into the grid. The microgrid can also provide power to the utility grid via back-to-back voltage source converter, which provides regenerative functionality.

The voltage control techniques that have been researched for the three-phase inverter includes an observer-based optimal voltage control for three-phase uninterruptible-power supply systems (UPS) [68], Model Predictive Control [69] for UPS, Feedback Linearization for UPS [70] Efficient-Implicit Model-Predictive Control [71], Optimal Fuzzy Logic Control [72], and Modified Interconnection and Damping Assignment Passivity-Based Control in standalone mode [73]. The aforementioned techniques have not been implemented in an AC microgrid systems for voltage and frequency regulation but as standalone systems.

For grid-feeding mode the power converter injects current into the grid; therefore, it is essential to employ a controller that ensures a zero steady-state error while regulating the active and reactive power with the grid. The existing current control techniques for voltage source inverters include the decoupled Proportional Integral control, Deadbeat control and Proportional Resonant current control for distributed power generation systems [74],[54]. These linear controllers are only

accurate up to a certain bandwidth after which their effectiveness become degraded. This chapter proposes the application of the Modified Interconnection and Damping Passivity-Based Control (Modified IDA-PBC) for the voltage source inverter in grid-forming mode. Currently, the 13.8kV system utilizes the decoupled proportional integral controller to modulate the REGEN Bench inverter as a load simulator which recirculates the injected current specified by a user input.

6.2 Mathematical modelling of Grid-Forming Inverter

Figure 6.1 displays the dc-ac inverter in grid-forming mode. Assuming a balanced three-phase system, the filter inductance is $L_f = L_a = L_b = L_c$ and the filter capacitance is $C_f = C_a = C_b = C_C$. The filter capacitor is transformed from a delta connected to a wye connected enabling a simpler mathematical model derivation. The dc current and phase currents flowing out of the inverter are represented by i_{dc}, i_a, i_b and i_c respectively. The three phase load currents are i_{la},i_{lb}, i_{lc}.The phase voltages of the inverter output arev_a, v_b, v_c and the capacitor voltages are v_{la}, v_{lb} and v_{lc}. The self-commutated IGBTs with anti-parallel diodes are labelled $S_1 - S_6$. The switches are complementary so when S_1 , S_2, and S_3 are on S_4 , S_5 and S_6 are turned off. The mathematical model of the three phase inverter is given in equation 6.1 [75-77].

To derive the controller for the three-phase inverter, the mathematical equations are transformed to the d-q synchronous rotating frame shown in (6.2) where v_{ld}, v_{lq} are the direct axis and quadrature axis load voltages respectively and i_{ld}, i_{lq} are the direct axis and quadrature axis load currents respectively and ω is the angular frequency for which the reference frame is rotating. Afterwards, the system is represented using the Port-Controlled Hamiltonian Model in order to design a stability controller using the Modified IDA-PBC technique.

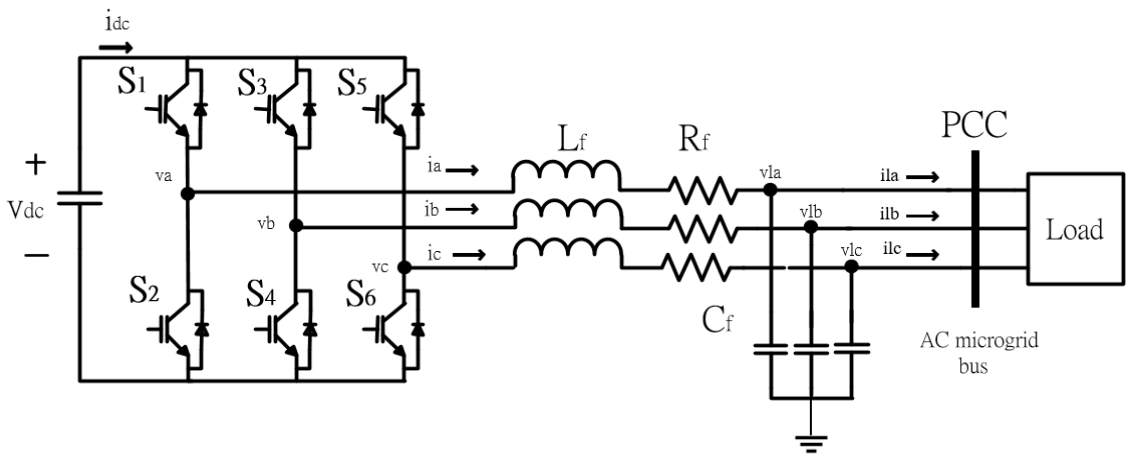

Figure 6.1 Three-phase Inverter in Grid-Forming Mode.

$$\begin{cases} \dfrac{L_f di_a}{dt} = -R_f i_a + v_{dc}(S_1 - \dfrac{1}{3}\sum_{k=1,2,3} S_k) - v_{la} = -R_f i_a + v_a - v_{la} \\ \dfrac{L_f di_b}{dt} = -R_f i_b + v_{dc}(S_2 - \dfrac{1}{3}\sum_{k=1,2,3} S_k) - v_{lb} = -R_f i_b + v_b - v_{lb} \\ \dfrac{L_f di_c}{dt} = -R_f i_c + v_{dc}(S_3 - \dfrac{1}{3}\sum_{k=1,2,3} S_k) - v_{lc} = -R_f i_c + v_c - v_{lc} \\ \dfrac{C_f dv_{la}}{dt} = i_a - i_{la} \quad \dfrac{C_f dv_{lb}}{dt} = i_b - i_{lb} \quad \dfrac{C_f dv_{lc}}{dt} = i_c - i_{lc} \end{cases} \tag{6.1}$$

In the d-q synchronous reference frame, the dynamical equations are described as,

$$\begin{cases} \dfrac{L_f di_d}{dt} = -R_f i_d + L\omega i_q + S_d v_{dc} - v_{ld} \\ \dfrac{L di_q}{dt} = -R_f i_q - L\omega i_d + S_q v_{dc} - v_{lq} \\ \dfrac{C_f dv_{ld}}{dt} = -i_{ld} + C\omega v_{ld} + i_d \\ \dfrac{C_f dv_{lq}}{dt} = -i_{lq} - C\omega v_{lq} + i_q \end{cases} \tag{6.2}$$

6.3 Port-Hamiltonian Modeling of the Grid-Forming Inverter

The Port-Hamiltonian Modelling system is shown in (6.3) and will be used to model the three-phase dc-ac inverter system in grid-forming mode.

$$\begin{cases} \dot{x} = [J(x,u) - R(x)] \dfrac{\partial H}{\partial x}(x) + g(x)u\,, \\ y = g^T(x) \dfrac{\partial H}{\partial x}(x). \end{cases} \tag{6.3}$$

Recalling in Chapter 3 that $x \epsilon \mathbb{R}^n$ is the state vector; the port power variables $u \epsilon \mathbb{R}^m$, $y \epsilon \mathbb{R}^m$system's are conjugated variables whose products has units of power dissipation is represented by $R(x) = R^T(x) \epsilon \mathbb{R}^{nxn} \geq 0$; The interconnection structure is captured in the skew-symmetric matrix is defined by $J(x,u) = -J^T(x,u) \epsilon \mathbb{R}^{nxn}$matrix and the input matrix $g(x) \epsilon \mathbb{R}^m$. Ortega et al. [40] suggests from (6.3) that for power converters the matrix $g(x,u)$ represents two kinds of interconnections structure, the standard $g(x)u$ and "the constant source inputs" where u is the switching of the source inputs. $H(x)$ represents the Hamiltonian function of the system.

In constructing the Port-Controlled Hamiltonian modeling equations for the three-phase inverter we define the state trajectories as

$$x = \begin{bmatrix} x_1 \\ x_2 \\ x_3 \\ x_4 \end{bmatrix} = \begin{bmatrix} Li_d \\ L_{iq} \\ Cv_{ld} \\ Cv_{lq} \end{bmatrix} = D \begin{bmatrix} i_d \\ i_q \\ v_{ld} \\ v_{lq} \end{bmatrix}, \tag{6.4}$$

where $D = diag\{L, L, C, C\}$ and i_d, i_q, v_{ld}, v_{lq} are the d-q voltages and currents.

The Hamiltonian energy function $H(x)$ is chosen to the total energy of the inductance and capacitance and is defined as

$$\begin{aligned} H(x) &= \frac{1}{2}x^T D^{-1}x \\ &= \frac{1}{2}x^T \begin{bmatrix} 1/L & 0 & 0 & 0 \\ 0 & 1/L & 0 & 0 \\ 0 & 0 & 1/C & 0 \\ 0 & 0 & 0 & 1/C \end{bmatrix} x \\ &= \frac{1}{2}Li_d^2 + \frac{1}{2}Li_q^2 + \frac{1}{2}Cv_{ld}^2 + \frac{1}{2}Cv_{lq}^2 \\ &= \frac{x_1^2}{2L} + \frac{x_2^2}{2L} + \frac{x_3^2}{2C} + \frac{x_4^2}{2C} \quad . \end{aligned} \tag{6.5}$$

6.4 Controller Design Procedure for Inverter in Grid-Forming Mode

The Modified Interconnection and Damping Assignment Passivity-Based Control is chosen as the control method because it allows for reference tracking and set point regulation thus producing a more robust controller design and transforms a non-passive system into a port-controlled Hamiltonian (passive) system. The three-phase DC-AC inverter will be designed for voltage and frequency regulation in grid-forming mode in the VVVF drive. Recalling from chapter 3, the objective of the modified IDA-PBC is to find a feedback controller $S = \beta(x, x^*)$ that stabilizes the system (6.3) to a desired trajectory error tracking such that the closed-loop dynamic is a Port-Controlled Hamiltonian with dissipation of the following form

$$\dot{e} = [J_d(e) - R_d(e)] \frac{\partial H_d}{\partial e}(x, x^*) , \tag{6.6}$$

where $e = x - x^*$ is the error variable, x is the state vector, x^* is the desired reference trajectory, $\dot{x^*}$ is the derivative of the reference trajectory, $J_d(e)$ is the closed-loop internal error interconnection matrix given by $J_d(e) = J(e) + J_a(e)$, the closed-loop error dissipation matrix is

defined as $R_d(e) = R(e) + R_a(e) = R_d^T(e)$ with $J_a(e)$ and $R_a(e)$ being the additional internal error interconnection and error damping matrices. $J_d(e)$ satisfy skew-symmetry such that $J_d(e) = -J_d^T(e)$ and $R_d(e)$ satisfy the positive semi-definiteness such that $R_d(e) = R_d^T(e)$ with $R_d(e) \geq 0$. The desired storage function $H_d(x, x_d)$: $R^n \Rightarrow$R such that it has minimum at $x = x^*$

$$\min H_d\,(x, x^*)\; at\; x = x^* \tag{6.7}$$

The desired closed-loop Hamiltonian function is defined by

$$\begin{aligned} H_d(x, x^*) &= H(x) + H_a(x, x^*) \\ &= \frac{1}{2}(x - x^*)^T D^{-1}(x - x^*) \\ &= \frac{1}{2} e^T D^{-1} e\,. \end{aligned} \tag{6.8}$$

with the desired trajectories given as,

$$x_d = \begin{bmatrix} x_1^* \\ x_2^* \\ x_3^* \\ x_4^* \end{bmatrix} = \begin{bmatrix} Li_d^* \\ Li_q^* \\ Cv_{ld} \\ Cv_{lq}^* \end{bmatrix}, \tag{6.9}$$

where $H_a(x, x^*)$ represents the energy modification error that is injected into the system by the controller and $H_d(x, x^*)$ has a minimum at the desired error point e. The control objectives are satisfied if there exists a controller $\mu(x, x^*)$, an added dissipation symmetric matrix $R_a(x, x^*)$, added interconnection skew matrix $J_a(x, x^*)$ and $H_a(x, x^*)$ can be found, which satisfies the partial differential tracking matching equation

$$[(J(x) - R(x)]\frac{\partial H_a}{\partial x}(x) + \left[J_a(x) - R_a(x)\right]\frac{\partial H_d}{\partial e}(x, x^*) + \gamma + \dot{x}^* = g\beta \tag{6.10}$$

A state-dependent disturbance γ can also be used as another degree of freedom in solving the partial differential matching equation and does not destroy the desired stability properties [42].The next step is to solve the matching equation in (6.10) by choosing the interconnection and damping assignment matrices and the desired storage function.

The three methods for solving the matching equation are the Non-Parameterized IDA-PBC, Parameterized IDA-PBC and Algebraic IDA-PBC discussed in chapter in three. The Parameterized method is chosen where the desired storage function $H_d(x, x^*)$ is fixed in (6.8) imposing constraints on the interconnection and damping matrices $J_d(x)$ and $R_d(x)$ respectively solving the matching condition in (6.10). Additionally, the interconnection and damping matrices $J_d(x)$ and $R_d(x)$ can be freely chosen provided that they satisfy the skew-symmetry and positive semi-definiteness respectively. The interconnection and damping matrices will be chosen such that the system trajectories are decoupled, and the system converges to the desired equilibrium point or set-point value that is desired. Also, it is imperative that the direct-axis and quadrature-axis components are decoupled so that any changes in the quadrature axis components do not cause issues with the direct axis components and vice versa. $J_d(x)$ will be designed to ensure decoupling of the direct and quadrature axis variables.

For the interconnection matrices,

$$J_d(x,u) = J(e,u) + J_a(e,u), \tag{6.11}$$

$$J(x) = \begin{bmatrix} 0 & -L\omega & 1 & 0 \\ L\omega & 0 & 0 & 1 \\ -1 & 0 & 0 & -C\omega \\ 0 & -1 & C\omega & 0 \end{bmatrix}, \quad J_a(e,u) = \begin{bmatrix} 0 & L\omega & -1 & 0 \\ -L\omega & 0 & 0 & -1 \\ 1 & 0 & 0 & C\omega \\ 0 & 1 & -C\omega & 0 \end{bmatrix}, \tag{6.12}$$

$$J_d(e,u) = \begin{bmatrix} 0 & -L\omega & 1 & 0 \\ L\omega & 0 & 0 & 1 \\ -1 & 0 & 0 & -C\omega \\ 0 & -1 & C\omega & 0 \end{bmatrix} \tag{6.13}$$

The damping matrices are chosen as,

$$R_d(x) = R(x) + R_a(e) \tag{6.14}$$

$$R(x) = \begin{bmatrix} R & 0 & 0 & 0 \\ 0 & R & 0 & 0 \\ 0 & 0 & 1/R_L & 0 \\ 0 & 0 & 0 & 1/R_L \end{bmatrix}, \qquad R_a(e) = \begin{bmatrix} R_1 & 0 & 0 & 0 \\ 0 & R_2 & 0 & 0 \\ 0 & 0 & R_3 & 0 \\ 0 & 0 & 0 & R_4 \end{bmatrix} \tag{6.15}$$

$$R_d(e) = \begin{bmatrix} R+R_1 & 0 & 0 & 0 \\ 0 & R+R_2 & 0 & 0 \\ 0 & 0 & R_3 & 0 \\ 0 & 0 & 0 & R_4 \end{bmatrix}$$

The input matrix is defined as

$$g(x,u) = \begin{bmatrix} v_d & 0 \\ 0 & v_q \\ 0 & 0 \end{bmatrix}, \tag{6.16}$$

As defined in [47], the desired Hamiltonian error function is given as

$$\begin{aligned} \frac{\partial H_d}{\partial e} &= \frac{\partial H_d(x,x^*)}{\partial x} = D^{-1}e\,, \\ \frac{\partial H_a}{\partial x}(x,x^*) &= \frac{\partial H_d(x,x^*)}{\partial x} - \frac{\partial H}{\partial x}(x) \\ &= D^{-1}(e-x) \\ &= -D^{-1}x^* \end{aligned} \tag{6.17}$$

The matching equation in (6.10) is written as

$$\begin{bmatrix} 0 & -L\omega & 1 & 0 \\ L\omega & 0 & 0 & 1 \\ -1 & 0 & 0 & -C\omega \\ 0 & -1 & C\omega & 0 \end{bmatrix} - \begin{bmatrix} R & 0 & 0 & 0 \\ 0 & R & 0 & 0 \\ 0 & 0 & 0 & 0 \\ 0 & 0 & 0 & 0 \end{bmatrix} \begin{bmatrix} -i_d^* \\ -i_q^* \\ -v_{ld}^* \\ -v_{lq}^* \end{bmatrix} + \begin{bmatrix} 0 & L\omega & -1 & 0 \\ -L\omega & 0 & 0 & -1 \\ 1 & 0 & 0 & C\omega \\ 0 & 1 & -C\omega & 0 \end{bmatrix} \tag{6.18}$$

$$- \begin{bmatrix} R_1 & 0 & 0 & 0 \\ 0 & R_2 & 0 & 0 \\ 0 & 0 & R_3 & 0 \\ 0 & 0 & 0 & R_4 \end{bmatrix} \begin{bmatrix} i_d - i_d^* \\ i_q - i_q^* \\ v_{ld} - v_{ld}^* \\ v_{lq} - v_{lq}^* \end{bmatrix} + \begin{bmatrix} 0 \\ 0 \\ -i_{ld} \\ -i_{lq} \end{bmatrix} + \begin{bmatrix} L\dot{i}_d^* \\ L\dot{i}_q^* \\ C\dot{v}_{ld}^* \\ C\dot{v}_{lq}^* \end{bmatrix} = \begin{bmatrix} S_d \\ S_q \\ 0 \\ 0 \end{bmatrix} \begin{bmatrix} V_{dc} & 0 \\ 0 & V_{dc} \\ 0 & 0 \\ 0 & 0 \end{bmatrix}$$

Solving the system in (6.18) the controllers and reference currents are defined as

$$S_d = \frac{\left[L\dot{i}_d^* + Ri_d^* - \omega L i_q - R_1(i_d - i_d^*) + v_{ld}^* \right]}{V_{dc}} \tag{6.19}$$

$$S_q = \frac{\left[L\dot{i}_q^* + Ri_q^* + \omega L i_d - R_2\left(i_d - i_q^*\right) + v_{lq}^* \right]}{V_{dc}} \tag{6.20}$$

$$i_d^* = C\dot{v}_d^* - R_3(v_{ld} - v_{ld}^*) - \omega C v_{lq} + i_{ld} \tag{6.21}$$

$$i_q^* = C\dot{v}_q^* - R_4\left(v_{lq} - v_{lq}^*\right) + \omega C v_{ld} + i_{lq} \tag{6.22}$$

As discussed in chapter three the damping values can freely choosen for R_1, R_2, R_3, R_4 if they satisfy a positive-definite matrix. This also applies to the damping parameters for the grid-feeding mode. The damping matrix allows the passivity-based controller to force the closed-loop dynamics to act as if there are virtual resistors connected in series or parallel to the real circuit elements.

6.5 Simulation Results

The inverter of the VVVF drive was simulated using the designed Modified IDA-PBC and the results were compared to a proportional integral controller. The inverter system parameters are given in Table 6.1 while the controller parameters of the Modified IDA-PBC and proportional integral controller are tabulated in Table 6.2.

Table 6.1 Inverter Simulation Parameters for VVVF DRIVE

Parameter	Symbol	Nominal Value
Input Voltage	V_{dc}	750Vdc
Filter Inductor	L_f	20 µH
Filter Capacitor	C_f	3 x 480µF
DC link capacitor	C_{dc}	42.3mF
EMI Filter Capacitor	C_{EMI}	40 µF
Switching Frequency	f_{sw}	8 kHz
Resistive Load	R_{load}	50 Ω

Table 6.2 Controller Parameters

Modified IDA-PBC		
Parameter	**Symbol**	**Value**
Inner current damping	R_1, R_2	1
Outer Voltage damping	R_3, R_4	0.1
Proportional Integral Control		
Parameter	**Symbol**	**Value**
Inner current Proportional gain	K_p_c	1.4325
Inner current Integral gain	K_i_c	0.0022
Outer voltage Proportional gain	K_p_v	5
Outer voltage Integral gain	K_i_v	0.125

The proportional integral controller (PI) design is based on the control diagram in Figure 4.5 that displays the control structure of a grid-forming converter utilizing a PI controller. The system was simulated using MATLAB/Simulink™ and the Simpower toolbox. The inverter is provided with an input voltage of 750Vdc and produces an output voltage of 480Vrms or a peak voltage of 678Vpeak. Figure 6.2 displays the inverter output voltage of the VVVF drive using the Modified IDA-PBC controller and PI control. Based on the simualtion results, it can be deduced both control methods are capable of providing good output voltage response for grid-forming converters.

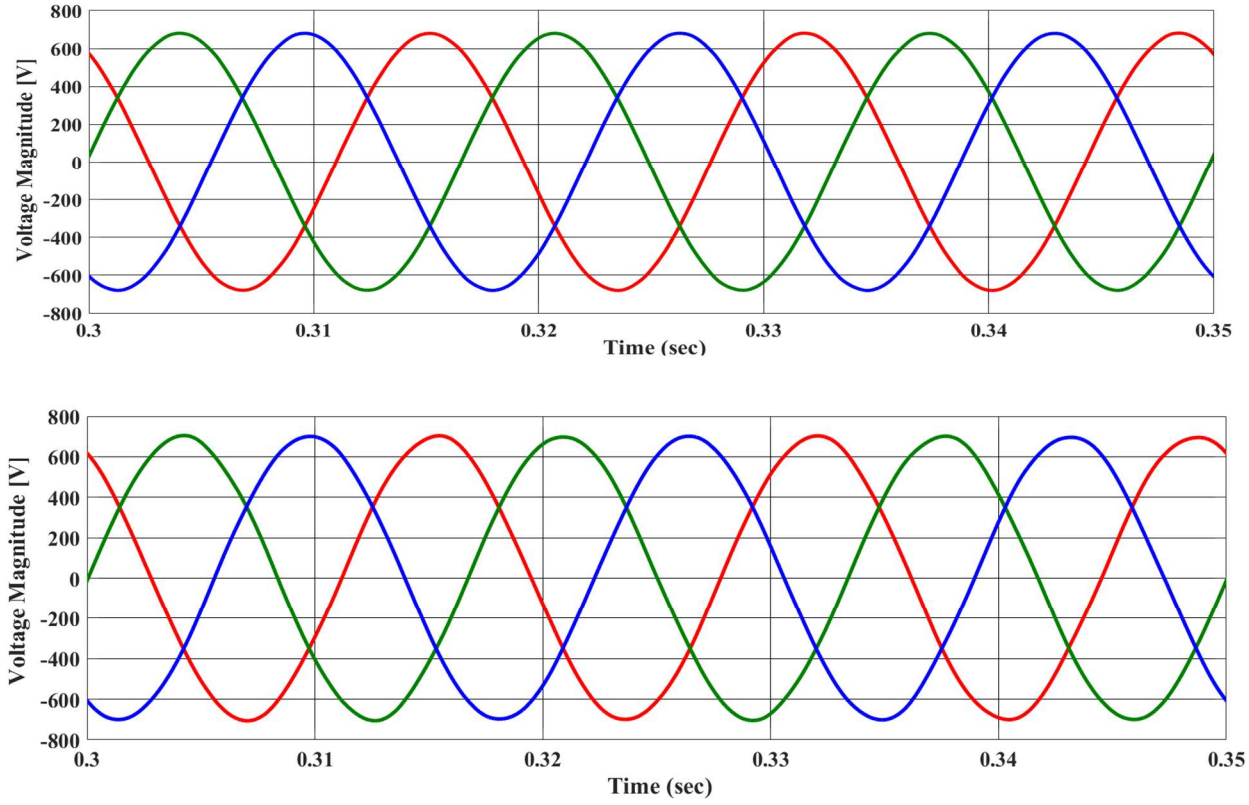

Figure 6.2 Inverter Output Voltage using Modified IDA-PBC (top) and Proportional Integral control (bottom)

6.6 Summary

This chapter derives a stability controller for the DC-AC inverter of the two-level back-to-back voltage source converter of the VVVF drive. The controller was designed by deriving the mathematical model of the inverter using the concept of grid-forming. The mathematical model is transformed into its d-q synchronous rotating frame equivalent and is converted to a port-Hamiltonian model. The Modified IDA-PBC controller is then designed using the port-Hamiltonian modeling formulation and the desired control objectives resulting in a closed-loop controller that provides a stable output voltage of 480Vrms at a frequency of 60Hz for the Variable Voltage Variable Frequency Drive.

CHAPTER SEVEN

ENERGY-BASED MODELING AND CONTROL OF THE ACTIVE FRONT-END RECTIFIER

7.1 Literature Review

There has been extensive research on the three-phase grid-connected rectifier in regards to new control methods and active and passive damping techniques for resonance mitigation. The grid-connected AFE rectifier typically consists of an LCL input filter to minimize the input current harmonics which is more cost-effective than an L filter[78][79]. One drawback of the LCL filter is the stability problem which appears due to the filter resonance effect [12][80][81]. To reduce the filter resonance, active and passive damping techniques are implemented. Active damping consists of using damping resistors in series with a filter capacitor, but this method creates additional losses. So active damping which involves modifying the control algorithm is preferred.

The existing AFE rectifier control techniques include voltage oriented PI current control [82], A passivity-based current control with outer loop PI compensation [83], an input-output feedback linearization method [84], and Generalized Closed-Loop Control Schemes with Embedded Virtual Impedances [12]. An Interconnection and Damping Assignment (IDA-PBC) passivity-based control is also used for L-based rectifiers, but neglects to include the damping injection thus the controller reduces to an Energy-Shaping and Damping Injection Passivity-Based Control [85]. Other methods that are used in controlling a grid-connected rectifier are Lyapunov-based control [26], An IDA-PBC method[86][87], Fuzzy Logic Control [88], Model Predictive Control [89], an integrated Sliding mode and Port-Hamiltonian Control [90] and an Interconnection and damping assignment control with generalized state-space average modelling [91].

Most of the aforementioned controllers are designed for L-based active rectifiers and don't provide an analysis into the resonance effect for LCL based rectifiers. Based on previous literature an IDA-PBC was designed for a single phase back-to-back converter system, but a generalized state-space averaging method was used for implementing the controller [52]. In [92] a bidirectional controller using the port-Hamiltonian and general state space averaging technique is implemented for a back-to-back converter. The VVVF drive and Regen bench utilizes the decoupled proportional integral current control method mentioned in chapter 3. The application of the Modified Interconnection and Damping Assignment Passivity-Based Control theory is presented to control the active front-end rectifier of the VVVF drive and Regen bench in the NCREPT microgrid system.

7.2 Mathematical modelling of Active Front-End Rectifier

The grid-connected active front-end rectifier is illustrated in Figure 7.1. Assuming a balanced three-phase system the filter inductance is $L_f = L_a = L_b = L_c$ and the filter capacitance is $C_f = C_a = C_b = C_C$ .The filter capacitor is transformed from a delta connected to a wye connected enabling a simpler mathematical model derivation. The dc current is represented by i_{dc} and the input line currents flowing in the rectifier are i_a, i_b and i_c. The output voltage across the load is measured as v_{dc}. The self-commutated IGBTs with anti-parallel diodes are labelled $S_1 - S_6$. The switches are complementary hence when S_1 , S_2, and S_3 are on S_4 , S_5 and S_6 are turned off. The mathematical model of the three-phase rectifier is given in equation 7.1[77].

The three-phase rectifier is also modeled in the d-q synchronous rotating frame given in equation (7.2) where v_d, v_d are the direct axis and quadrature axis voltage respectively and i_d, i_q are the direct axis and quadrature axis grid currents respectively and ω is the angular frequency for which the reference frame is rotating.

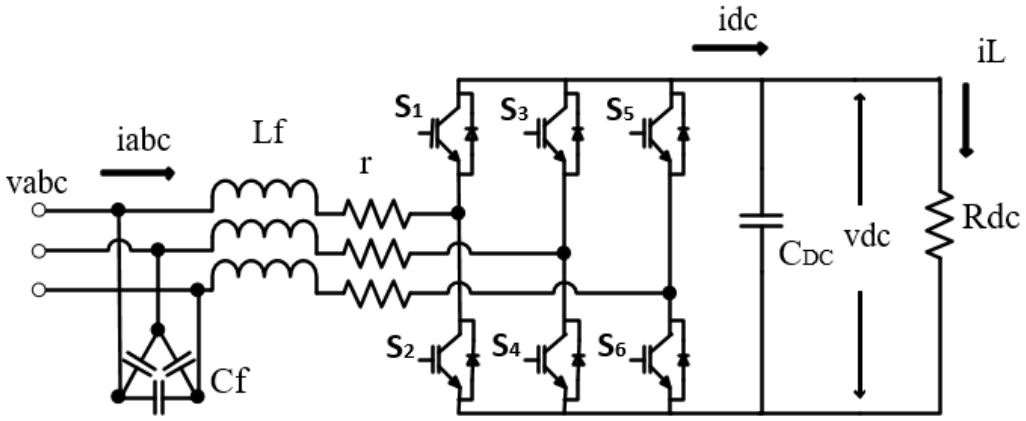

Figure 7.1. Active Front-End Rectifier.

The dynamical equations for the AFE rectifier in the stationary frame are given as,

$$\begin{cases} \frac{Ldi_a}{dt} = -Ri_a + v_{dc}(S_1 - \frac{1}{3}\sum_{k=a,b,c} S_k) + v_a \ = -Ri_a - S_a v_{dc} + v_a \\ \frac{Ldi_b}{dt} = -Ri_b + v_{dc}(S_2 - \frac{1}{3}\sum_{k=a,b,c} S_k) + v_b \ = -Ri_b - S_b v_{dc} + v_b \\ \frac{Ldi_c}{dt} = -Ri_{bc} + v_{dc}(S_3 - \frac{1}{3}\sum_{k=a,b,c} S_k) + v_c \ = -Ri_c - S_c v_{dc} + v_c \\ \frac{Cdv_{DC}}{dt} = i_{dc} - i_l = S_a i_a + S_b i_b + S_c i_c - i_{load} \end{cases} \tag{7.1}$$

In the d-q synchronous reference frame, the dynamical equations are described as,

$$\begin{cases} \frac{Ldi_d}{dt} = -Ri_d - S_d v_{dc} + v_d + \omega L i_q \\ \frac{Ldi_q}{dt} = -Ri_q - S_q v_{dc} + v_q - \omega L i_d \\ \frac{Cdv_{DC}}{dt} = S_d i_d + S_q i_q - i_{load} \end{cases} \tag{7.2}$$

7.3 Port-Hamiltonian Model of the Active Front End Rectifier

The Port-Hamiltonian Modelling system is shown in (6.3) and will be used to model the three-phase active front-end rectifier system.

$$\begin{cases} \dot{x} = [J(x,u) - R(x)] \dfrac{\partial H}{\partial x}(x) + g(x,u), \\ y = g^T(x) \dfrac{\partial H}{\partial x}(x). \end{cases} \tag{7.3}$$

Recalling in Chapter six that $x \epsilon \mathbb{R}^n$ is the state vector; the port-power variables $u \, \epsilon \, \mathbb{R}^m$, $y \, \epsilon \, \mathbb{R}^m$ of the system are conjugated variables whose products has units of power. The dissipation matrix is represented by $R(x) = R^T(x) \, \epsilon \, \mathbb{R}^{nxn} \geq 0$; The interconnection structure is captured in the skew-symmetric matrix $J(x,u) = -J^T(x,u) \, \epsilon \, \mathbb{R}^{nxn}$ and the input matrix $g(x,u) \, \epsilon \, \mathbb{R}^m$. According to [40], for power converters the matrix $g(x,u)$ represents two kinds of interconnections structure, the standard $g(x)u$ and "the constant source inputs" where u is the switching of the source inputs. The Hamiltonian function $H(x)$ represents the total energy of the system.

In constructing the Port-Controlled Hamiltonian modeling equations for the three-phase AFE rectifier the state trajectories are defined as

$$x = \begin{bmatrix} x_1 \\ x_2 \\ x_3 \end{bmatrix} = \begin{bmatrix} Li_d \\ L_{iq} \\ Cv_{dc} \end{bmatrix} = D \begin{bmatrix} i_d \\ i_q \\ v_{dc} \end{bmatrix}, \tag{7.4}$$

where $D = diag\{L, L, C\}$ and i_d, i_q, v_{dc} are the d-q currents and dc output voltage respectively.

The Hamiltonian energy function $H(x)$ is defined as

$$\begin{aligned} H(x) &= \frac{1}{2}x^T D^{-1}x \\ &= \frac{1}{2}x^T \begin{bmatrix} 1/L & 0 & 0 \\ 0 & 1/L & 0 \\ 0 & 0 & 1/C \end{bmatrix} x \\ &= \frac{1}{2}Li_d^2 + \frac{1}{2}Li_q^2 + \frac{1}{2}Cv_{dc}^2 \\ &= \frac{x_1^2}{2L} + \frac{x_2^2}{2L} + \frac{x_3^2}{2C}. \end{aligned} \tag{7.5}$$

7.4 Modified IDA-PBC Controller Design

The Modified IDA-PBC is designed to ensure dc bus voltage control for the AFE rectifier. It is important to note that the operation of the three-phase rectifier involves tracking control objectives, which cannot be achieved with the traditional IDA-PBC method. Recalling from chapter six, the objective of the modified IDA-PBC is to find a feedback controller $u = \beta(x, x^*)$ that stabilizes the system (7.3) to a desired trajectory error tracking such that the closed-loop dynamic is a Port-Controlled Hamiltonian with dissipation of the following form [47],[73]

$$\dot{e} = [J_d(e) - R_d(e)] \frac{\partial H_d}{\partial e}(x, x^*), \tag{7.6}$$

where $e = x - x^*$ is the error variable, x is the state vector, x^* is the desired reference trajectory, $\dot{x^*}$ the derivative of the reference trajectory, $J_d(e)$ is the closed-loop internal error interconnection matrix given by $J_d(e) = J(e) + J_a(e)$, the closed-loop error dissipation matrix is defined as $R_d(e) = R(e) + R_a(e) = R_d^T(e)$ with $J_a(e)$ and $R_a(e)$ being the added internal error interconnection and error damping matrices. $J_d(e)$ satisfy skew-symmetry such that $J_d(e) = -J_d^T(e)$ and $R_d(e)$ satisfy the positive semi-definiteness such that $R_d(e) = R_d^T(e)$ with $R_d(e) \geq 0$. The desired storage function $H_d(x, x^*)$: $R^n \Rightarrow$R such that it has minimum at $x = x^*$

$$\min H_d\,(x, x^*)\; at\; x = x^* \tag{7.7}$$

The desired closed-loop error Hamiltonian function is defined by

$$\begin{aligned} H_d(x, x^*) &= H(x) + H_a(x, x^*) \\ &= \frac{1}{2}(x - x^*)^T D^{-1}(x - x^*) \\ &= \frac{1}{2} e^T D^{-1} e\,. \end{aligned} \tag{7.8}$$

The reference vectors are defined by

$$x^* = \begin{bmatrix} x_1^* \\ x_2^* \\ x_3^* \end{bmatrix} = \begin{bmatrix} Li_d^* \\ Li_q^* \\ Cv_{dc}^* \end{bmatrix}, \tag{7.9}$$

and $H_a(x, x^*)$ represents the energy modification error that is injected into the system by the controller and $H_d(x, x^*)$ has a minimum at the desired error operating point e. The control objectives are satisfied if there exists a controller $\mu(x, x^*)$, an added dissipation symmetric matrix $R_a(x, x^*)$, added interconnection skew matrix $J_a(x, x^*)$ and $H_a(x, x^*)$ can be found, which satisfies the partial differential tracking matching equation

$$[J(x) - R(x)]\frac{\partial H_a}{\partial x}(x) + \left[J_a(x) - R_a(x)\right]\frac{\partial H_d}{\partial e}(x, x^*) + \gamma + \dot{x^*} = g\beta \tag{7.10}$$

where the external disturbances is represented by γ represents. The next step is to solve the matching equation in (7.10) by choosing the interconnection and damping assignment matrices and the desired storage function. The Parameterized method is chosen where we completely fix the desired storage function H_d imposing constraints on the interconnection and damping matrices $J_d(x)$ and $R_d(x)$ respectively solving the matching condition (7.10). Additionally, the interconnection and damping matrices $J_d(x)$ and $R_d(x)$ can be freely chosen provided that they satisfy the skew-symmetry and positive semi-definiteness respectively. The interconnection and

damping matrices will be chosen such that the system converges to the desired equilibrium point or set-point value that is desired. Also, it is imperative that the direct-axis and quadrature-axis components are decoupled so that any changes in the quadrature axis components do not cause issues with the direct axis components. $J_d(x)$ will be designed to ensure decoupling.

For the interconnection matrices,

$$J_d(e,u) = J(e,u) + J_a(e,u), \tag{7.11}$$

$$J(x,u) = \begin{bmatrix} 0 & -\omega L & -S_d \\ \omega L & 0 & -S_q \\ S_d & S_q & 0 \end{bmatrix}, \quad J_a(e,u) = \begin{bmatrix} 0 & \omega L & S_d \\ -\omega L & 0 & S_q \\ -S_d & -S_q & 0 \end{bmatrix}, \tag{7.12}$$

$$J_d(e,u) = \begin{bmatrix} 0 & 0 & 0 \\ 0 & 0 & 0 \\ 0 & 0 & 0 \end{bmatrix}.$$

The desired damping matrix is defined as

$$R_d(e) = R(x) + R_a(e), \tag{7.13}$$

$$R(x) = \begin{bmatrix} R & 0 & 0 \\ 0 & R & 0 \\ 0 & 0 & 1/R_{dc} \end{bmatrix}, \qquad R_a(e) = \begin{bmatrix} R_1 & 0 & 0 \\ 0 & R_2 & 0 \\ 0 & 0 & R_3 \end{bmatrix}, \tag{7.14}$$

$$R_d(e) = \begin{bmatrix} R + R_1 & 0 & 0 \\ 0 & R + R_2 & 0 \\ 0 & 0 & R_3 + 1/R_{dc} \end{bmatrix}.$$

The input matrix is defined as

$$g(x,u) = \begin{bmatrix} v_d & 0 \\ 0 & v_q \\ 0 & 0 \end{bmatrix}, \tag{7.15}$$

As defined in equation in [47], the desired Hamiltonian error function is given as

$$\frac{\partial H_d}{\partial e} = \frac{\partial H_d(x, x^*)}{\partial x} = D^{-1}e\,,$$

$$\begin{aligned}\frac{\partial H_a}{\partial x}(x, x^*) &= \frac{\partial H_d(x, x^*)}{\partial x} - \frac{\partial H}{\partial x}(x) \\ &= D^{-1}(e - x) \\ &= -D^{-1}x^*\end{aligned} \tag{7.16}$$

7.4.1 Control Objectives

The control objectives of the AFE rectifier are as follows:

The output dc voltage should be equal to a desired constant value V_{dc} which must be greater than the utility ac voltage plus the voltage drop across the ac inductor. The minmum dc capacitor voltage is defined as

$$V_{dc} > \sqrt{3\left(V_d + \omega L i_q\right)^2 + \left(\omega L i_d\right)^2} \tag{7.17}$$

where V_d is the d-axis grid voltage in the dq reference frame and i_d is the d-axis current. Hence, the output dc voltage error $(v_{dc} - V_{dc}^*) \rightarrow 0$ and tracks a given a reference voltage V_{dc}^*.

- The power factor should be unity at the grid side which means that the reactive power of the converter is 0.

At steady state, $x_1 \rightarrow x_1^* = i_d^*, x_2 \rightarrow x_2^* = 0$ and $x_3 \rightarrow x_3^* = CV_{dc}^*$ which leads to the desired equilibrium points given as,

$$x_d = \begin{bmatrix} x_{1d} \\ x_{2d} \\ x_{3d} \end{bmatrix} = \begin{bmatrix} Li_d^* \\ 0 \\ CV_{dc}^* \end{bmatrix}\,, \tag{7.18}$$

Recalling the matching equation in 7.10 is written as

$$[(J(x)-R(x)]\frac{\partial H_a}{\partial x}(x)+\left[J_a(x)-R_a(x)\right]\frac{\partial H_d}{\partial e}(x,x^*)+\dot{x_d^*}=g\beta. \tag{7.19}$$

The matching equation can be rewritten as,

$$\begin{bmatrix}0 & -\omega L & -S_d\\ \omega L & 0 & -S_q\\ S_d & S_q & 0\end{bmatrix}-\begin{bmatrix}R & 0 & 0\\ 0 & R & 0\\ 0 & 0 & 1/R_{dc}\end{bmatrix}\begin{bmatrix}-i_d^*\\ -i_q^*\\ -v_{dc}^*\end{bmatrix}+\begin{bmatrix}0 & \omega L & S_d\\ -\omega L & 0 & S_q\\ -S_d & -S_q & 0\end{bmatrix} \tag{7.20}$$

$$-\begin{bmatrix}R_1 & 0 & 0\\ 0 & R_2 & 0\\ 0 & 0 & R_3\end{bmatrix}\begin{bmatrix}i_d-i_d^*\\ i_q-i_q^*\\ v_{dc}-v_{dc}^*\end{bmatrix}+\begin{bmatrix}L\dot{i}_d^*\\ L\dot{i}_q^*\\ C\dot{v}_{dc}^*\end{bmatrix}=\begin{bmatrix}v_d & 0\\ 0 & v_q\\ 0 & 0\end{bmatrix}$$

Solving the system in (7.20) the controllers are defined as

$$S_d=\frac{\left[R_1(i_d-i_d^*)-\omega Li_q-Ri_d^*-L\dot{i}_d^*+v_d\right]}{V_{dc}} \tag{7.21}$$

$$S_q=\frac{\left[R_2(i_d-i_q^*)+\omega Li_d-Ri_q^*-L\dot{i}_q^*+v_q\right]}{V_{dc}} \tag{7.22}$$

$$-S_di_d-S_qi_q-R_3(v_{dc}-v_{dc}^*)+\frac{v_{dc}^*}{R_{dc}}+C\dot{v}_{dc}^*=0 \tag{7.23}$$

Substituting (7.21) and (7.22) into (7.23) and considering at steady state $i_d=i_d^*$ and $i_q=i_q^*$, the desired active current is obtained as

$$i_d^*=\frac{\frac{v_d}{R}\pm\sqrt{(\frac{v_d}{R})^2-4(\frac{v_{dc}*V_{dc}^*}{R_{dc}R}+{i_q^*}^2-\frac{v_{dc}}{R}R_3(v_{dc}-V_{dc}^*)]}}{2} \tag{7.24}$$

As mentioned in chapter six the damping parameters are chosen freely for the damping matrix R_d which contains R_1,R_2 and R_3

7.4.1.1 Integral Action

The derived controllers in (7.21) and (7.22) are dependent on the system parameters which may lead to a steady-state error in the state variables due to parameter variation. To mitigate this issue the integral action discussed in chapter three is added to the proposed controller. This integral action extension will be useful in stabilizing the dc link of the VVVF and REGEN drives when they are interconnected.

Recalling from (7.3), the pH model of the system is described by

$$\dot{x} = [J(x,u) - R(x)]\frac{\partial H}{\partial x}(x) + g(x,u), \qquad (7.25)$$
$$y = g^T(x)\frac{\partial H}{\partial x}(x).$$

Then a new PCH model of the integral controller is given as

$$\dot{v} = u_{ic} \qquad (7.26)$$

$$y_{ic} = g^T(\rho)\frac{\partial H_{ic}}{\partial v}(\rho) = \frac{\partial H_{ic}}{\partial v}(\rho) \qquad (7.27)$$

where v is the state variable, u_{ic} is the input vector, y_{ic} is the output vector and $H_{ic} = 1/2\rho^T\rho$ is the energy function of the integral controller. The closed-loop system when interconnected with the feedback controller is given as

$$u_{ic} = \dot{\rho} = y = g^T(x)\frac{\partial H_d(x,x^*)}{\partial e} \qquad (7.28)$$

And the energy function of the closed-loop system with the integral controller is written as,

$$H_T(x,x^*,v) = H_d(x,x^*) + H_{ia}(\rho), \qquad (7.29)$$

The closed-loop system with integral controller is a PCH with the form

$$\begin{bmatrix}\dot{x}\\ \dot{\rho}\end{bmatrix} = \begin{bmatrix}J_d(e) - R_d(e) & g(x)K_I\\ -K_I g^T(x) & 0\end{bmatrix}\begin{bmatrix}\dfrac{\partial H_T(x,x^*,\rho)}{\partial e}\\ \dfrac{\partial H_T(x,x^*,\rho)}{\partial v}\end{bmatrix} + \begin{bmatrix}\dot{x}^*\\ 0\end{bmatrix}.$$

(7.30)

Solving 7.30, the new controller is obtained as

$$\begin{bmatrix} S_{dnew} \\ S_{qnew} \end{bmatrix} = \begin{bmatrix} S_d \\ S_q \end{bmatrix} + \rho \quad = \begin{bmatrix} S_d \\ S_q \end{bmatrix} - \mathrm{K_I} \int g^T \frac{\partial H_d(x, x^*)}{\partial e} dt \tag{7.31}$$

After substitution, the final PCH controller is given as

$$\begin{aligned} S_{dnew} &= \frac{\left[R_1(i_d - i_d^*) - \omega L i_q - R i_d^* - L\dot{i}_d^* + v_d\right]}{V_{dc}} + \rho_d \\ S_{qnew} &= \frac{\left[R_2\left(i_d - i_q^*\right) + \omega L i_d - R i_q^* - L\dot{i}_q^* + v_q\right]}{V_{dc}} + \rho_q \end{aligned} \tag{7.32}$$

where the added integral controllers are written as,

$$\rho_d = -\mathrm{K_I} \int v_d(i_d - i_d^*) dt, \tag{7.33}$$

$$\rho_q = -\mathrm{K_I} \int v_q\left(i_q - i_q^*\right) dt, \tag{7.34}$$

The selection of $\mathrm{K_I}$ in the above equations is determined by the static error of the system states.

7.5 Simulation Parameters

The active-front end rectifier of the VVVF drive and REGEN bench was simulated using the designed Modified IDA-PBC and the results were compared to a proportional integral controller. The rectifier system parameters of the VVVF drive are given in Table 7.1 while the controller parameters are displayed in Table 7.2. The proportional integral controller design is based on the control diagram in Figure 4.2 which displays the AFE rectifier control structure of a Proportional Integral controller. The system was simulated using MATLAB/Simulink™ and the Simpower toolbox. In Figure 7.1, The rectifier is provided with 480Vrms and produces an output voltage of

750Vdc. Figure 7.2 displays the rectifier voltage of the VVVF drive using the Modified IDA-PBC controller while Figure 7.3 displays the output rectifier voltage using a PI control. Based on the simualtion results, the PI controller allows the dc voltage to reach steady-state at 0.03 seconds, but the controller design results in an overshoot of the voltage to 810V which would cause a voltage collapse in the microgrid system.

The modified IDA-PBC allows the rectifier's dc link voltage to reach steady-state in 0.04 seconds with and overshoot that increases to 756V. The modified IDA-PBC provides for better voltage regulation.

Table 7.1 AFE Rectifier Parameters for VVVF drive

Parameter	**Symbol**	**Nominal Value**
Input Voltage	V_{ac}	480Vrms
Filter Inductor	L_f	110 µH
Filter Capacitor	C_f	3 x 384µF
DC link capacitor	C_{dc}	46.2mF
Switching Frequency	f_{sw}	8 kHz
Resistive Load	R_{load}	50 Ω

Table 7.2 Controller Parameters for VVVF drive AFE rectifier

Modified IDA-PBC		
Parameter	**Symbol**	**Value**
Inner Current Damping	R_1 R_2	8
Outer Voltage damping	R_3	25
Integral voltage extension	K_{Iv}	5
Proportional Integral Control		
Parameter	**Symbol**	**Value**
Inner current Proportional gain	K_p_c	2.8717
Inner current Integral gain	K_i_c	0.0090
Outer voltage Proportional gain	K_p_v	20.8947
Outer voltage Integral gain	K_i_v	1.3799

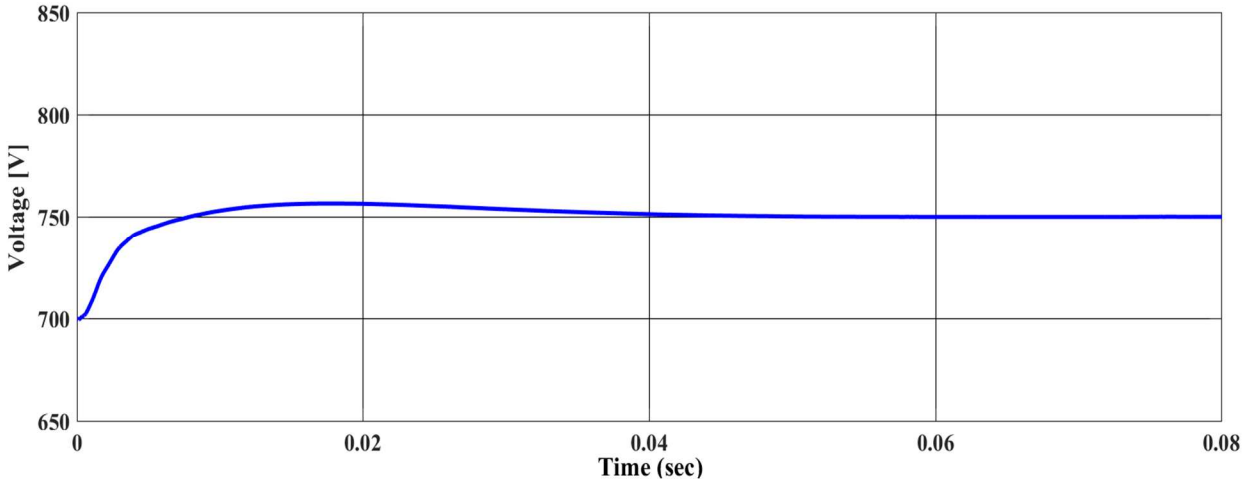

Figure 7.2 Rectifier Output Voltage for VVVF drive using Modified IDA-PBC

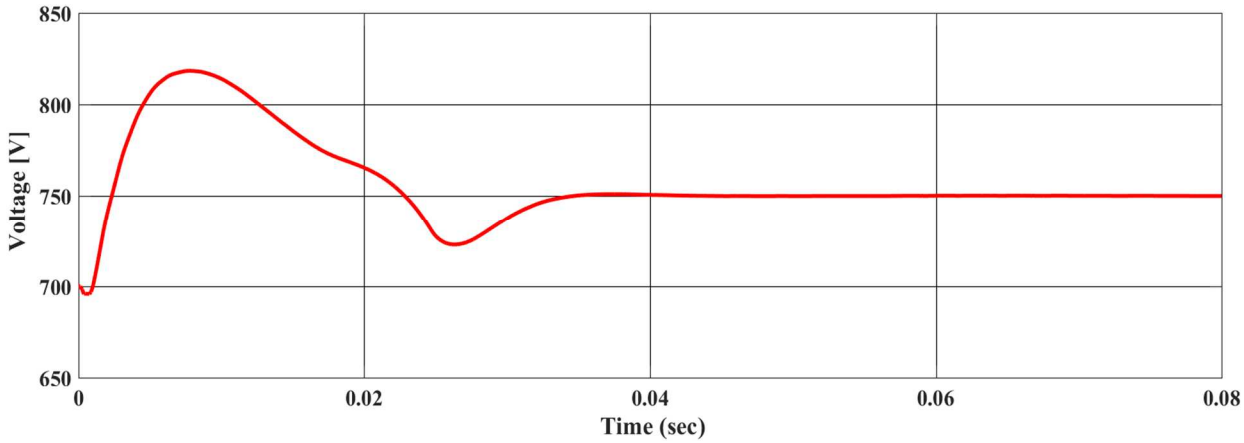

Figure 7.3 Rectifier Output Voltage for VVVF drive using Proportional Integral control.

The active front-end rectifier for the REGEN was simulated with the Modified IDA-PBC and PI controller to observe the output voltage response. The AFE rectifier system and control parameters for the REGEN bench and are given in Tables 7.3 and 7.4 respectively. Figure 7.4 displays the rectifier output voltage with the Modified –IDA-PBC. The output voltage response reaches steady-state at 0.05 seconds with an overshooting of 5 volts. This response was compared to Figure 7.4 which displays the rectifier voltage using a PI controller. The PI controller allow the system in Figure 7.4 to reach a steady-state of 0.03 second, but the system is very oscillatory and the voltage increases above 800V which is above the REGEN's allowable limit. Therefore, it can deduced that the Modified IDA-PBC successfully stabilizes the dc bus voltage with minimal oscillation.

Table 7.3 AFE Rectifier Parameters for REGEN bench

Parameter	**Symbol**	**Nominal Value**
Input Voltage	V_{ac}	480Vrms
Filter Inductor	L_f	20μH
Filter Capacitor	C_f	3 x 480μF
DC link capacitor	C_{dc}	32.4mF
Switching Frequency	f_{sw}	8 kHz
Resistive Load	R_{load}	50 Ω

Table 7.4 Controller Parameters for REGEN bench AFE rectifier

Modified IDA-PBC		
Parameter	**Symbol**	**Value**
Inner Current Damping	R_1 R_2	45
Outer Voltage damping	R_3	12.8
Integral voltage extension	K_{Iv}	5
Proportional Integral Control		
Parameter	**Symbol**	**Value**
Inner current Proportional gain	K_p_c	0.2894
Inner current Integral gain	K_i_c	0.000271
Outer voltage Proportional gain	K_p_v	1.2388
Outer voltage Integral gain	K_i_v	0.0543

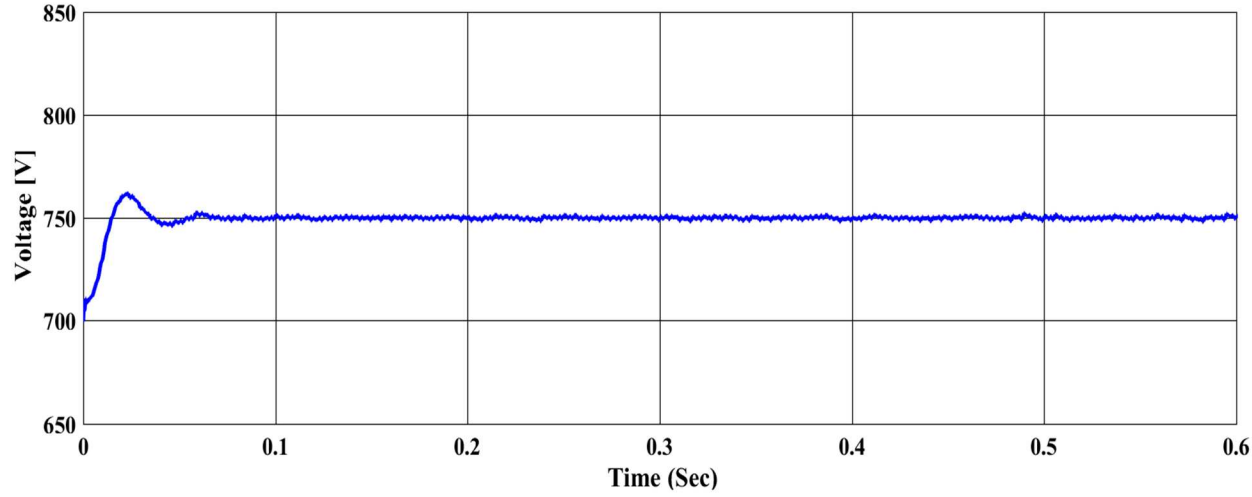

Figure 7.4 Rectifier Output Voltage for REGEN bench using Modified IDA-PBC

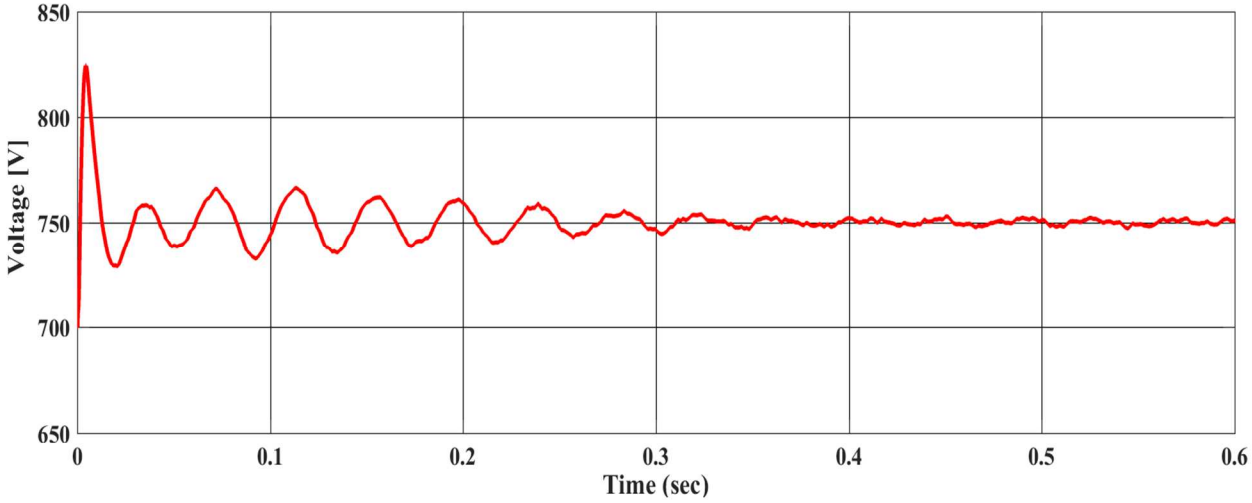

Figure 7.5 Rectifier Output Voltage for REGEN bench using Proportional Integral control

7.6 Summary

In conclusion, this chapter derives a stability controller for the active front-end rectifier of the back-to-back voltage source converter of the NCREPT system. The controller was designed by deriving the mathematical model of the AFE rectifier, transforming the model into its d-q synchronous rotating frame equivalent and finally converting it to a port-Hamiltonian model. The modified IDA-PBC controller is then designed using the port-Hamiltonian modeling formulation and the desired control objectives resulting in a closed-loop controller that stabilizes the dc link voltage controller. In addition, an integral extension is also discussed which can be added to the derived controller to mitigate any external disturbances and account for modeling errors. The Simulation results indicated that the Modified IDA-PBC is a viable option for dc voltage control.

CHAPTER EIGHT

SIMULATION RESULTS OF MICROGRID SYSTEM

8.1 System Overview

The microgrid testbed that has been configured at the NCREPT testing facility is displayed in Figure 8.1. This configuration currently shows the microgrid in islanded mode where the VVVF drive provides power downstream to the parallel REGEN benches operating as distributed energy resources. The utility input connects to a three-phase 1.5MVA 12.47Y/0.48YkV transformer which provides 480 Vrms to the main service bus one (MSB1). The main service bus provides power to the low voltage circuit breakers $F4, F5$ and $F6$ which connects to the 750kVA VVVF, HP1 bus and building loads respectively.

In Figure 8.1 displays the one-line diagram of the NCREPT microgrid configuration. The circuit breakers represented in red are viewed as closed while black circuit breakers are viewed as opened. When the $F4$ circuit breaker is closed and the $F5$ circuit breaker is opened the microgrid operates in island mode such that the VVVF drive acts as a grid-forming inverter providing power to the REGEN benches acting as loads through the $T6$ transformer which decouples the VVVF drive and REGEN bench PWM frequencies and improves the control of the VVVF drive output voltage. When circuit breakers $F5$ is closed and $F4$ is opened, the system now operates in grid-connected mode and the paralleled REGEN benches act as grid-feeding converters recirculating current through the medium voltage circuit breakers, transformers and B2B converter. The $F5$ circuit breaker is referred to as the point-of-common-coupling switch which connects to the utility grid. There are six transformers $T1 - T_6$ rated at 2.5 MVA 0.48 Δ/4.16YkV that are used in the microgrid configuration.

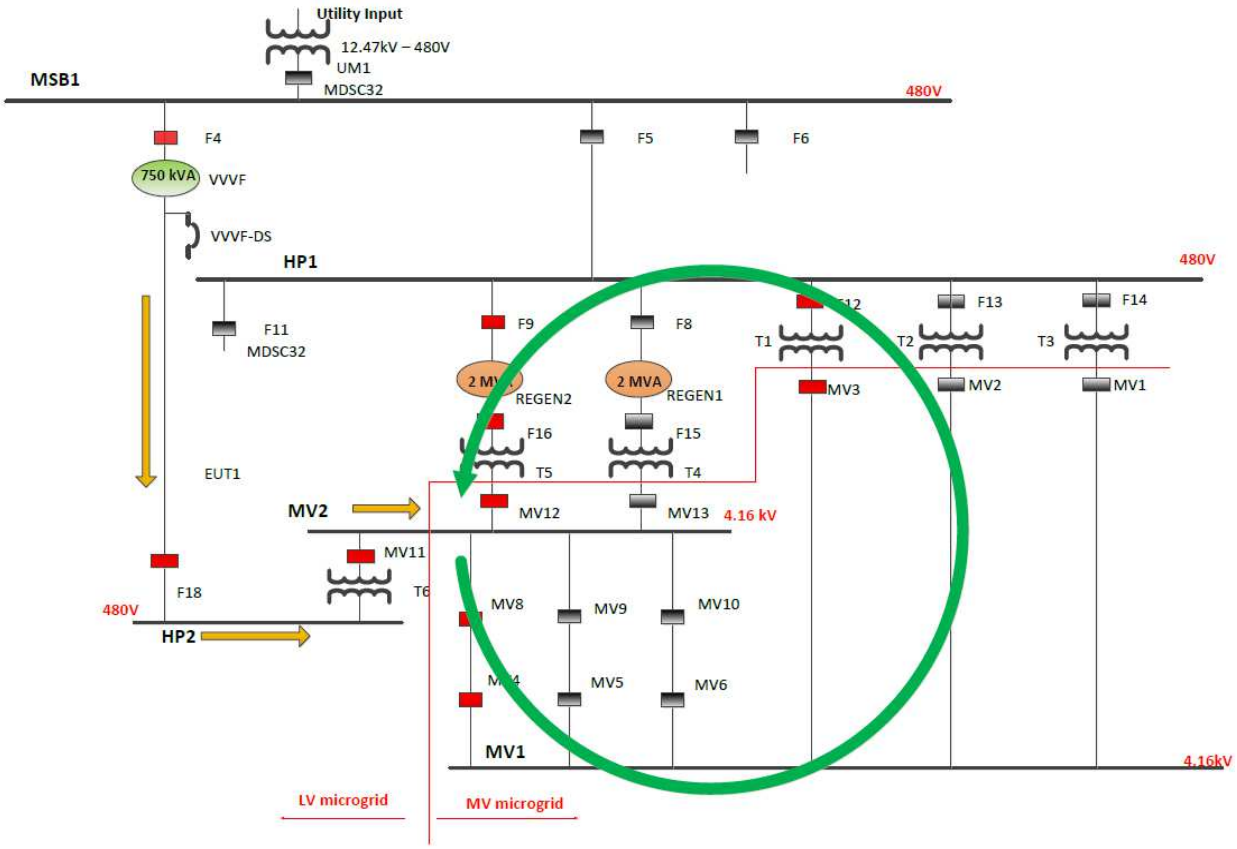

Figure 8.1 One-line diagram of Proposed NCREPT Configuration.

The system ratings and parameters for the VVVF drive and REGEN benches are given in Tables 8.1-8.6 which were obtained from the test facility shown in Appendix B. Using the system ratings and parameters, a MATLAB\Simulink^{TM} model using the SimPower toolbox is constructed and analyzed to illustrate the system's performance with the Modified IDA-PBC developed in chapters six and seven. For the initial data acquisition, three experimental results were performed to obtain the instability data of the microgrid configuration for the NCREPT system. Experimental results were obtained for the VVVF drive in standalone mode, the REGEN2 bench in standalone and island mode in which the VVVF and REGEN2 are connected. In this chapter, the virtual microgrid testbed is simulated for the VVVF drive in standalone mode, and islanded mode.

The proposed microgrid shown in Figure 8.1 is able to run in all four microgrid modes: 1) normal ac grid parallel connected mode 2) transition-to-island mode 3) island mode and 4) ac grid reconnection mode.

Table 8.1 Variable Voltage Variable Frequency Drive Parameters

Parameter	**Symbol**	**Nominal Value**
Rated Power	S_{VVVF}	750kVA
Filter Inductor	L_f	110 µH (0.135pu) @750A
AFE Filter Capacitor	C_{f-AFE}	3 x 384µF @ 100kVAR
Inverter Filter Capacitor	C_{f-INV}	3 x 960µF @ 250kVAR
DC link capacitor	C_{dc}	42.3 mF @900V
EMI Filter Capacitor	C_{EMI}	20 µF
Switching Frequency	f_{sw}	8 kHz

Table 8.2 Per Unit Values for Variable Voltage Variable Frequency Drive

Parameter	**Symbol**	**Formula**	**Nominal Value**
Power	S_{VVVF}	-	750kVA
Voltage	V_B	-	480 Vrms
Frequency	f_B	-	60Hz
Current	I_B	$P_B/\sqrt{3}V_B$	902Arms
Radian frequency	ω_B	$2\pi f_B$	377 rad/s
Base Impedance	Z_B	V_B^2/P_B	0.3072 Ω
Base Inductance	L_B	z_B/ω_B	814 µH
Base Capacitance	C_B	$1/z_B\omega_B$	8.63 mF

Table 8.3 Variable Voltage Variable Frequency Parameters

Parameter	**Symbol**	**Nominal Value**
Input voltage range	V_{in}	360-528Vac
Input frequency range	$f_{sys_{IN}}$	47-63 Hz
Output Voltage	V_{out}	120-528Vac
Output Current	I_{out}	685Arms @40 □C
Output Frequency	$f_{sys_{out}}$	45-66Hz
Overload Capacity	150 % for 60 secs, 175% 3 seconds	

Table 8.4 Per Unit Values for Regenerative Bench

Parameter	Symbol	Formula	Nominal Value
Power	S_{REGEN}	-	2MVA
Voltage	V_B	-	480 Vrms
Frequency	f_B	-	60Hz
Current	I_B	$P_B/\sqrt{3}V_B$	2405Arms
Radian frequency	ω_B	$2\pi f_B$	377 rad/s
Base Impedance	Z_B	V_B^2/P_B	0.1152 Ω
Base Inductance	L_B	z_B/ω_B	305 µH
Base Capacitance	C_B	$1/z_B\omega_B$	23.03 mF

Table 8.5 Regenerative Bench Ratings

Parameter	Symbol	Nominal Value
Input voltage range	V_{in}	120-528Vac
Input frequency range	$f_{sys_{IN}}$	45-66 Hz
Output Voltage	V_{out}	------
Output Current	I_{out}	2500Arms @20 □C
Output Frequency	$f_{sys_{out}}$	-------
Overload Capacity	110 % for 60 secs, 125% 3 seconds	

Table 8.6 Regenerative Bench Parameters

Parameter	Symbol	Nominal Value
Rated Power	S_{REGEN}	2MVA
Filter Inductor	L_f	20 µH @2500A
AFE Filter Capacitor	C_f	3 x 480µF @ 100kVAR
DC link capacitor	C_{dc}	32.4mF@ 900V
EMI Filter Capacitor	C_{EMI}	40 µF
Switching Frequency	f_{sw}	8 kHz

8.2 Operation of VVVF Drive in Standalone Mode

The modified IDA-PBC method is used to control the VVVF drive in standalone mode in Figure 8.2 In this mode, the VVVF drive provides the energy which compensates the losses in the virtual microgrid by the green path (F4 → F18 → MV11 →MV2). The VVVF drive is isolated by the transformer T6 and power is sent to the HP1 bus by the red path (MV8 → MV4 → MV3 → F12 →). A 100kW resistive load bank was used as the equipment under test. Figure 8.3 displays the matlab simulation model of the VVVF in standalone mode where the grid input and impedances represent the thevanin equivalent circuit of the grid as seen by the facility. The utility transformer as mentioned earlier has an impedance of 5.9% with an impedance angle of -80 degrees. The base impedance on the secondary side of the transformer is 0.1536 Ω.

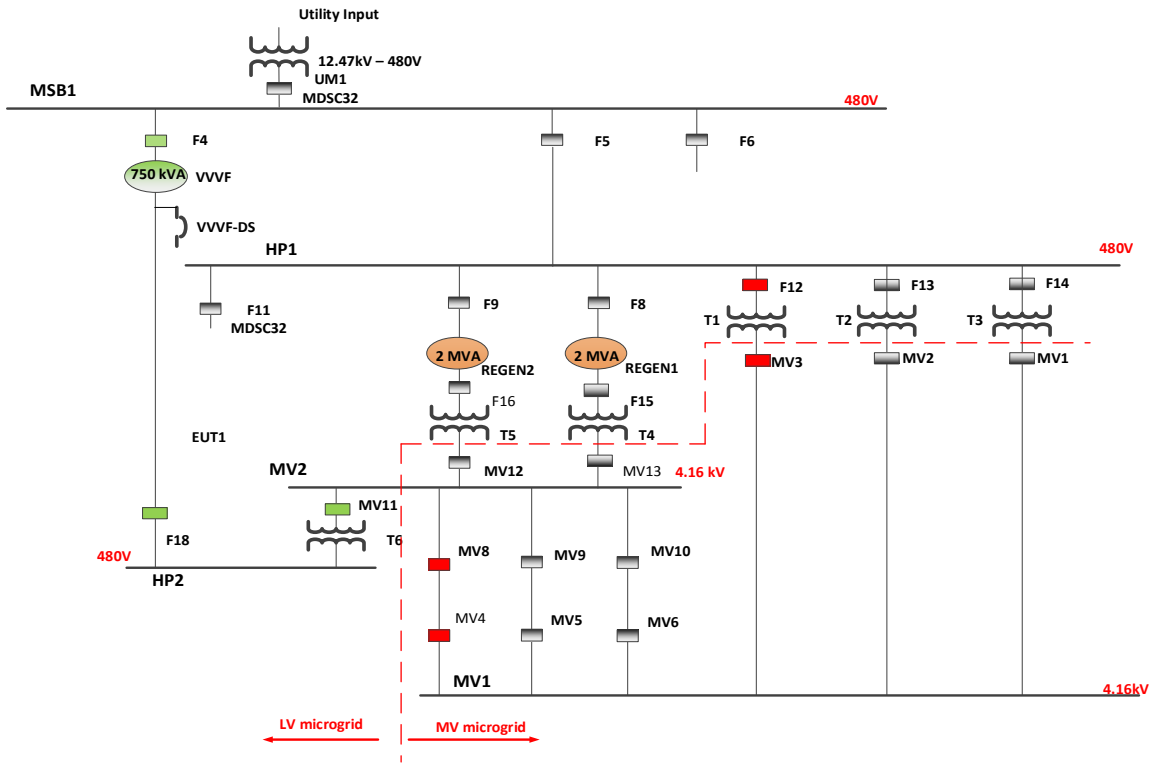

Figure 8.2 One-line diagram of VVVF drive in Standalone Mode.

The actual grid impedance is 9.1 mΩ at an angle of -80 degrees. This translates to a grid resistance and inductance of 1.58 mΩ and a 23.67 μH respectively. In the NCREPT system, the transformer is connected to the main service bus (MSB1) to the F4 circuit breaker which allows the microgrid to operate in islanded mode and serves as the disconnect switch of the VVVF in the NCREPT system. This electromagnetic switch with fault control responds to the direct control of the NCREPT user interface. The capacitor bank at the output of the F4 CB provides voltage stability.

The start-up circuitry of the VVVF drive consists of the $F4$ circuit breaker, a three-phase relay, and a 0.4 Ω soft start resistor. The soft-start or bypass resistor is necessary for reducing the inrush currents in the ac filter and dc link capacitors. When the F4 circuit breaker is turned on the pre-charging process of the dc bus capacitor begins. At this time, the relay is opened forcing current to flow through the soft-start resistor limiting the current as it begins to charge the dc bus capacitor. The soft start resistor is needed to prevent the dc bus capacitor from acting as a short circuit drawing excessive currents from the main service bus. The relay is then closed, which bypasses the soft-start resistor allowing a low impedance path to the VVVF drive. Once the bus voltage is pre-charged to $678V_{LLpk}$ and the current is flowing through the relays for some time, a charge command for the rectifier is activated increasing the dc bus voltage to 750Vdc. Once the dc bus voltage is stable at the commanded voltage, the inverter is commanded to operate in grid-forming mode providing 480Vrms to the down-stream circuitry consisting of the 100kW resistor bank equipment under test, $F18$ circuit breaker, $MV11$ circuit breaker and the $T6$ transformer.

8.2.1 Simulation of VVVF drive in Standalone Mode

The VVVF drive in standalone mode is simulated to emulate its operation at the NCREPT testing facility. The input impedance chosen were calculated to be 1.58 mΩ and 23.67μH for the system. The Modified IDA- PBC controller parameters are shown in Table 8.7 for the system's operation. As mentioned in chapter four, the inner loop current controller is to be designed faster than the outer loop voltage controller for the grid-forming converter hence the damping variables were chosen to accomplish to this task to ensure correct operation.

The VVVF drive is provided with a peak line-to-line voltage of $678V_{LLpk}$ illustrated in Figure 8.4 through the main contactor circuit breaker $F4$ which closes at 12.5ms. At 50ms, the relay switch is closed bypassing the soft start resistor and the VVVF dc bus capacitor begins to pre-charge to the peak line-to-line voltage of 678Vdc. At this time, a transient can be seen on the input current waveform in Figure 8.5.The input current has a total harmonic distortion (THD) of 10.78% but is within the continuous range of 900Arms given in Table 8.2 for the VVVF drive parameters. At 0.1 seconds, the dc bus controller of the VVVF drive turns on increasing the bus voltage to the commanded voltage of 750Vdc illustrated in Figure 8.6. Once the dc bus voltage is stabilized to 750Vdc, the ac voltage controller is turned on at 0.18 seconds in Figure 8.7-8.8 and provides 480Vrms voltage to the downstream circuitry to the equipment under test.

The VVVF drive output current in Figures 8.9 is 450Arms which is also in the within the rated continuous current limit given in Table 8.3.The current flows to the low voltage bus $HP2$ and through the medium voltages buses shown in Figure 8.2. Reiterating from chapter four and six, the VVVF drive acts as a grid-forming converter providing the AC microgrid voltage of 480Vrms at 60Hz to the downstream loads. It can be deduced from the simulation

results that the Modified IDA-PBC of the active front-end rectifier stabilizes the dc bus voltage and ensures a stable output voltage.

Table 8.7 Modified IDA-PBC Damping Resistances for VVVF Standalone Mode

Active Front End Rectifier		
Parameter	**Symbol**	**Value**
Inner current damping	R_1, R_2	12
Outer Voltage damping	R_3	8.1
Integral voltage extension	K_{Iv}	23.50
DC-AC Inverter		
Inner current damping	R_1, R_2	1
Outer Voltage damping	R_3, R_4	0.1

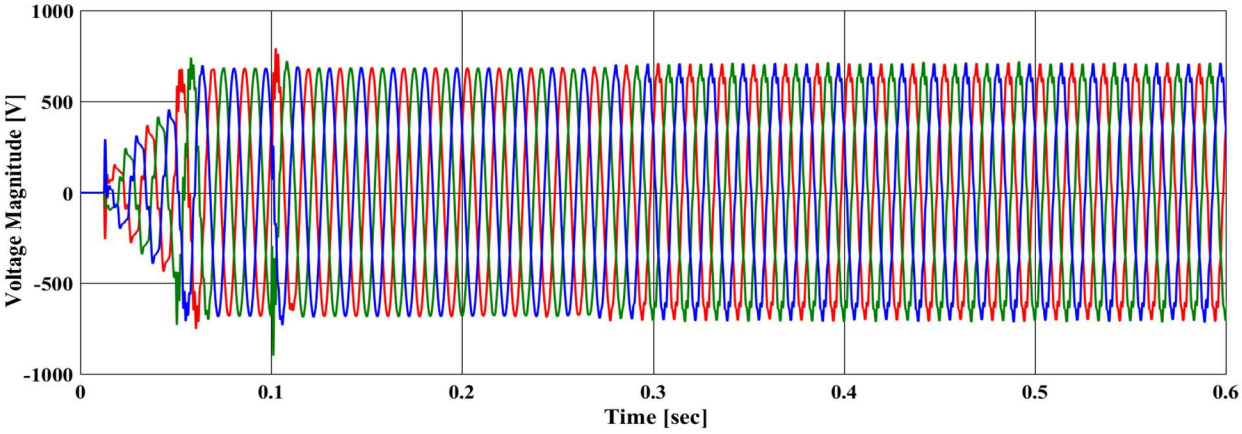

Figure 8.3 VVVF drive Input line-to-line voltage

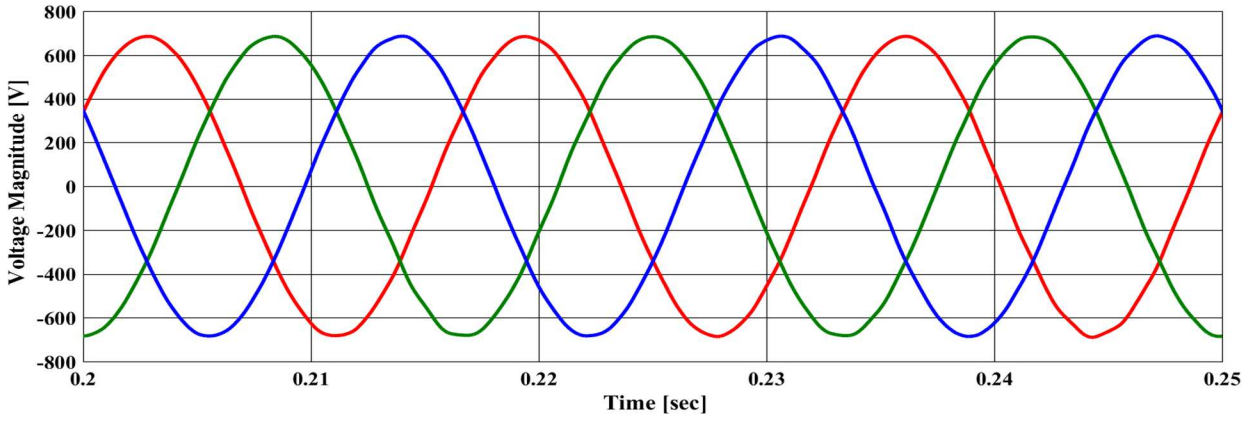

Figure 8.4 VVVF drive Input line-to-line voltage (zoomed)

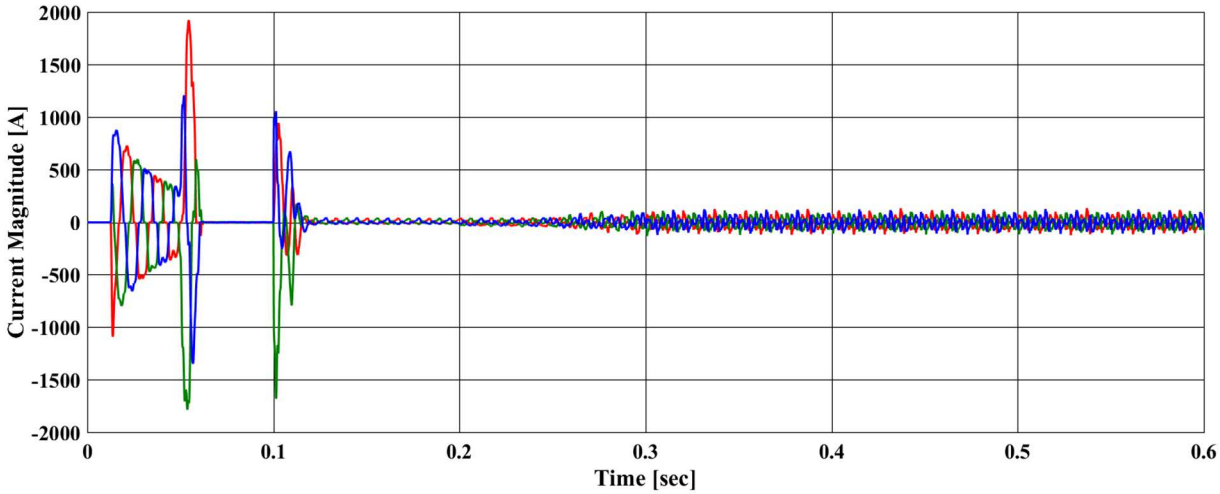

Figure 8.5 VVVF Input Current.

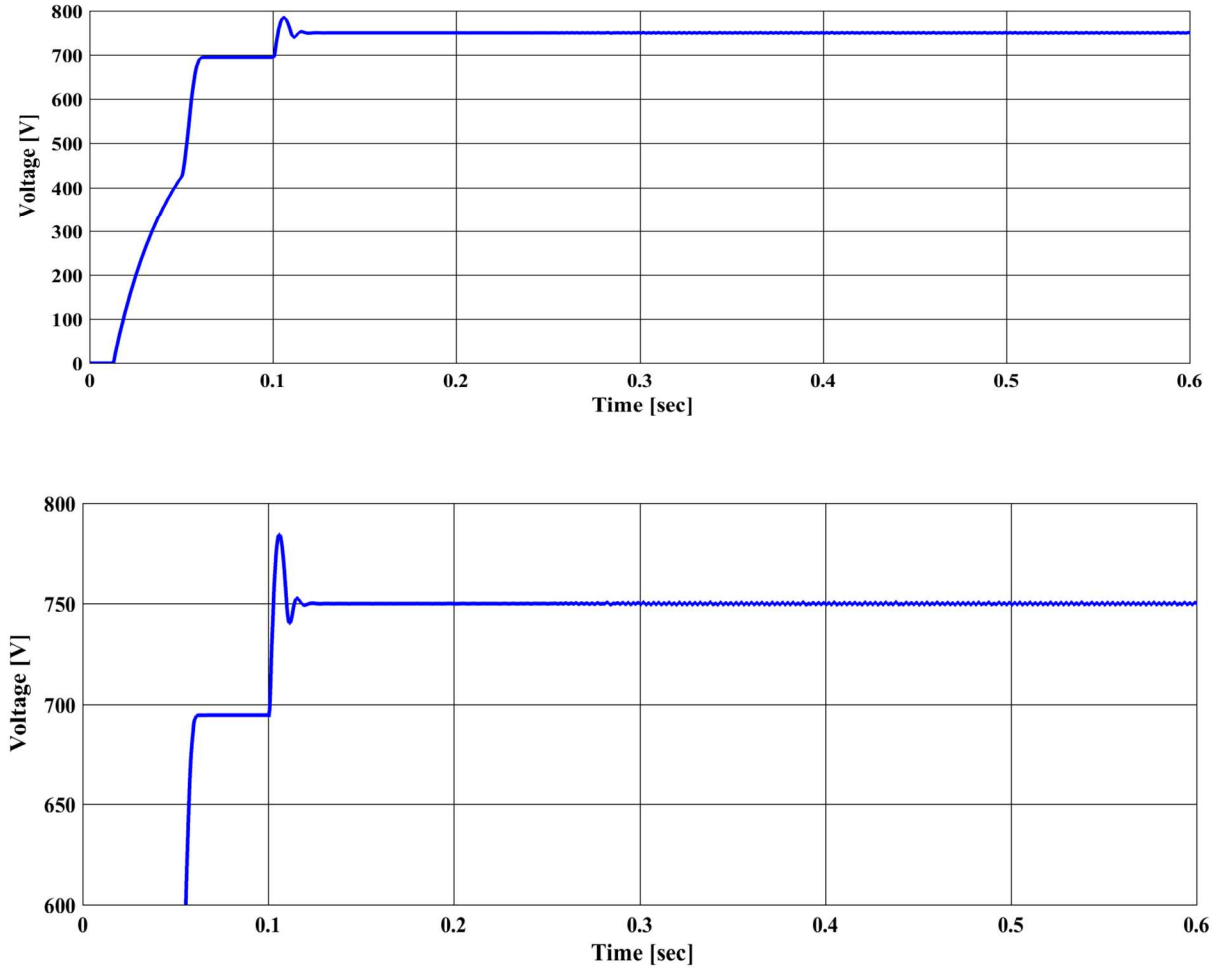

Figure 8.6 DC Link capacitor voltage (top) and zoomed waveform (bottom)

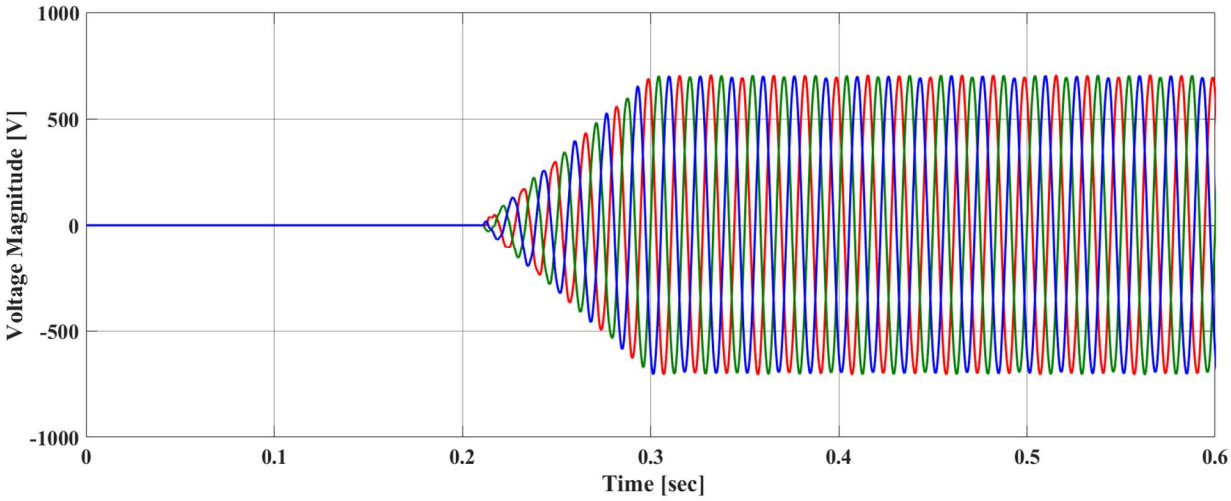

Figure 8.7 VVVF Output voltage starting at 0.25 seconds.

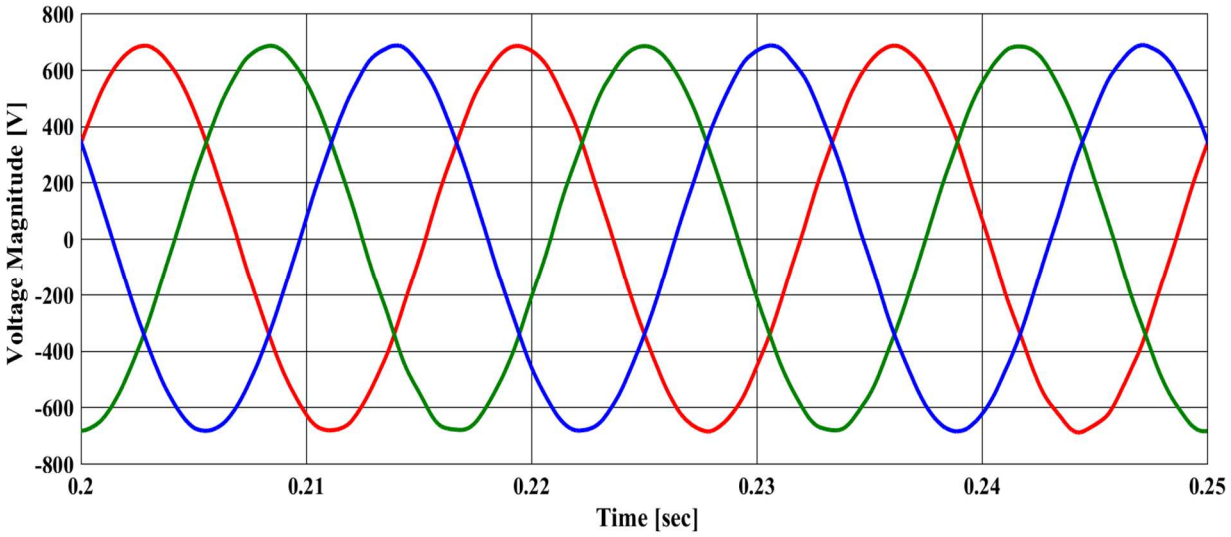

Figure 8.8 VVVF Output voltage zoomed waveform.

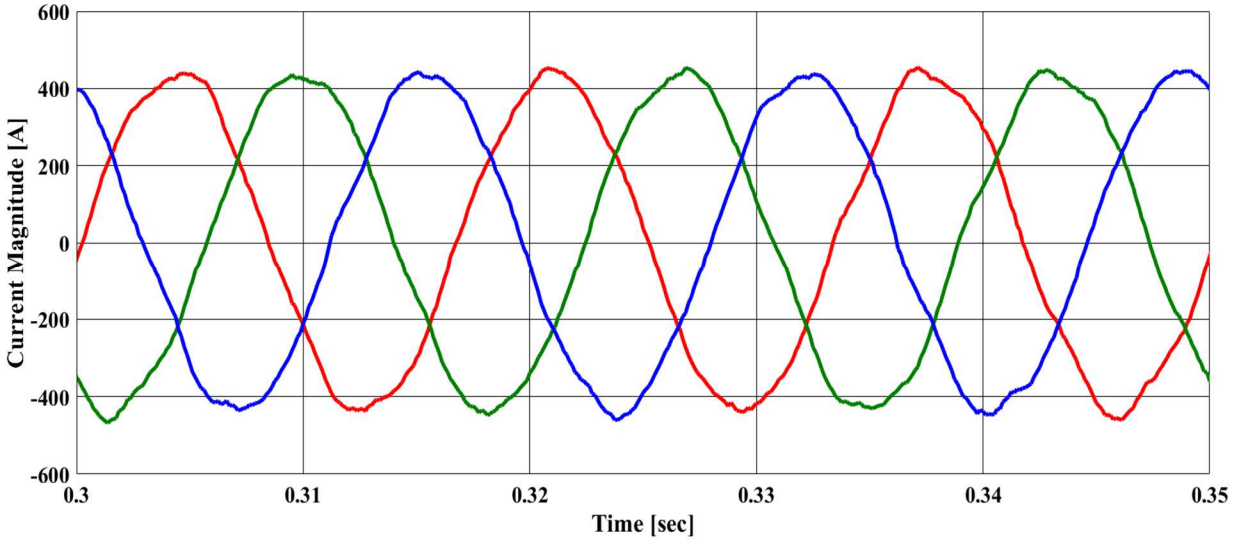

Figure 8.9. VVVF Output Current.

8.3 Simulation of the Microgrid in Island Mode with Weak Grid Interface

The virtual microgrid configuration is shown in Figure 8.10 where the VVVF drive is connected to the utility grid via the $F4$ circuit breaker and the output of the VVVF drive is connected to transformer $T6$, which decouples the VVVF and REGEN bench pwm frequencies and improves the control of the VVVF output voltage. The VVVF provides the energy which compensates the losses in the virtual microgrid by the green path (F4 → F18 → MV11 →) then the Regen bench recycles power by the red path (MV12 → MV8 → MV4 → MV3 → F12 → F9 →).

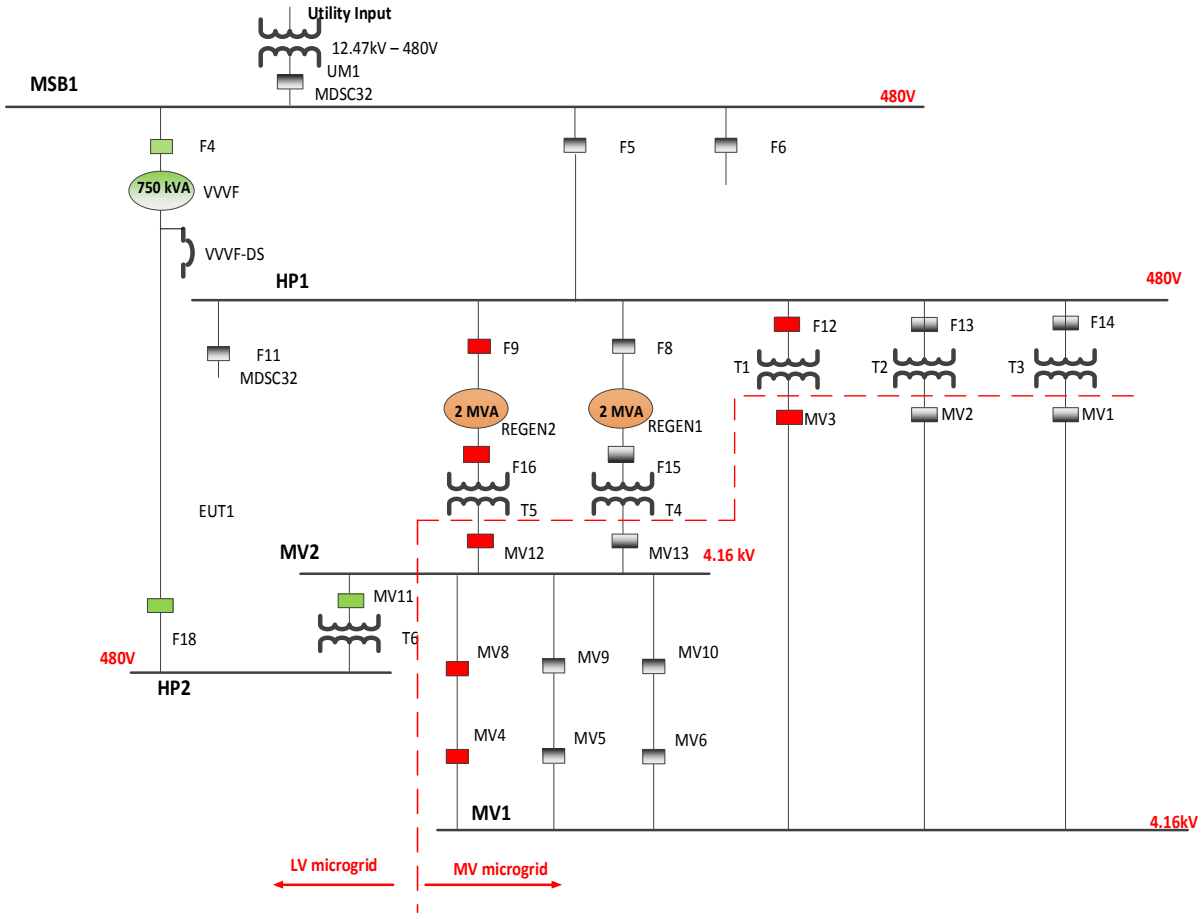

Figure 8.10 One-line diagram of Microgrid Configuration in Island Mode.

8.3.1 Microgrid System Operation

The microgrid system is simulated using the decoupled proportional integral controller and the Modified-IDA-PBC. The controller parameters are provided in Tables 8.8 -8.10 and the controller design calculations are given in Appendix A. The system operates using the startup circuitry of the VVVF drive discussed in section 8.1 where the circuit breaker $F5$ closes at 12.5 ms and the relay switch of the pre-charge circuit closes at 50ms quickly pre-charging the VVVF dc bus capacitor to just below the peak value of the line to line voltage of 678 V_{LL}. At 0.1 seconds, the dc bus controller of the AFE rectifier of the VVVF drive turns on, increasing the bus voltage to the commanded 750 V. There is a small transient input current at each of these times at the VVVF

drive draws current form the source to charge the bus capacitor. Once the bus voltage is at the commanded level, the VVVF drive is ready to start providing voltage to the input bus of the regeneration benches. The ac voltage controller turns on at 0.14 seconds and the output voltage increases to a 678 V_{LL} supplying the regenerative bench. This causes the diodes of the regeneration drive to begin to conduct, charging the regeneration drive dc bus capacitor to 678 Vdc.

The input converter of the regeneration drive begins to operate at 0.30 seconds, increasing the regeneration drive dc bus voltage to the commanded 750 V. This results in an increase of the VVVF output current and the regeneration drive input current which represents a steady draw from the VVVF drive to supply losses in the regeneration bench. At 0.45 seconds the load simulator switch is enabled connecting the output of the regeneration drive to the common ac $HP1$ bus. There is a brief transient visible in the VVVF and regeneration bench currents at this time. The current draw from the VVVF increases slightly, and increases again at 0.55 seconds when the regeneration bench turns on fully and begins to recycle power. The simulation results for the microgrid configuration using the control methods are shown in Figures 8.11-8.17.

Table 8.8 Proportional Integral Control Parameters for REGEN bench in Island Mode

Active Front-End Rectifier		
Parameter	**Symbol**	**Value**
Inner current Proportional gain	$K_p\_c\_regen$	0.2894
Inner current Integral gain	$K_i\_c\_regen$	0.000271
Outer voltage Proportional gain	$K_p\_bus\_regen$	1.2338
Outer voltage Integral gain	$K_i\_bus\_regen$	0.0543
DC-AC Inverter		
Parameter	**Symbol**	**Value**
Load current Proportional gain	$K_p\_loadsim$	0.0027
Load current Integral gain	$K_i\_loadsim$	2.1705

Table 8.9 Proportional Integral Control Parameters for VVVF in Island Mode

Active Front-End Rectifier		
Parameter	**Symbol**	**Value**
Inner current Proportional gain	$K_p\_c\_vvvf$	2.8717
Inner current Integral gain	$K_i\_c\_vvvf$	0.0090
Outer voltage Proportional gain	$K_p\_bus\_vvvf$	20.8947
Outer voltage Integral gain	$K_i\_bus\_vvvf$	1.3799
DC-AC Inverter		
Parameter	**Symbol**	**Value**
Inner current Proportional gain	$K_p\_acc\_vvvf$	1.4325
Inner current Integral gain	$K_i\_acc\_vvvf$	0.0022
Outer voltage Proportional gain	$K_p\_ac\_vvvf$	5
Outer voltage Integral gain	$K_i\_ac\_vvvf$	0.125

Table 8.10 Modified PBC Damping Resistances for VVVF Islanded Mode

Active Front End Rectifier		
Parameter	**Symbol**	**Value**
Inner current damping	R_1, R_2	18
Outer Voltage damping	R_3	18
Integral voltage extension	K_{Iv}	2
DC-AC Inverter		
Inner current damping	R_1, R_2	1
Outer Voltage damping	R_3, R_4	0.1

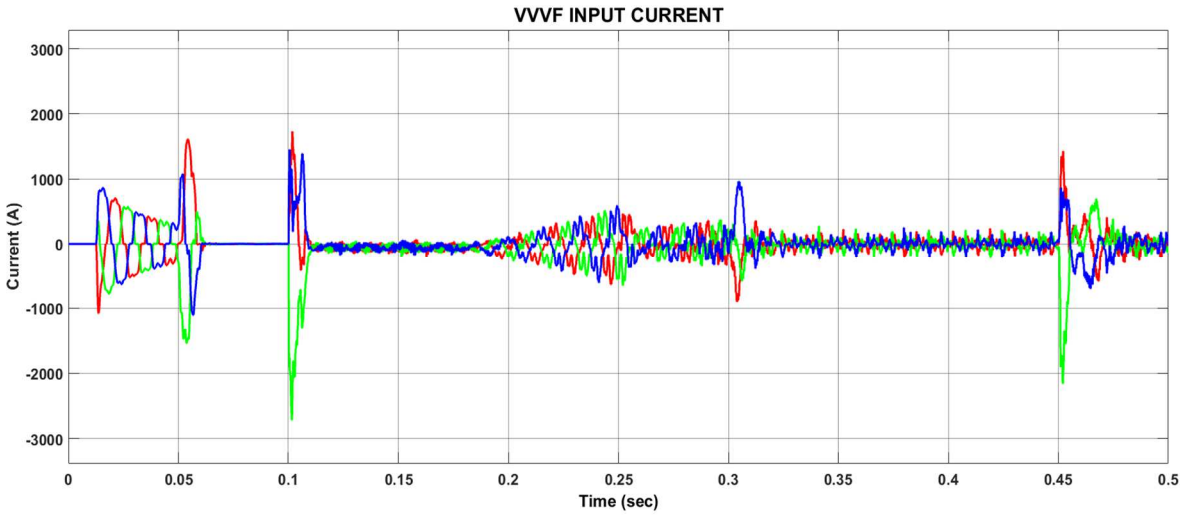

Figure 8.11. VVVF Input Current with Modified IDA-PBC.

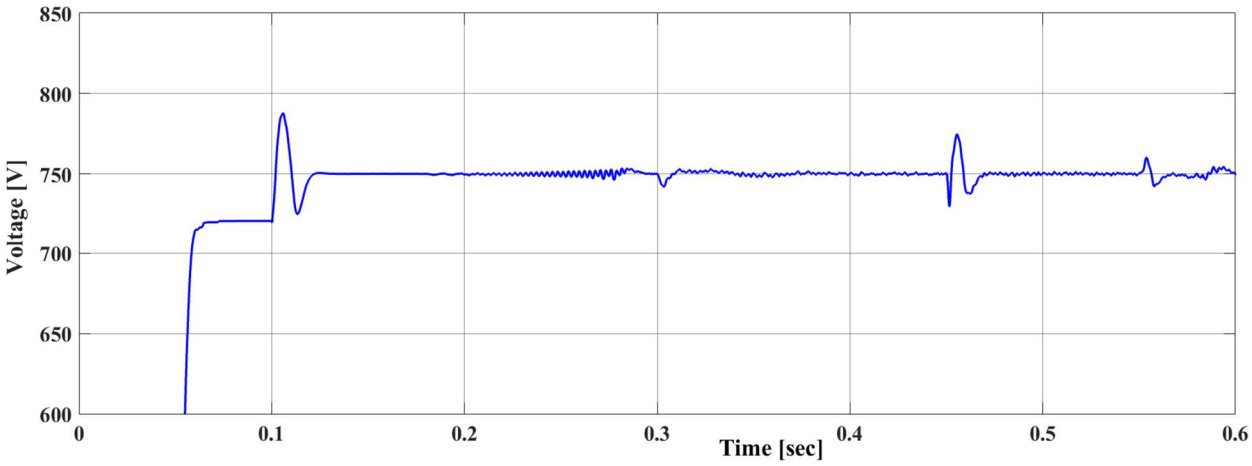

Figure 8.12. VVVF DC link Voltage using the Proportional Integral Control.

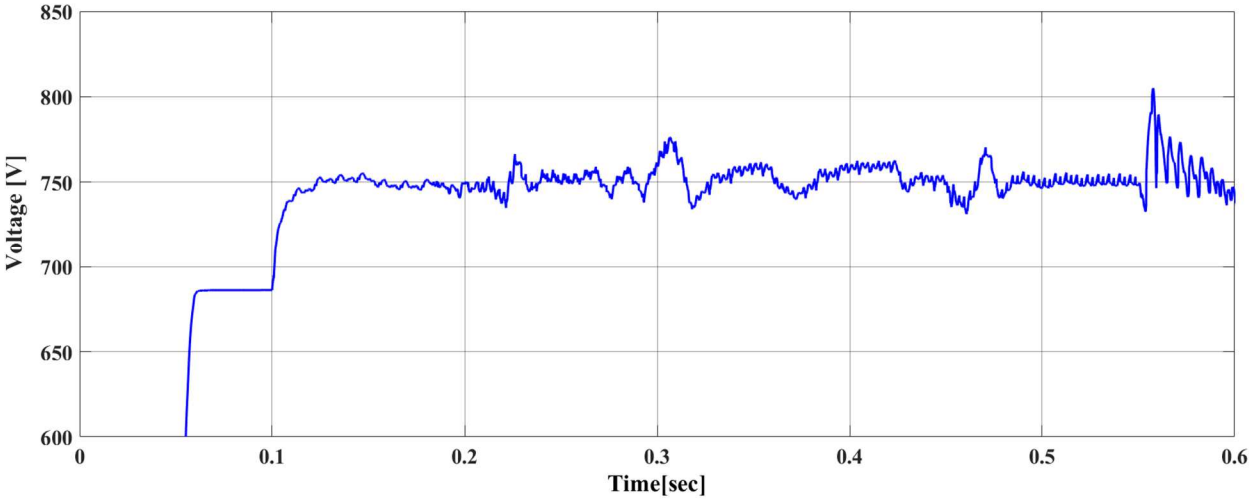

Figure 8.13. VVVF DC link Voltage using the Modified IDA-PBC.

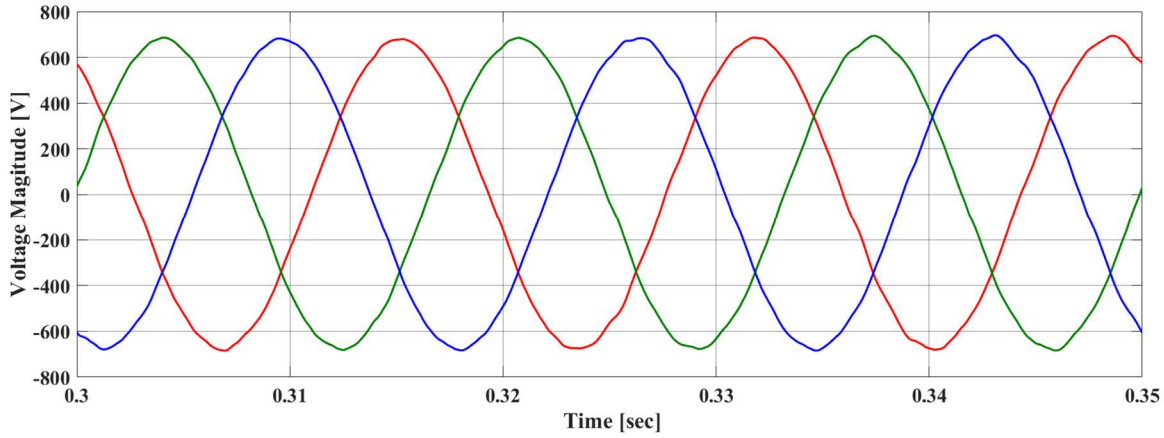

Figure 8.14. VVVF Output Voltage with Proportional Integral control.

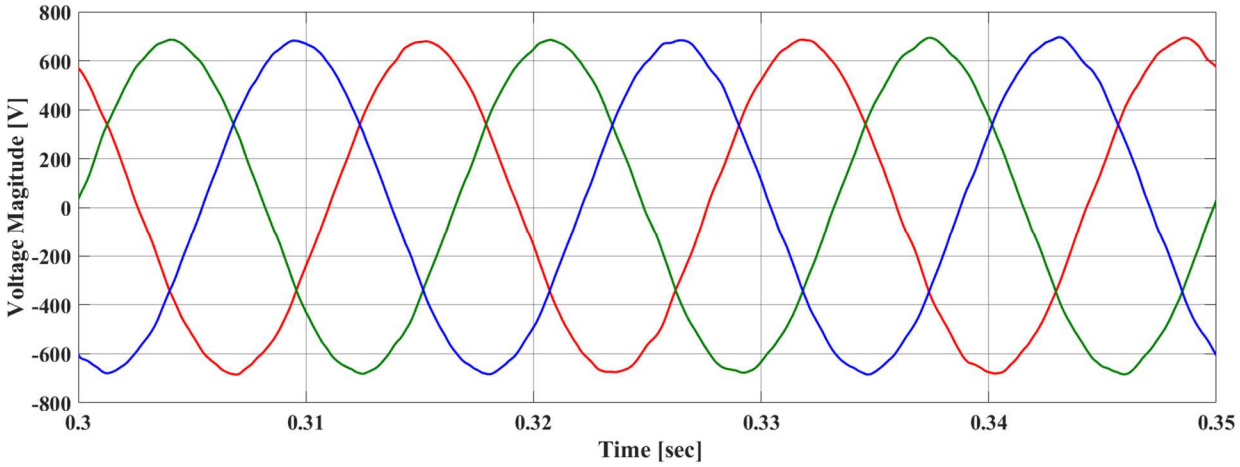

Figure 8.15. VVVF Output Voltage with Modified IDA-PBC.

The regenerative bench voltage waveforms in Figure 8.16 and 8.17 shows that the REGEN dc bus voltage is enabled at 0.3 seconds and charges to 780Vdc. At 0.45 seconds the load simulator breaker is enabled and the current increases to 758V. At 0.55 seconds, the dc bus voltage sag when a reference current of 1.0 per unit is injected. Although the dc bus voltage is oscillatory the proportional controller is able to stabilize the voltage at 750Vdc.

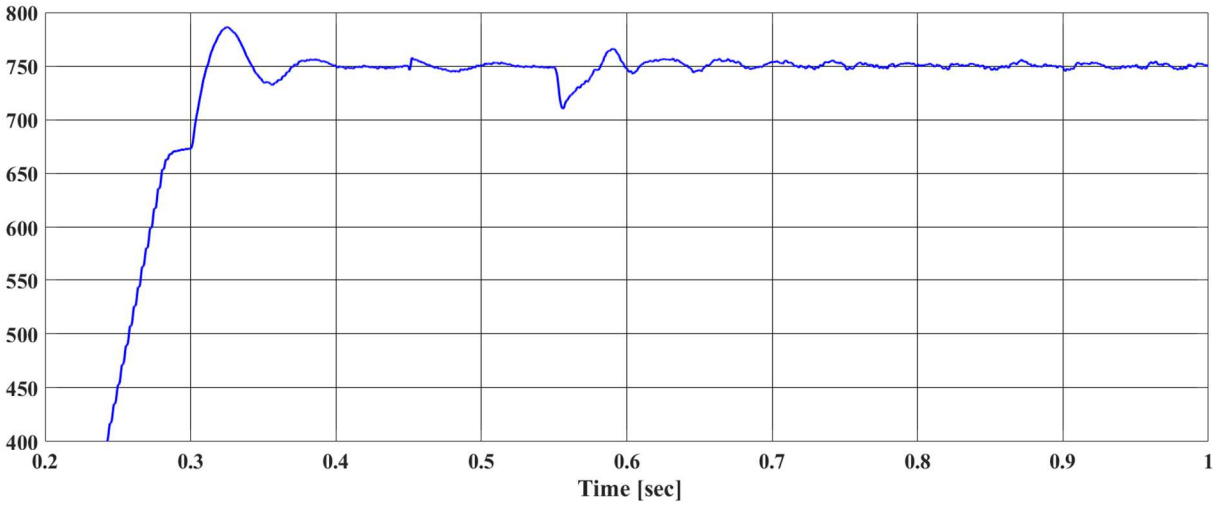

Figure 8.16. REGEN BUS Voltage with PI controller

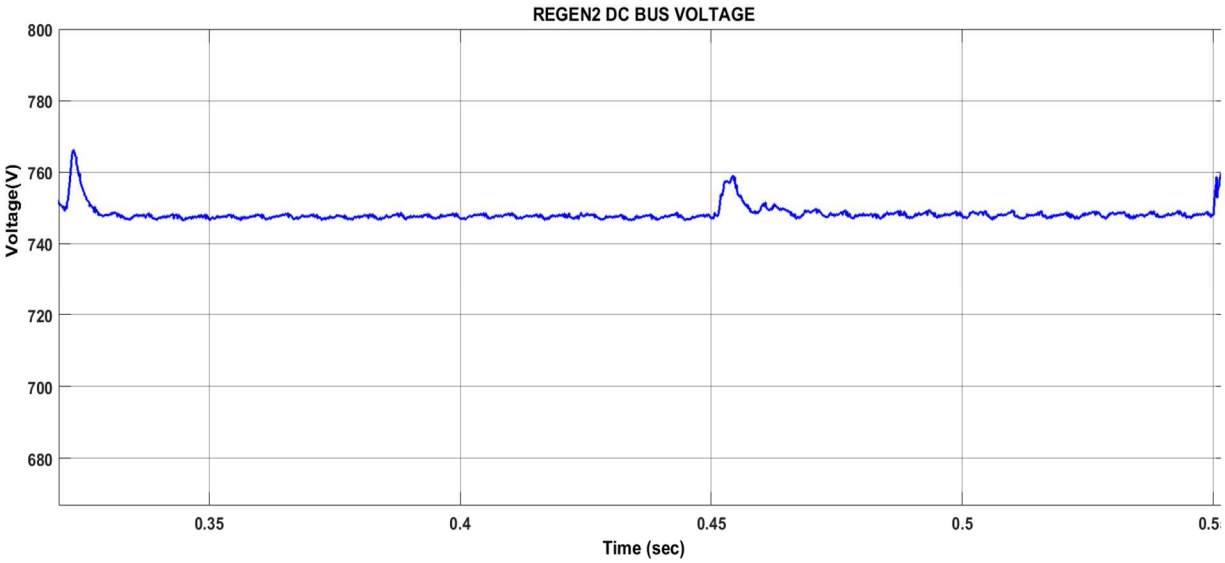

Figure 8.17. REGEN BUS Voltage with Modified IDA-PBC.

8.4 Discussion of Results

Reiterating from chapter one, there are three types of stability issues which are common in microgrid systems which are the following: small-signal stability, voltage stability and transient stability. From the above simulations it can be clearly observed that the load dynamics and feedback controller can easily contribute to small signal and voltage instability in the dc bus voltages. The microgrid system with the proportional integral control design featured current limiters and the synchronous reference frame phase locked loop grid synchronization technique.

Hence if the system were to transition from islanded to grid-connected mode or vice versa, the system would experience more voltage and small signal instabilities in terms of grid voltage tracking and load variations due to the degradation in the SRF-PLL performance in modes of transitions. The small signal instabilities can also be attributed to the controller design, which features four proportional integral controllers for the VVVF drive and two proportional integral controllers for the REGEN bench. The dc bus voltages for the VVVF drive and the REGEN are stabilized to 750Vdc but does not account for load variations.

When the microgrid system is simulated with the Modified IDA-PBC, the dc link voltage of the VVVF drive and REGEN bench are less oscillatory and experience less voltage spikes and voltage sags as compared to simulations performed with the PI controller. This is attributed to the fact that Modified IDA-PBC takes into consideration the entire structure of the system and reduces the need to construct bode plots to determine various bandwidths and cross-over frequency to ensure stability. The controller utilizes the DSOGI-FLL grid synchronization technique, which allows efficient tracking of the grid voltage and frequency in modes of transitions.

8.5 Summary

This chapter presented simulations of the operation of the variable voltage variable frequency drive as the grid-forming converter and islanded mode of the microgrid configuration in which the VVVF drive and REGEN bench are connected. The VVVF drive in standalone mode was simulated to observe the performance of the Modified-IDA PBC. The controller performed as expected regulating the dc bus voltage and providing the grid-forming voltage of 480Vrms. The island mode microgrid configuration was simulated using the Modified-PBC and the decoupled proportional integral control. A comparison analysis of the system's operation was performed and the Modified-IDA PBC was shown to provide better performance in terms of dc voltage stability control for the VVVF drive and REGEN bench.

CHAPTER NINE

CONCLUSION AND FUTURE WORK

9.1 Conclusions

Power electronics plays a major role in grid modernization from its interconnection with renewable energy technologies to energy efficiency improvement in electric utilities. Efficiently managing electricity among power electronic-based sources and loads is essential in electronic power transmission and distribution grids. Microgrids in particular are contributing to the decentralization of distributed energy resources in the utility grid and are advantageous in improving energy reliability and sustainability, which tends to be an issue related with central power stations in addition to an ageing power grid that exist in some countries. The stability, resiliency and power quality of electronic power grids is essential for future grid modernization.

In this dissertation a stability control technique was designed and implemented for stabilizing the dc link voltage of interconnected back-to back voltage source converters at the National Center for Reliable Energy Transfer. The theoretical concepts of Port-Hamiltonian Dirac structures, passivity and microgrid system architectures were used to derive novel stability theorems for voltage-source converter based microgrid systems.

To observe the current system stability of the NCREPT system a robust analysis of the derived 24^{th} order system was performed using the concept of parameter uncertainty based on the edge theorem. As with weak grid systems the input impedance is typically responsible for instabilities that occur downstream along the voltage feeder. The transformer impedance was varied and root space plot of the system showed that it was not robustly stable. An eigenvalue analysis was also performed of the closed-loop system to see observe the systems stability as the input impedance increased. The NCREPT microgrid configuration has characteristics of various classes of voltage source converter based microgrids hence it is used a baseline model such that if it can be stabilized

via a passivity-based controller then all classes of voltage source converters can be stabilized using a passivity-based control method. This analysis verified that the Modified-IDA PBC can be considered for stabilizing the microgrid configuration of the NCREPT system. The Modified IDA PBC was designed to ensure voltage stability of the dc link voltage of the rectifier and output voltage stability of the inverter of the grid-forming VVVF drive. In the REGEN bench, the grid-feeding converter, the proposed converter is also designed to ensure the dc link voltage stability of the rectifier and allows the load simulator to recirculate power in the system.

The NCREPT system was simulated in three modes 1) VVVF standalone mode 2) REGEN standalone mode (grid-connected mode) and 3) Islanded mode in which the VVVF and REGEN are interconnected. The system was simulated using a decoupled proportional integral controller and the results were compared to the Modified IDA-PBC. From the simulations results it can be deduced that the Modified IDA-PBC is a viable method for ensuring dc link voltage stability in a weak grid system.

9.2 Recommendations for Future Work

Some research recommendations based on this dissertation are given below.

9.2.1 Implementing the Modified IDA-PBC Microgrid system prototype

A scaled-down low power microgrid prototype can be developed to test the modified IDA-PBC controller for stabilizing interconnected voltage source converters and verifying the new control algorithm before implementing it on the 13.8kV NCREPT system. The system should be designed to implement the four mode of microgrid operations 1) grid-connected mode 2) transition to island mode 3) island mode and 4) reconnection mode. Other control levels should also be explored i.e. secondary and tertiary control and the passivity-based control can be applied to the

case when two regenerative benches are in parallel. In the case of the load simulator, a zero-sequence technique should be employed to minimize the distorted load currents.

9.2.2 Exploring Robust Control methods for Microgrid Systems

The power-shaping controller described in chapter three is another passivity-based control method that should be explored. The power-shaping controller is an extension of the energy-shaping controller where the power of the system is modified rather than the energy of a system. It is also a model-based controller, which makes use of the Brayton Moser formulation. The Brayton Moser has been used in ac-dc and dc-dc systems but there is no literature to the author's knowledge where it has been implemented in controlling voltage source converters in a microgrid system. Other robust control methods such as integrator back-stepping control and a dynamic sliding mode control can also be used since their design is based on the principle of Lyapunov's second method.

Additionally, adaptive control methods based on the passivity-based control should also be considered researching especially in microgrid modes of operation such as the transition to island mode and grid-reconnection mode where the frequency and voltage must be accurately tracked. By incorporating an adaptive method this reduces the need for solving complex mathematical (PDE) equations analytically. It also enhances the performance of the systems by improving the rate of convergence of system trajectories thereby ensuring system stability.

REFERENCES

[1] I. Standards, C. Committee, D. Generation, and E. Storage, "IEEE Guide for Design , Operation , and Integration of Distributed Resource Island Systems with Electric Power Systems IEEE Standards Coordinating Committee 21 Sponsored by the," 2011.

[2] K. A. and B. S. Parhizi, S. Lotfi H., "State of the Art in research on Microgrids: A Review," *IEEE Access*, vol. 3, no. 1, pp. 890–925, 2015.

[3] Y. W. Li and C. N. Kao, "An accurate power control strategy for power-electronics-interfaced distributed generation units operating in a low-voltage multibus microgrid," *IEEE Trans. Power Electron.*, vol. 24, no. 12, pp. 2977–2988, 2009.

[4] H. A. Mantooth, Y. Liu, C. Farnell, F. Zhang, Q. Li, and J. Di, "Securing DC and Hybrid Microgrids H.," *2015 IEEE 1st Int. Conf. Direct Curr. Microgrids, ICDCM 2015*, p. 285–286c, 2015.

[5] T. C. Green and M. Prodanovi, "Control of inverter-based micro-grids," in *Electric Power Systems Research*, 2007, vol. 77, no. 9, pp. 1204–1213.

[6] Y. Liu, C. Farnell, K. George, H. A. Mantooth, and J. C. Balda, "A Scaled-Down Microgrid Laboratory Testbed," in *2015 IEEE Energy Conversion Congress and Exposition, ECCE 2015*, 2015, pp. 1184–1189.

[7] Y. Liu, C. Farnell, J. C. Balda, and H. A. Mantooth, "A 13.8-kV 4.75-MVA Microgrid Laboratory Test Bed," in *Applied Power Electronics Conference and Exposition (APEC), 2015 IEEE, Charlotte, NC*, 2015, pp. 697–702.

[8] T. Considine, W. Cox, and E. G. Cazalet, "Understanding Microgrids as the Essential Architecture of Smart Energy," 2012.

[9] R. Majumder, "Some Aspects of Stability in Microgrids," *IEEE Trans. Power Syst.*, vol. 28, no. 3, pp. 3243–3252, 2013.

[10] R. Majumder, "Modeling , Stability Analysis and Control of Microgrid .," Queensland University of Technology, 2010.

[11] M. A. Sofla and L. Wang, "Control of DC-DC Bidirectional Converters for Interfacing Batteries in Microgrids," in *2011 IEEE/PES Power Systems Conference and Exposition, PSCE 2011*, 2011.

[12] J. He and Y. W. Li, "Generalized Closed-Loop Control Schemes with Embedded Virtual Impedances for Voltage Source Converters with LC or LCL," *IEEE Trans. Power Electron.*, vol. 27, no. 4, pp. 1850–1861, 2012.

[13] J. Schifer, D. Zonetti, R. Ortega, A. Stankovicc, T. Sezid, and J. Raischa, "Modeling of microgrids—from fundamental physics to phasors and voltage sources," *Automatica*, no. MAY, pp. 1–15, 2015.

[14] M. Ashourloo, A. Khorsandi, and H. Mokhtari, "Stabilization of DC Microgrids with Constant-Power Loads by an Active Damping Method," in *PEDSTC 2013 - 4th Annual International Power Electronics, Drive Systems and Technologies Conference*, 2013, pp. 471–475.

[15] Y. A. R. I. Mohamed, H. H. Zeineldin, M. M. A. Salama, and R. Seethapathy, "Seamless Formation and Robust Control of Distributed Generation Microgrids via Direct VoltageControl and Optimized Dynamic Power Sharing," *IEEE Trans. Power Electron.*, vol. 27, no. 3, pp. 1283–1294, 2012.

[16] D. Haribabu, A. Vangari, and J. N. Sakamuri, "Dynamics of Voltage Source Converter in a Grid Connected Solar Photovoltaic System," in *2015 International Conference on Industrial Instrumentation and Control (ICIC)*, 2015, no. March, pp. 360–365.

[17] J. Schiffer, R. Ortega, J. Raisch, and T. Sezi, "Stability and power sharing in microgrids," Berlin University of Technology, 2015.

[18] North American Electric Reliabiliy Corporation (NERC), "Integrating Inverter- Based Resources into Weak Power Systems," 2017.

[19] A. Rodriguez-Cabero and M. Prodanovic, "Stability analysis for weak grids with power electronics interfaces," in *IECON Proceedings (Industrial Electronics Conference)*, 2016, pp. 2402–2407.

[20] N. Bottrell, M. Prodanovic, and T. C. Green, "Dynamic stability of a microgrid with an active load," *IEEE Trans. Power Electron.*, vol. 28, no. 11, pp. 5107–5119, 2013.

[21] N. R. E. Laboratory, "Midwest Interconnection Seams Study," 2017.

[22] D. Zonetti, "Energy-based modelling and control of electric power systems with guaranteed stability properties," Delft University of Technology, 2016.

[23] J.-J. E. Slotine and W. Li, *Applied Nonlinear Control*, 1st ed. Upple Saddle River, New Jersey: Prentice Hall, 1991.

[24] H. K. Khalil, *Nonlinear Systems 3rd edition*, 1st ed. Upple Saddle River, New Jersey, 2002.

[25] M. Mehrasa, E. Pouresmaeil, and J. P. S. Catalao, "Direct Lyapunov Control Technique for the Stable Operation of Multilevel Converter-Based Distributed Generation in Power Grid," *IEEE J. Emerg. Sel. Top. Power Electron.*, vol. 2, no. 4, pp. 931–941, 2014.

[26] H. Kömürcügil and O. Kükrer, “Lyapunov-Based Control for Three-Phase PWM AC/DC Voltage-Source Converters,” *IEEE Trans. Ind. Electron.*, vol. 46, no. 3, pp. 544–553, 1999.

[27] W. Liu, L. Liu, D. A. Cartes, S. Member, and X. Wang, “Neural Network Based Controller Design for Three-PhasePWM AC/DC Voltage Source Converters,” in *2008 IEEE International Joint Conference on Neural Networks (IEEE World Congress on Computational Intelligence)*, 2008, pp. 3421–3427.

[28] M. Kabalan, P. Singh, and D. Niebur, “Large Signal Lyapunov-Based Stability Studies in Microgrids: A Review,” *IEEE Trans. Smart Grid*, no. 99, pp. 1–9, 2016.

[29] S. R. Sanders and G. C. Verghese, “Lyapunov-Based Control for Switched Power Converters,” *IEEE Trans. Power Electron.*, vol. 7, no. 1, pp. 17–24, 1992.

[30] C. Meza, D. Biel, D. Jeltsema, and J. M. A. Scherpen, “Lyapunov-Based Control Scheme for Single-Phase Grid-Connected PV Central Inverters,” *IEEE Trans. Control Syst. Technol.*, vol. 20, no. 2, pp. 520–529, 2012.

[31] R. Ortega, A. Loria, P. Nicklasson, and H. Sira-Ramirez, *Passivity-based control of Euler-Lagrange systems*. 1998.

[32] A. Loria and H. Nijmeijer, “PASSIVITY IN CONTROL SYSTEMS,” *Control Syst. Robot. Autom.*, vol. 13, pp. 1–24.

[33] Y. Gu, W. Li, and X. He, “Passivity-Based Control of DC Microgrid for Self-Disciplined Stabilization,” *IEEE Trans. Power Syst.*, vol. 30, no. 5, pp. 2623–2632, 2015.

[34] B. Maschke, L. U. M. R. Cnrs, and U. C. Bernard, “An introduction to Port Hamiltonian Systems,” 2005.

[35] D. Jeltsema and J. M. a. Scherpen, “Multidomain modeling of nonlinear networks and systems,” *Control Syst. IEEE*, vol. 29, no. August, pp. 28–59, 2009.

[36] D. Jeltsema, “Modeling and Control of Nonlinear Networks A Power-Based Perspective,” *Perspective*, no. August, p. 231, 2005.

[37] J. M. A. Scherpen, D. Jeltsema, and J. Ben Klaassens, “Lagrangian modeling of switching electrical networks,” *Syst. Control Lett.*, vol. 48, no. 5, pp. 365–374, 2003.

[38] J. C. Willems, “Terminals and Ports,” *Ieee Circuits Syst. Mag.*, 2010.

[39] A. Van Der Schaft, C. Science, and D. Jeltsema, *Port-Hamiltonian Systems Theory : An Introductory Overview*, vol. 1. 2014.

[40] R. Ortega, A. Van der Schaft, B. Maschke, and G. Escobar, “Interconnection and damping assignment passivity-based control of port-controlled Hamiltonian systems,” *Automatica*, vol. 38, no. 4, pp. 585–596, 2002.

[41] S. Nageshrao, G. Lopes, D. Jeltsema, and R. Babuska, “Port-Hamiltonian Systems in Adaptive and Learning Control: A Survey,” *IEEE Trans. Automat. Contr.*, vol. 9286, no. c, pp. 1–1, 2015.

[42] R. Ortega and E. García-Canseco, “Interconnection and Damping Assignment Passivity-Based Control: A Survey,” *Eur. J. Control*, vol. 10, no. 5, pp. 432–450, 2004.

[43] J. Zeng, Z. Zhang, and W. Qiao, “An Interconnection and Damping Assignment Passivity-Based Controller for a DC–DC Boost ConverterWith a Constant Power Load,” *IEEE Trans. Ind. Appl.*, vol. 50, no. 4, pp. 2314–2322, 2014.

[44] H. Sira-ram and R. A. P. Moreno, “Passivity Based Controllers for the Stabilization of DC to DC Power Converters,” pp. 1–30.

[45] D. Jeltsema, R. Ortega, and J. M. A. Scherpen, “An energy-balancing perspective of interconnection and damping assignment control of nonlinear systems,” *Automatica*, vol. 40, no. 9, pp. 1643–1646, 2004.

[46] A. Peart, “ONLINE LEARNING ALGORITHMS For Passivity-Based and Distributed Control,” Tu Delft, 2016.

[47] Z. Wang and P. Goldsmith, “Modified energy-balancing-based control for the tracking problem,” *IET Control Theory Appl.*, vol. 2, no. 4, pp. 310–322, 2008.

[48] A. Donaire and S. Junco, “On the addition of integral action to port-controlled Hamiltonian systems,” *Automatica*, vol. 45, no. 8, pp. 1910–1916, 2009.

[49] T. Kalitjuka, “Control of Voltage Source Converters for Power System Applications,” 2011.

[50] O. Anaya-Lara, C.-G. D., E. Moreno-Goytia, and G. Adam, “Voltage Source Converter Topologies,” in *Voltage Source Converter Topologies, in Offshore Wind Energy Generation: Control, Protection, and Integration to Electrical Systems*, 1st ed., vol. 18, no. 3, Chichester, UK.: John Wiley & Sons,Ltd, 2003, pp. 1034–1042.

[51] L. Shen, S. Bozhko, G. Asher, C. Patel, and P. Wheeler, “Active DC-Link Capacitor Harmonic Current Reduction in Two-Level Back-to-Back Converter,” *IEEE Trans. Power Electron.*, vol. 31, no. 10, pp. 6947–6954, 2016.

[52] I. Martínez-Pérez, G. Espinosa-Perez, G. Sandoval-Rodríguez, and A. Dòria-Cerezo, “IDA Passivity-Based Control of single phase back-to-back converters,” *IEEE Int. Symp. Ind. Electron.*, no. 2, pp. 74–79, 2008.

[53] M. Liserre, F. Blaabjerg, and S. Hansen, "Design and Control of an LCL-Filter-Based Three-Phase Active Rectifie," *IEEE Trans. Ind. Appl.*, vol. 41, no. 5, pp. 1281–1291, 2005.

[54] J. Rocabert, A. Luna, F. Blaabjerg, and P. Rodríguez, "Control of Power Converters in AC Microgrids," *IEEE Trans. Power Electron.*, vol. 27, no. 11, pp. 4734–4749, 2012.

[55] N. Mohan, U. Tore, and R. William, "Switch-mode DC-AC Inverters," in *Power Electronic CONVERTERS, APPLICATIONS, AND DESIGN*, Third., WILEY, 2003, pp. 200–248.

[56] M. S. Huertas, "the Use of Power Electronics for Emulating power distribution feeders," The University of Arkansas, 2008.

[57] M. Ciobotaru, R. Teodorescu, and F. Blaabjerg, "A new single-phase PLL structure based on second order generalized integrator," *PESC Rec. - IEEE Annu. Power Electron. Spec. Conf.*, no. July, 2006.

[58] P. Rodríguez, A. Luna, M. Ciobotaru, R. Teodorescu, and F. Blaabjerg, "Advanced grid synchronization system for power converters under unbalanced and distorted operating conditions," *IECON Proc. (Industrial Electron. Conf.*, no. 2, pp. 5173–5178, 2006.

[59] V. Kaura and V. Blasko, "Operation of a phase locked loop system under distorted utilityconditions," *IEEE Trans. Ind. Appl.*, vol. 33, no. 1, pp. 58–63, 1997.

[60] S. Chatterjee and S. Chatterjee, "Simulation of synchronous reference frame PLL based grid connected inverter for photovoltaic application," in *2015 1st Conference on Power, Dielectric and Energy Management at NERIST (ICPDEN)*, 2015, no. JANUARY 2015, pp. 1–6.

[61] S. Gao and B. Mike, "Phase-locked loop for AC systems: analyses and comparisons," in *6th IET International Conference on Power Electronics, Machines and Drives (PEMD 2012)*, 2012, no. 1, pp. 1–6.

[62] F. M. Serra, D. G. Forchetti, and C. H. De Angelo, "Comparison of positive sequence detectors for shunt active filter control," *2010 9th IEEE/IAS Int. Conf. Ind. Appl. INDUSCON 2010*, 2010.

[63] J. Cervera, A. J. Van Der Schaft, and A. Ba, "Interconnection of port-Hamiltonian systems and composition of Dirac structures," *Automatica*, no. August, 2006.

[64] A. Niragire, "Linear Quadratic Optimal Control for Cascaded Converters-Based Microgrid," University of Arkansas, 2017.

[65] M. Toulabi, S. Bahrami, and A. M. Ranjbar, "Application of Edge theorem for robust stability analysis of a power system with participating wind power plants in automatic generation control task," *IET Renew. Power Gener.*, vol. 11, no. 7, pp. 1049–1057, 2017.

[66] J. Zhou *et al.*, "Large-Scale Power System Robust Stability Analysis Based on Value Set Approach," *IEEE Trans. Power Syst.*, vol. 8950, no. i, pp. 1–1, 2017.

[67] F. Habibi, A. H. Naghshbandy, and H. Bevrani, "Robust voltage controller design for an isolated Microgrid using Kharitonov's theorem and D-stability concept," *Int. J. Electr. Power Energy Syst.*, vol. 44, no. 1, pp. 656–665, 2013.

[68] E. K. Kim, F. Mwasilu, H. H. Choi, and J. W. Jung, "An Observer-Based Optimal Voltage Control Scheme for Three-Phase UPS Systems," *IEEE Tran. Ind. Electron.*, vol. 62, no. 4, pp. 2073–2081, 2015.

[69] P. Cortés, G. Ortiz, J. I. Yuz, J. Rodríguez, S. Vazquez, and L. G. Franquelo, "Model Predictive Control of an Inverter With Output LC Filter for UPS Applications," *IEEE Trans. Ind. Electron.*, vol. 56, no. 6, pp. 1875–1883, 2009.

[70] D. E. Kim and D. C. Lee, "Feedback Linearization Control of Three-Phase UPS Inverter Systems," *IEEE Trans. Ind. Electron.*, vol. 57, no. 3, pp. 963–968, 2010.

[71] M. Nauman and A. Hasan, "Efficient Implicit Model-Predictive Control of a Three-Phase Inverter With an Output LC Filter," *IEEE Trans. Power Electron.*, vol. 31, no. 9, pp. 6075–6078, 2016.

[72] K. H. Reddy, S. Anupama, and S. Mahalakshmi, "Optimal Voltage Control Scheme on an Observer- Based For Three-Phase Ups Systems by Using Fuzzy," *Int. J. Electr. Eng.*, vol. 9, no. 2, pp. 139–154, 2016.

[73] F. M. Serra, C. H. De Angelo, and D. G. Forchetti, "IDA-PBC control of a DC–AC converter for sinusoidal three-phase voltage generation," *Int. J. Electron.*, vol. 7217, no. June, 2016.

[74] A. Timbus, M. Liserre, R. Teodorescu, P. Rodriguez, and F. Blaabjerg, "Evaluation of Current Controllers for Distributed Power Generation Systems," *Power Electron. IEEE Trans.*, vol. 24, no. 3, pp. 654–664, 2009.

[75] K. Mu, X. Ma, X. Mu, and D. Zhu, "Study on passivity-based control of voltage source PWM DC/AC inverter," in *Proceedings of 2011 International Conference on Electronic and Mechanical Engineering and Information Technology, EMEIT 2011*, 2011, vol. 8, pp. 3963–3967.

[76] L. Harnefors, A. G. Yepes, A. Vidal, and J. Doval-Gandoy, "Passivity-Based Stabilization of Voltage-Source Converters Equipped With LCL Input Filters," in *Proceedings, IECON 2014 - 40th Annual Conference of the IEEE Industrial Electronics Society*, 2014, pp. 1700–1706.

[77] S. Krul, "Modelling of Three-Phase Power Converters: A fundamental port-Hamiltonian approach."

[78] B. TerziÄ‡, G. MajiÄ‡, and A. Slutej, "Stability analysis of three-phase PWM converter with LCL filter by means of nonlinear model," *AUTOMATIKA*, vol. 51, no. 3, pp. 221–232, 2010.

[79] A. Reznik, M. G. Simoes, A. Al-Durra, and S. M. Muyeen, "LCL filter design and performance analysis for grid-interconnected systems," in *IEEE Industry Applications (IAS)*, 2014, vol. 50, no. 2, pp. 1225–1232.

[80] M. Liserre, A. Dell'Aquila, and F. Blaabjerg, "Stability Improvements of an LCL-filter Based Three-phase Active Rectifier Marco," *Power Electron. Spec. Conf. 2002. pesc 02. 2002 IEEE 33rd Annu.*, vol. 3, pp. 1195–1201, 2002.

[81] P. a. Dahono, "A Control Method to Damp Oscillation in the Input LC Filter of AC-DC Converters," in *2002 IEEE 33rd Annual IEEE Power Electronics Specialists Conference. Proceedings (Cat. No.02CH37289)*, 2002, vol. 4, pp. 1630–1635.

[82] J. Dannehl, C. Wessels, and F. W. Fuchs, "Limitations of voltage-oriented PI current control of grid-connected PWM rectifiers with LCL filters," *IEEE Trans. Ind. Electron.*, vol. 56, no. 2, pp. 380–388, 2009.

[83] G. Tan, H. Chen, and X. Zhang, "'Lagrangian modeling and passivity-based control of three-phase AC/DC voltage-source converters,'" *IEEE Trans. Ind. Electron.*, vol. 55, no. 4, pp. 1881–1882, 2008.

[84] A. Marzouki, M. Hamouda, and F. Fnaiech, "Nonlinear Control of Three-Phase Active Rectifiers Based L and LCL Filters," in *2013 International Conference on Electrical Engineering and Software Applications, ICEESA 2013*, 2013, no. 1, pp. 1–5.

[85] P. Wang, J. Wang, and Z. Xu, "Passivity-based control of three phase voltage source PWM rectifiers based on PCHD model," pp. 1126–1130.

[86] Y. Tang, H. Yu, and Z. Zou, "Hamiltonian modeling and energy-shaping control of three-phase ac/dc voltage-source converters," in *Proceedings of the IEEE International Conference on Automation and Logistics, ICAL 2008*, 2008.

[87] H. Yu, Z. Teng, J. Yu, and Y. Zang, "Energy-shaping and passivity-based control of three-phase PWM rectifiers," in *Proceedings of the 10th World Congress on Intelligent Control and Automation*, 2012, no. 61174131, pp. 2844–2848.

[88] F. Huerta, S. Styński, S. Cóbreces, M. Malinowski, and F. J. Rodríguez, "Novel control of three-phase active front-end converter with compensation of unknown grid-side inductance," *IEEE Trans. Ind. Electron.*, vol. 58, no. 8, pp. 3275–3286, 2011.

[89] S. M. M. Uddin, P. Akter, S. Mekhilef, M. Mubin, M. Rivera, and J. Rodriguez, "Model predictive control of an active front end rectifier with unity displacement factor," in *ICCAS 2013 - 2013 IEEE International Conference on Circuits and Systems: "Advanced Circuits and Systems for Sustainability,"* 2013, pp. 81–85.

[90] Y. Gu, H. Yu, J. Yu, and B. Shan, "Sliding-mode and PCH control of three phase PWM rectifier," in *Proceedings of the 2015 27th Chinese Control and Decision Conference, CCDC 2015*, 2015, no. 2, pp. 4480–4484.

[91] C. Gaviria, E. Fossas, and R. Griñó, "Robust controller for a full-bridge rectifier using the IDA approach and GSSA modeling," *IEEE Trans. Circuits Syst. I Regul. Pap.*, vol. 52, no. 3, pp. 609–616, 2005.

[92] C. Batlle, A. D` oria-Cerezo, and E. Fossas, "Bidirectional power flowcontrol of a power converter using passive Hamiltonian techniques," *Int. J. Circuit Theory Appl.*, vol. 36, no. 7, pp. 769–788, 2008.

APPENDIX A Matlab Script File for Stability Analysis of NCREPT System

```
Omega = 2*pi*60;

P24 = zeros(1,15); P23 = zeros(1,15); P22 = zeros(1,15); P21 = zeros(1,15);
P20 = zeros(1,15); P19 = zeros(1,15); P18 = zeros(1,15); P17 = zeros(1,15);
P16 = zeros(1,15); P15 = zeros(1,15); P14 = zeros(1,15); P13 = zeros(1,15);
P12 = zeros(1,15); P11 = zeros(1,15); P10 = zeros(1,15); P9 = zeros(1,15);
P8 = zeros(1,15);  P7 = zeros(1,15);  P6 = zeros(1,15);  P5 = zeros(1,15);
P4 = zeros(1,15);  P3 = zeros(1,15);  P2 = zeros(1,15);  P1 = zeros(1,15);

R_T = zeros(1,15); R_1 = zeros(1,15); R_2 = zeros(1,15);
R_R = zeros(1,15); R_3 = zeros(1,15); R_4 = zeros(1,15);

L_T = zeros(1,15); L_1 = zeros(1,15); L_2 = zeros(1,15);
L_L = zeros(1,15); L_3 = zeros(1,15); L_4 = zeros(1,15);

Grid_Imp=zeros(1,15);
Actual_Imp=zeros(1,15);

RL1 = zeros(1,15); RL2= zeros(1,15);

Incr = zeros(1,15);
Incr1 = zeros(1,15);
Incr2 = zeros(1,15);

 for k = 1:15
    Alpha = 0.3*(k-1);

  %Grid Input to NCREPT facility for Microgrid Configuration
   %The grid is a three-phase Y-connected source with a series resistance and inductance value,
   %most of which comes from the step-down transformer outside the building.
   %This transformer is a 12.47 kV – 480 V transformer rated to 1500 kVA.
   %It has a rated impedance of 5.9%, with a measured impedance angle of -80 degrees

  Pbase=1500e3;%Rated Power of Transformer
  Vbase=480;%Voltage on secondary side of Transformer
  Ibase= Pbase/Vbase/sqrt(3);%Rated Power of Transformer
  zbase =Vbase/Ibase/sqrt(3);%Base impedance of Transformer

  %%% Increase Grid Impedance and Calculate new Impedance values
  XmfrImp=5.9+(Alpha)%Xmfr percent impedance
  y=round(XmfrImp)%round to the nearest integer
  percentRS_vvvf= XmfrImp*0.174;%1.028 percent resistance
  RT=(percentRS_vvvf/100)*(zbase)%source resistance;1.58mohm
  percentLS_vvvf= sqrt((XmfrImp)^2-(percentRS_vvvf)^2)%5.81 percent reactance
```

```
  LT=(percentLS_vvvf/100)*(zbase)/(Omega)%23.67uH

  % Grid Impedance was increased
  ActualImp = sqrt(RT^2 + ((percentLS_vvvf/100)*(zbase))^2)

% System Parameters for VVVF drive and REGEN Bench
   L1 = 110e-6;%VVVF input filter inductance
   L2 = 110e-6; %VVVF Output filter inductance
   L  = 23.67e-6;%6.1e-6 Xmf reactance grid inductance
   L3 = 20e-6; %REGEN input filter inductance
   L4 = 20e-6;%REGEN output filter inductance

   R1 = L1*Omega/10; %VVVF input filter resistance
   R2 = L2*Omega/10;%VVVF output filter resistance
   R  = 1.58e-3; %L*Omega/7 %Xmf impedance grid resistance
   R3 = L3*Omega/10; %REGEN input filter resistance
   R4 = L4*Omega/10; %REGEN output filter resistance

   C1 = 1152e-6; %VVVF input filter Capacitance (3x384uF)
   C2 = 28800e-6; %VVVF output filter Capacitance (3x960uF)
   C3 = 1440e-6; %REGEN input filter Capacitance (3x480uF)
   C4 = 1440e-6;%REGEN output filter Capacitance (3x480uF)

   Cdc1 = 42.3e-3; %DC link capacitors for VVVF
   Cdc2 = 32.4e-3; %DC link capacitors for REGEN
   R_L1 = .23e0; %- 2.3*(Alpha + .01);
   R_L2 = .23e0; %- 2.3*(Alpha +.01); %Loads
%% A, B & F matrices:

   A11 = [ -RT/LT Omega 0 0 0 0 0 0 0 0 0 0;
      -Omega -RT/LT 0 0 0 0 0 0 0 0 0 0;
      0 0 -R1/L1 Omega 0 0 0 0 0 0 0 0;
      0 0 -Omega -R1/L1 0 0 0 0 0 0 0 0;
      0 0 0 0 -R2/L2 Omega 0 0 0 0 0 0;
      0 0 0 0 -Omega -R2/L2 0 0 0 0 0 0;
      0 0 0 0 0 0 -R/L Omega  0 0 0 0;
      0 0 0 0 0 0 -Omega -R/L  0 0 0 0;
      0 0 0 0 0 0 0 0 -R/L Omega 0 0;
      0 0 0 0 0 0 0 0 -Omega -R/L 0 0;
      0 0 0 0 0 0 0 0 0 0 -R3/L3 Omega;
      0 0 0 0 0 0 0 0 0 0 -Omega -R3/L3];
```

```
A12 = [ 0 0 0 0 -1/LT 0 0 0 0 0 0 0;
   0 0 0 0 0 -1/LT 0 0 0 0 0 0;
   0 0 -U1d/L1 0 1/L1 0 0 0 0 0 0 0;
   0 0 -U1q/L1 0 0 1/L1 0 0 0 0 0 0;
   0 0 U2d/L2 0 0 0 -1/L2 0 0 0 0 0;
   0 0 U2q/L2 0 0 0 0 -1/L2 0 0 0 0;
   0 0 0 0 0 0 2/(3*L) 0 -1/(3*L) 0 -1/(3*L) 0;
   0 0 0 0 0 0 0 2/(3*L) 0 -1/(3*L) 0 -1/(3*L);
   0 0 0 0 0 0 1/(3*L) 0 -2/(3*L) 0 1/(3*L) 0;
   0 0 0 0 0 0 0 1/(3*L) 0 -2/(3*L) 0 1/(3*L);
   0 0 0 -U3d/L3 0 0 0 0 1/L3 0 0 0;
   0 0 0 -U3q/L3 0 0 0 0 0 1/L3 0 0];

A21 = [ 0 0 0 0 0 0 0 0 0 0 0 0;
   0 0 0 0 0 0 0 0 0 0 0 0;
   0 0 U1d/Cdc1 U1q/Cdc1 -U2d/Cdc1 -U2q/Cdc1 0 0 0 0 0 0;
   0 0 0 0 0 0 0 0 0 0 U3d/Cdc2 U3q/Cdc2;
   1/C1 0 -1/C1 0 0 0 0 0 0 0 0 0;
   0 1/C1 0 -1/C1 0 0 0 0 0 0 0 0;
   0 0 0 0 1/C2 0 -1/C2 0 0 0 0 0;
   0 0 0 0 0 1/C2 0 -1/C2 0 0 0 0;
   0 0 0 0 0 0 0 0 1/C3 0 -1/C3 0;
   0 0 0 0 0 0 0 0 0 1/C3 0 -1/C3;
   0 0 0 0 0 0 1/C4 0 -1/C4 0 0 0;
   0 0 0 0 0 0 0 1/C4 0 -1/C4 0 0];

A22 = [ -R4/L4 Omega 0 -U4d/L4 0 0 0 0 0 0 1/L4 0;
   -Omega -R4/L4 0 -U4q/L4 0 0 0 0 0 0 0 1/L4;
   0 0 0 0 0 0 0 0 0 0 0 0;
   U4d/Cdc2 U4q/Cdc2 0 0 0 0 0 0 0 0 0 0;
   0 0 0 0 0 Omega 0 0 0 0 0 0;
   0 0 0 0 -Omega 0 0 0 0 0 0 0;
   0 0 0 0 0 0 0 Omega 0 0 0 0;
   0 0 0 0 0 0 -Omega 0 0 0 0 0;
   0 0 0 0 0 0 0 0 -1/(R_L1*C3) Omega 0 0;
   0 0 0 0 0 0 0 0 -Omega -1/(R_L1*C3) 0 0;
   -1/C4 0 0 0 0 0 0 0 0 0 -1/(R_L2*C4) Omega;
   0 -1/C4 0 0 0 0 0 0 0 0 -Omega -1/(R_L2*C4)];

A = vertcat(horzcat(A11,A12),horzcat(A21,A22));

Poles = eig(A); Determine the eigenvalues of the system
```

```
    B11 = [ 0 0 0 0 0 0 0 0;
       0 0 0 0 0 0 0 0;
       -Vdc1/L1 0 0 0 0 0 0 0;
       0 -Vdc1/L1 0 0 0 0 0 0;
       0 0 Vdc1/L2 0 0 0 0 0;
       0 0 0 Vdc1/L2 0 0 0 0;
       0 0 0 0 0 0 0 0;
       0 0 0 0 0 0 0 0;
       0 0 0 0 0 0 0 0;
       0 0 0 0 0 0 0 0;
       0 0 0 0 -Vdc2/L3 0 0 0;
       0 0 0 0 0 -Vdc2/L3 0 0];

    B21 = [ 0 0 0 0 0 0 -Vdc2/L4 0;
       0 0 0 0 0 0 0 -Vdc2/L4;
       I2d/Cdc1 I2q/Cdc1 -I3d/Cdc1 -I3q/Cdc1 0 0 0 0;
       0 0 0 0 I6d/Cdc2 I6q/Cdc2 I7d/Cdc2 I7q/Cdc2;
       0 0 0 0 0 0 0 0;0 0 0 0 0 0 0 0;0 0 0 0 0 0 0 0;
       0 0 0 0 0 0 0 0;0 0 0 0 0 0 0 0;0 0 0 0 0 0 0 0;
       0 0 0 0 0 0 0 0;0 0 0 0 0 0 0 0];

    B = vertcat(B11,B21); C = eye(24); D = 0*B;

    F = [1/LT 0 0 0 0 0 0 0 0 0 0 0 0 0 0 0 0 0 0 0 0 0 0 0;
       0 1/LT 0 0 0 0 0 0 0 0 0 0 0 0 0 0 0 0 0 0 0 0 0 0 0;
       0 0 0 0 0 0 0 0 0 0 0 0 0 0 0 0 0 0 0 0 0 0 1/C4 0;
       0 0 0 0 0 0 0 0 0 0 0 0 0 0 0 0 0 0 0 0 0 0 0 1/C4]';

    C = [0 0 0 0 0 0 0 0 0 0 0 0 0 0 0 0 0 0 0 0 0 0 1 0;
    0 0 0 0 0 0 0 0 0 0 0 0 0 0 0 0 0 0 0 0 0 0 0 1];

    P24(k)= Poles(24);P23(k) = Poles(23);P22(k) = Poles(22);P21(k) = Poles(21);
    P20(k)= Poles(20);P19(k) = Poles(19);P18(k) = Poles(18);P17(k) = Poles(17);
    P16(k)= Poles(16);P15(k) = Poles(15);P14(k) = Poles(14);P13(k) = Poles(13);
    P12(k)= Poles(12);P11(k) = Poles(11);P10(k) = Poles(10);P9(k) = Poles(9);
    P8(k) = Poles(8);P7(k) = Poles(7);P6(k) = Poles(6);P5(k) = Poles(5);
    P4(k) = Poles(4);P3(k) = Poles(k);P2(k) = Poles(2);P1(k) = Poles(1)

t = 0:14;
figure(1);
set(gca,'fontsize',16);
plot((P1),'x');
hold on
plot((P2),'x');
hold on
```

```
plot((P4),'x');
hold on
plot((P15),'x');
hold on
plot((P16),'x');
hold on
plot((P17),'x');
hold on
plot((P18),'x');
grid on
title('Pole eigenvalues');
xlabel('Real axis');
ylabel('Imaginary axis');

    %%%% Controllability Analysis
    Cdc=zeros(2,24);%output matrix
    Ddc=zeros(2,8);
    Cdc(1,15)=1;
    Cdc(2,16)=1;
    Gss=ss(A,B,Cdc,Ddc);

    % System transfer function
    Gdc=ss(A,B,Cdc,Ddc);% system
     Gtfcom=tf(Gdc);%
    %Isolate tranfer functions
     Gtfcom_Vdc1 = Gtfcom(1,1); %transfer function of VVVF
     Gtfcom_Vdc2 = Gtfcom(2,6); %transfer fucntion of REGEN

      % PI Controller
      Gcom=ss(A,B,Cout,zeros(10,8));
      Gtfcom=tf(Gcom);

% PI Feedback Controller Implementation:
  % a PI Control is applied in a negative feedback with the VVVVF system
    [C_PI1,Info1] = pidtune(Gtfcom_Vdc1,'PI');
   T1 = feedback(C_PI1*Gtfcom_Vdc1,1);

 % a PI Control is applied in a negative feedback with the REGEN system
    [C_PI2,Info2] = pidtune(Gtfcom_Vdc2,'PI');
    T2 = feedback(C_PI2*Gtfcom_Vdc2,1);

     [C_PI3,Info3] = pidtune(Gtfcom_V3d,'PI');
     T3 = feedback(C_PI3*Gtfcom_V3d,1);

     [C_PI4,Info4] = pidtune(Gtfcom_V3q ,'PI');
     T4 = feedback(C_PI4*Gtfcom_V3q ,1);
```

```
[C_PI5,Info5] = pidtune(Gtfcom_V4d,'PI');
T5 = feedback(C_PI5*Gtfcom_V4d,1);

[C_PI6,Info6] = pidtune(Gtfcom_V4q,'PI');
T6 = feedback(C_PI6*Gtfcom_V4q,1);

% Find the polynomial coefficient of the system matrix A

% Plot root space for the family of polynomial for the system matrix using the maximum and
minimum values defined by the interval desired interval polynomial coefficients to determine if
the system is robustly stable

%%%%%%%%%%%%%%%%%%Edge Theorem %%%%%%%%%%%%%%%%%%

% edge polynomials of VVVF dc link to grid impedance transfer function with
% parametric variation of transformer resistance and inductance impedance

P1=[1  1.281e04 2.774e08  2.34e12   2.69e16  1.587e20 1.233e24  5.165e27 2.984e31 8.831e34
4.025e38 8.268e41 3.048e45  4.188e48 1.231e52 1.052e55 2.243e58 1.038e61 9.95e63 2.947e66
1.594e69 2.873e71 8.602e73 7.105e75 3.489e77  7.021e78];


P2=[1  1.273e04 2.756e08  2.307e12  2.651e16 1.548e20 1.202e24  4.964e27 2.869e31 8.307e34
3.804e38 7.563e41 2.825e45 3.692e48 1.116e52 8.79e54 1.98e58 7.882e60 8.318e63 2.123e66
1.285e69 2.051e71 6.895e73 5.564e75 2.713e77 5.419e78];

P3=[1 1.275e04 2.766e08   2.322e12  2.676e16 1.57e20  1.223e24   5.09e27 2.954e31 8.652e34
3.974e38 8.029e41 3.002e45 4.01e48 1.209e52 9.814e54 2.189e58 9.153e60 9.475e63 2.541e66
1.5e69 2.485e71 8.138e73 6.451e75 2.977e77 5.692e78];

P4=[1 1.273e04 2.756e08   2.307e12  2.651e16 1.548e20 1.202e24  4.963e27  2.869e31
8.306e34 3.804e38 7.561e41 2.825e45 3.691e48 1.116e52 8.787e54 1.98e58 7.877e60 8.316e63
2.121e66 1.285e69 2.05e71 6.894e73 5.564e75 2.713e77 5.419e78];


% %  Vertex polynomials for VVVF and REGEN System

Characteristic polynomial of VVVF rectifier
P1=[1  1.281e04 2.774e08  2.34e12   2.69e16  1.587e20 1.233e24  5.165e27 2.984e31 8.831e34
4.025e38 8.268e41 3.048e45  4.188e48 1.231e52 1.052e55 2.243e58 1.038e61 9.95e63 2.947e66
1.594e69 2.873e71 8.602e73 7.105e75 3.489e77  7.021e78];
```

Characteristic polynomial of REGEN rectifier

```
 P2 =[1 1.285e04 5.977e08 5.645e12  1.311e17  9.003e20 1.336e25  6.416e28 6.522e32
2.052e36 1.44e40 2.845e43 1.412e47 1.636e50 5.745e53  3.982e56  8.708e59 3.858e62
3.926e65 1.175e68  6.662e70  1.294e73 4.024e75 4.292e77  3.715e79  1.017e81 ];
```

Characteristic polynomial of REGEN Inverter

```
  P3 =[1 1.111e04 5.841e08 5.054e12 1.367e17 9.245e20 1.674e25 8.773e28  1.17e33 4.625e36
4.711e40 1.339e44 1.042e48  1.961e51 1.123e55 1.226e58 4.769e61 2.171e64 3.778e67
1.124e70 9.032e72 1.791e75 6.818e77 7.874e79 5.121e81  5.313e82];
```

Characteristic polynomial of inverter VVVF

```
 P4= [1 1.283e04 5.971e08 5.628e12 1.308e17 8.964e20 1.33e25  6.377e28 6.482e32 2.034e36
1.426e40 2.81e43 1.392e47 1.586e50  5.631e53  3.722e56  8.417e59  3.416e62  3.631e65
9.639e67 5.826e70 9.234e72 3.172e75 2.073e77 1.417e79 3.089e80];


  nn=0;
for uu=0:0.01:1
   nn=nn+1;
La=uu;
P1P2=(1-La)*P1+La*P2;
P1P3=(1-La)*P1+La*P3;
P1P4=(1-La)*P1+La*P4;
P2P1=(1-La)*P2+La*P1;
P2P3=(1-La)*P2+La*P3;
P2P4=(1-La)*P2+La*P4;
P3P1=(1-La)*P3+La*P1;
P3P2=(1-La)*P3+La*P2;
P3P4=(1-La)*P3+La*P4;
P4P1=(1-La)*P4+La*P1;
P4P2=(1-La)*P4+La*P2;
P4P3=(1-La)*P4+La*P3;

KK(:,nn)=[roots(P1P2);roots(P1P3);roots(P1P4);roots(P2P1);roots(P2P3);roots(P2P4);roots(P3P
1);roots(P3P2);roots(P3P4);roots(P4P1);roots(P4P2);roots(P4P3)];
end
plot(KK,'*')
xlabel('Real axis');
ylabel('Imaginary axis');
title('Root Space of Edge Polynomials');
```

APPENDIX B NCREPT System Parameters

Introduction

This appendix discusses the nominal values of the LC filter of the Variable Voltage Variable Frequency drive (VVVF) and Regenerative load (REGEN) bench of the microgrid configuration. Additionally, the system's transformer values are also presented in Table B.1. The values obtained were used in designing the passivity-based controller for the NCREPT system and performing simulations of the system.

Regenerative Load Benches

Each regenerative bench has a cabinet where the LC filter is located. When the filter cabinet of one of the REGEN was opened, a total of sixteen filter capacitors were found, as shown in Figure B.1. The model of each of those capacitors is ELECTRONICON MKPg 275.186-809600/221702 with value of Δ3x96 μF.From those sixteen capacitors, five capacitors were connected to the fuses of the inverter side of the REGEN, five capacitors were connected to fuses of the rectifier side of the REGEN and six capacitors were disconnected, as seen in Figure B.2. Thus, the filter capacitor of the rectifier side and inverter side each has a total value of Δ3x480 μF. In the same cabinet, the filter inductors were found and were rated at 2.5 kA with value of 20 μH, as illustrated in Figure B.3. Thus, both the rectifier side and inverter side of the regen each have a total filter inductor value of 20 μH.

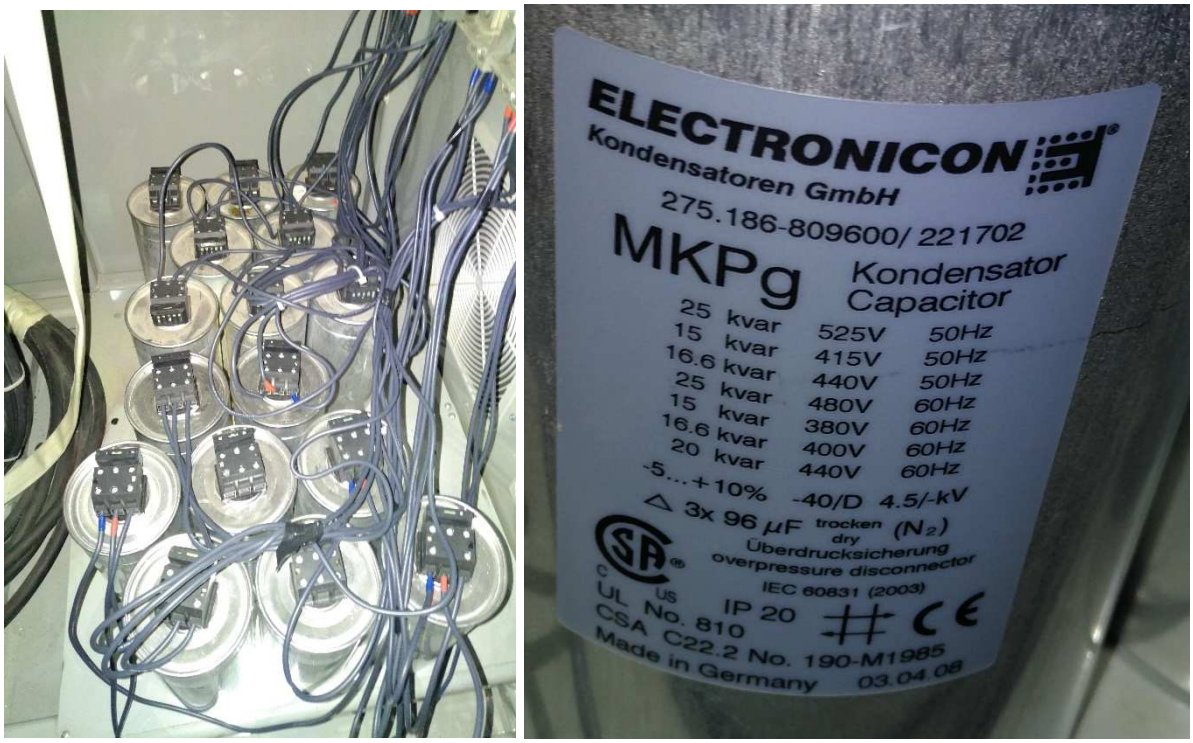

Figure B.1 Filter Capacitors in Regen bench (left) and model of filter Capacitors (right).

.

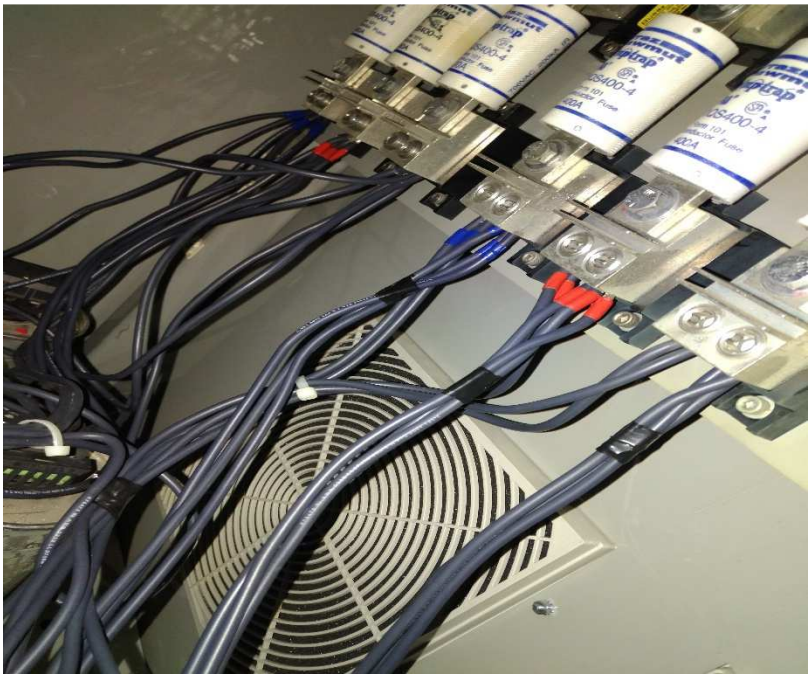

Figure B.2 Fuse Connection of Filter Capacitor for Rectifier and Inverter of Regen.

Figure B.3 Filter Inductors in REGEN bench (left) and model of Filter Inductors (right).

Variable Voltage Variable Frequency Drive

The VVVF also has a cabinet where the LC filters are located. When the filter cabinet of the VVVF was opened, a total of twenty filter capacitors were found, as shown in Fig. B.4. The model of each of those capacitors were the same as the ones in the REGEN bench with value of Δ3x96 μF. From those twenty capacitors, ten capacitors were connected to the fuses of the inverter side of the VVVF, four capacitors were connected to the fuses of the rectifier side of the VVVF drive and six capacitors were disconnected, as seen in Figure B.5. Thus, the filter capacitor of the rectifier side has a total value Δ3x384 μF and the filter capacitor of the inverter side has total value of Δ3x960 μF. Also, in the same cabinet, the filter inductors were found, each rated at 0.75 kA with value of 110 μH, as illustrated in Figure B.6. Thus, both the rectifier side and inverter side of the VVVF each have total value of 110 μH.

Figure B.7 illustrates the DC link capacitors utilized in the NCREPT system which were 2500μF rated at 900Vdc. Sixteen capacitors were used in the VVVF drive and twelve were used

in the REGEN bench system for values of 42.4mF and 32.4 mF respectively. EMI capacitors were also obtained from the VVVF drive and REGEN bench which were 40µF and 20µF respectively.

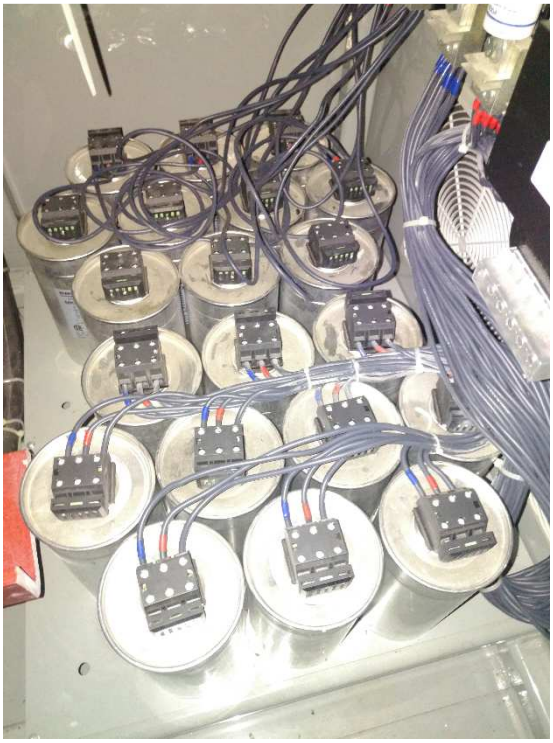

Figure B.4 Filter Capacitors in VVVF drive.

Figure B.5 Fuse Connection of Filter Capacitor for Rectifier and Inverter of VVVF.

Figure B.6 Filter inductors in VVVF (left) and model of the filter Inductors (right).

Figure B.7 DC Link Capacitors VVVF drive and REGEN Bench.

Table B.1 Transformer Ratings

Transformer Name	Voltage (kV)	Rated Power (kVA)	Impedance (~ %)
T1	0.48Δ/4.16/13.8Y	2500	5.9
T2	0.48Δ/4.16/13.8Y	2500	5.9
T3	0.48Δ/4.16/13.8Y	2500	5.9
T4	0.48Δ/4.16/13.8Y	2500	5.9
T5	0.48Δ/4.16/13.8Y	2500	5.9
T6	0.48Δ/4.16/13.8Y	2500	5.9
Utility Txmr	12.47Y/0.480Y	750	5.9

APPENDIX C Matlab Script File for Microgrid Simulation

```
%NCREPT  MICROGRID Project Simulation Parameters
%                    REGEN BENCH DATA
%%***********************************************
% Current and voltage ratings
Prated=2e6;% Continuous MVA Rating Input/Output
Irated=2405; %Continous Input/Output Current (Amps)
Vrated=480;  %VAC input/output
Frated=60;    % Operating frequency (Hz)
C_par = 360e-9; % parasitic capacitance

% Filter Inductor
Li=20e-6;%Henry @ 2500A

% DC Bus Capacitance
Cdc=32.4e-3; %Farad @900V

%% Specify control parameters  for REGEN BENCH
% REGEN PWM Switching Frequency
Fpwm = 8e3;% switching frequency was 8K
Fcontrol = 4e3;
Fcontrol_bus = 8e3;
Fcontrol_current =8e3;

% GAINS NUMBERS ENTERED FROM KEYPAD
BUS_PROP_GAIN=3;
BUS_INT_GAIN=2;
CURRENT_PROP_GAIN=10;
CURRENT_INT_GAIN=150;

% REGEN BENCH LOAD SIMULATOR GAINS
RGB_LS_CURRENT_PROP_GAIN=75;
RGB_LS_CURRENT_INT_GAIN=150*10;

% Current limit in per unit
%peak current for REGEN2 unit is 4800A. Ilimit=4800/2500=1.922;
Ilimit=2;
%Maximum and minimum value for dc bus voltages of REGEN
VdcRef = 1.5625*Vrated; % dcbus voltage is 750V
VdcMin = 0.904*VdcRef;% pre-charge dc bus voltage 678V
VdcMax = 1.1*VdcRef; % would be 825V when overload capacity is 110% at 60 secs
```

```
%%%%% Specify Simulation conditions

%% Compute/derive component/control values
 wrated=2*pi*Frated; %angular frequency
 zbase=Vrated/Irated/sqrt(3); % base impedance
 puLi=wrated*Li/zbase;%per unit inductance
 Ls=   percentLs/100*zbase/wrated;  % source inductance
 Rs=   percentRs/100*zbase;  % source resistance
 pwm = 1/Fpwm;%period
 Tcontrol=1/Fcontrol;

%The maximum ac current allowed in the regen drive converters;4800A
MaxPeakCurrent = 2*Irated;%maximum current

%Current loop PI design for REGEN dc bus
Kcloop=zbase/Li;
Kp_c=CURRENT_PROP_GAIN/Kcloop*160.4
Ki_c=CURRENT_INT_GAIN*Kp_c/20/8000

% Regen Bench Load Simulator Current Controller Design
RGB_LS_Kp_c=RGB_LS_CURRENT_PROP_GAIN/Kcloop*160.4;
RGB_LS_Ki_c=RGB_LS_CURRENT_INT_GAIN*Kp_c/20/8000;

% Timing for breaker coordination in simulation
vvvfDCStart = 0.1;% time in seconds when main contactor is closed and power is applied to
the 3VF; precharge of dc bus
vvvfACStart = 0.18  time in seconds at which the output inverter for the 3VF is turned on and
provide power to down stream circuitry
regenDCStart = 0.30; % time in seconds at which the control for input rectifier for the regen
drive is turned on;  pre-charge  of the dc bus capacitor.
regenLoadStart = 0.25;% time in seconds at which output inverter for the regen drive is turned
on to provide power to the load
%REGEN Load simulator
rgbLSClose = regenLoadStart - 0.1; %Time when the load switch closes


% Regen Bench Load Current
rgbLSPF = 1.0;% powerfactor of the load of the regen bench
rgbLSCurrent= -1.0;%magnitude of the commanded load current of the regen bench
rgbLSIdRef = rgbLSCurrent * rgbLSPF;%d axis  value of the commanded load current of
regen
if rgbLSPF > 0
   rgbLSIqRef = rgbLSCurrent * sqrt(1-rgbLSPF^2);%q axis  value of the commanded load
current of regen
else
   rgbLSIqRef = -rgbLSCurrent * sqrt(1-rgbLSPF^2);
end
```

```
rgbIRef = [0    0                rgbLSCurrent          rgbLSCurrent];
rgbITime= [0    regenLoadStart     regenLoadStart+0.01     regenLoadStart+10];

%%*************************************************************************
%%                          VVVF DATA
%%****************************************
% Current and voltage and Power ratings
Prated_vvvf=750e3;
Vrated_vvvf=480;
Frated_vvvf=60;
wn = wbw/beta;
m=Vrated*sqrt(2)/VdcRef;
Kbusloop=m/Cdc/zbase;
Kp_bus=BUS_PROP_GAIN/10*1332.5/Kbusloop;%       ;
Ki_bus=BUS_INT_GAIN/25*8.8e5/Kbusloop/4000;
Irated_vvvf=Prated_vvvf/480/sqrt(3);

% Converter Filter inductance
Li_vvvf = 110e-06;
%EMI filter capacitance
Cemi_vvvf=40e-6;
% phase-phase capacitance
Ci_vvvf = 384e-6; % delta connected input filter capacitance for AFE rectIFIER
Co_vvvf = 960e-6;% %delta connected Output filter capacitance for Inverter
% DC Bus Capacitance
Cdc_vvvf=42.3e-3;% Farad @900V
Cdc_init_V = 750;% dc bus  referenc voltage

%% Specify control parameters
% PWM Switching Frequency
Fpwm_vvvf = 8e3;
Fcontrol_vvvf = 8e3;

% Current limit in per unit
Ilimit_vvvf=1.50;
 VdcRef_vvvf = 1.5625*Vrated_vvvf;  750V
%VdcRef_vvvf = 750;
VdcMin_vvvf = 0.9*VdcRef_vvvf;
VdcMax_vvvf = 1.1*VdcRef_vvvf; % would be 825 for 480Vac
VacRef_vvvf = 480/Vrated_vvvf; %AC reference voltage for Grid forming mode
% VAC Reference
VrefTime_vvvf=  [0        vvvfACStart   vvvfACStart+0.1          vvvfACStart+10];
VrefValue_vvvf= [0         VacRef_vvvf         VacRef_vvvf         VacRef_vvvf];

%% Specify Simulation conditions
% Percent Source reactance
```

```
percentLs_vvvf=6;% This number should be 5 for a 5% impedance, not 0.05.
percentRs_vvvf=0.6;
 % Output frequency
FreqRef_vvvf = 60;
%% Compute/derive component/control values
wrated_vvvf=2*pi*Frated_vvvf;
zbase_vvvf=Vrated_vvvf/Irated_vvvf/sqrt(3); % base impedance
puLi_vvvf=wrated_vvvf*Li_vvvf/zbase_vvvf;
Ls_vvvf=   percentLs_vvvf/100*zbase_vvvf/wrated_vvvf;  % source inductance
Rs_vvvf=   percentRs_vvvf/100*zbase_vvvf; % source resistance
Tpwm_vvvf = 1/Fpwm_vvvf;
Tcontrol_vvvf=1/Fcontrol_vvvf;
MaxPeakCurrent_vvvf = Ilimit_vvvf*Irated_vvvf;
```